Title

Thin-Film Ferroelectrics

Journal

Advanced Materials, 34(30)

ISSN

0935-9648

Authors

Fernandez, Abel

Acharya, Megha

Lee, Han-Gyeol

et al.

Publication Date

2022-07-01

DOI

10.1002/adma.202108841

Peer reviewed

ADVANCED MATERIALS
www.advmat.de

Thin-Film Ferroelectrics

*Abel Fernandez, Megha Acharya, Han-Gyeol Lee, Jesse Schimpf, Yizhe Jiang, Djamila Lou, Zishen Tian, and Lane W. Martin**

Over the last 30 years, the study of ferroelectric oxides has been revolutionized by the implementation of epitaxial-thin-film-based studies, which have driven many advances in the understanding of ferroelectric physics and the realization of novel polar structures and functionalities. New questions have motivated the development of advanced synthesis, characterization, and simulations of epitaxial thin films and, in turn, have provided new insights and applications across the micro-, meso-, and macroscopic length scales. This review traces the evolution of ferroelectric thin-film research through the early days developing understanding of the roles of size and strain on ferroelectrics to the present day, where such understanding is used to create complex hierarchical domain structures, novel polar topologies, and controlled chemical and defect profiles. The extension of epitaxial techniques, coupled with advances in high-throughput simulations, now stands to accelerate the discovery and study of new ferroelectric materials. Coming hand-in-hand with these new materials is new understanding and control of ferroelectric functionalities. Today, researchers are actively working to apply these lessons in a number of applications, including novel memory and logic architectures, as well as a host of energy conversion devices.

1. Introduction

The last three decades of ferroelectric research have seen unprecedented advancements in the control, understanding, and utilization of this intriguing order parameter. Evolving from early work on the synthesis of bulk ceramic powders, researchers have developed the capability to create single-crystalline specimens of any number of compositions, with control approaching the atomic level and, in turn, we are being rewarded with previously unimagined polar textures and properties. Ferroelectrics belong to a special crystal class of polar, non-centrosymmetric structures which can possess a spontaneous electric polarization which can be controlled using applied electric fields (**Figure 1**). Ferroelectrics themselves are inherently hierarchical materials—wherein picometer ionic displacements give rise to polarization which can collectively extend over millimeters or self-organize into complex mesoscopic structures or collectively reorient under applied stimuli (e.g., electric fields, temperature, or stress). Understanding these complex behaviors necessitates a multilevel approach, wherein atomistic, microscopic, mesoscopic, and macroscopic properties are studied in concert. Parallel advances in synthesis, characterization, and simulation have enabled such multimodal studies and provided a methodology through which a multitude of ferroelectric functionalities can now be achieved and studied.

The promise of utilizing these functionalities in a number of applications kick-started the modern era of ferroelectric research in the mid-20th century.[1] Looking further back, in the 1920s, the ability to switch the polarization of sodium potassium tartrate tetrahydrate (commonly known as Rochelle salt) was first observed, along with dielectric and piezoelectric anomalies near the ferroelectric transition—now called the Curie point. In the 1940s, as part of the accelerated research push associated with World War II, ferroelectric $BaTiO_3$ was discovered by accident. When modifying TiO_2 with BaO to enhance its dielectric properties, a record-high dielectric permittivity was discovered and subsequent studies demonstrated a hysteretic switchable polarization. This discovery ushered in a new understanding of ferroelectricity as more than a rare phenomenon associated with salts that contained hydrogen bonding, but rather as a phenomenon that could exist in simple oxides like perovskites. Over the subsequent decades, the number of ferroelectric compositions exploded, particularly within the perovskite oxides, introducing new chemistries including $LiNbO_3$ and the $PbZr_xTi_{1-x}O_3$ system. Meanwhile, theoretical descriptions of ferroelectricity were advanced through lattice-dynamical models invoking a soft-mode optical phonon. Studies of the piezoelectric, thermodynamic, and optical properties in ferroelectric ceramics allowed for their deployment in a number of applications including piezoelectric sensors and pyroelectric infrared detectors. By the 1960s, increased interest in using ferroelectric polarization for nonvolatile memory was driving research into

A. Fernandez, M. Acharya, H.-G. Lee, J. Schimpf, Y. Jiang, D. Lou, Z. Tian, L. W. Martin
Department of Materials Science and Engineering
University of California, Berkeley
Berkeley, CA 94720, USA
E-mail: lwmartin@berkeley.edu
A. Fernandez, M. Acharya, H.-G. Lee, J. Schimpf, Y. Jiang, D. Lou, Z. Tian, L. W. Martin
Materials Sciences Division
Lawrence Berkeley National Laboratory
Berkeley, CA 94720, USA
The ORCID identification number(s) for the author(s) of this article can be found under https://doi.org/10.1002/adma.202108841.

DOI: 10.1002/adma.202108841

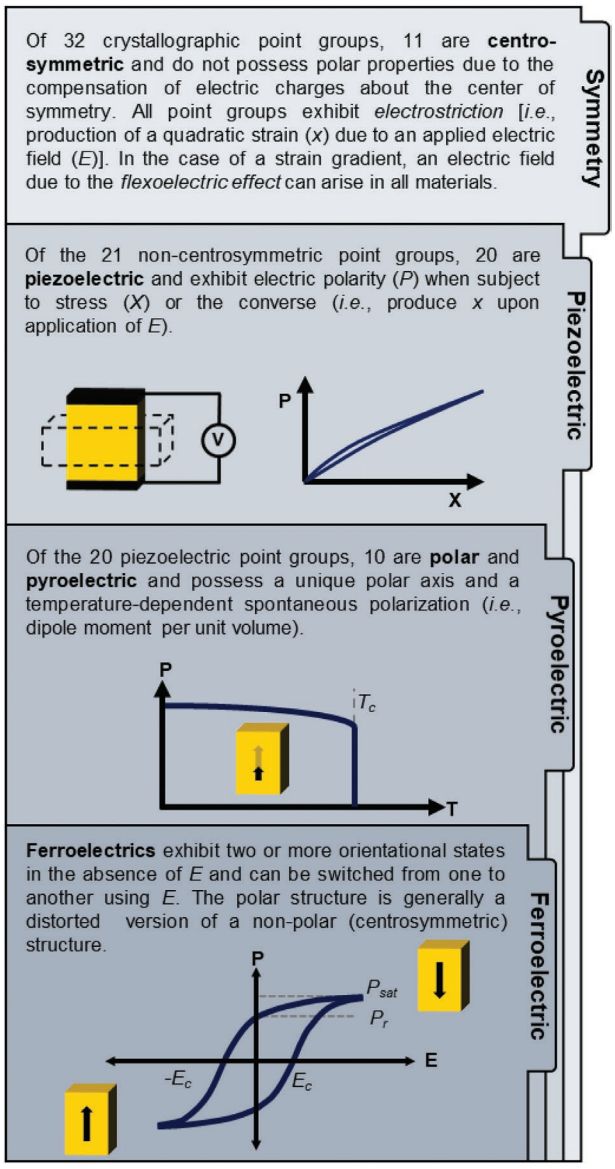

Figure 1. Symmetry-based hierarchy of material properties.

the synthesis of ferroelectrics as thin films for integration into microelectronics.

In parallel with this push for the integration of ferroelectrics at the sub-micrometer scale were rapid advancements in the development of thin-film-deposition techniques and the role of epitaxy, generally (at least initially) in the rapidly expanding semiconductor industry. Techniques like molecular-beam epitaxy and, in particular, pulsed-laser deposition, had only just begun to allow for the successful synthesis of thin films of oxide superconductors (e.g., $YBa_2Cu_3O_7$) and other correlated-electron oxides, such as those exhibiting colossal magnetoresistance (CMR). The ability to epitaxially deposit a thin, single-crystalline form of these oxide materials opened a new paradigm of synthetic control and experimental opportunities that had previously only been afforded to semiconductors. Naturally, these deposition techniques were eventually employed to synthesize ferroelectric thin films. It was soon understood that the direct coupling of the primary order parameter, namely the polarization, to the lattice resulted in an unprecedented degree of control over ferroelectric properties. Whereas epitaxial manipulation could influence carrier densities or transition temperatures in CMR and high-transition-temperature superconductors by tens of degrees, it was found that ferroelectric properties were far more susceptible to the electrical and elastic boundary conditions imposed through epitaxy.

From this serendipitous intersection of the need to address challenges in micro- and nanoscale devices, and the development of unprecedented structural and chemical control afforded by epitaxial deposition has emerged a rapidly expanding field of research wherein epitaxy is leveraged to study the fundamental physics of ferroelectrics and unlock previously inconceivable functionalities. Here, we look back on the development of ferroelectric thin-film research and review some important results in ferroelectric physics and functionality enabled by epitaxy. For some time now, the community has made use of the ability to precisely control electrode–ferroelectric interfaces and scale ferroelectrics down to nanometer length scales to probe questions directly related to the integration of ferroelectrics in new logic and memory devices. The employment of epitaxial strain via the lattice mismatch between the ferroelectric and substrate materials now also offers a way to directly manipulate the polarization, resulting in enhanced polar order and a myriad of new hierarchical domain structures. These results have laid the foundation for more advanced epitaxial manipulation making use of new interfacial control via changes to the surface symmetry enabled by new substrates, or heterostructuring to manipulate the electrical and mechanical boundary conditions and create emergent polar order in otherwise classical ferroelectric systems. Simultaneously, advances in the understanding of synthesis and processing methods allow for the introduction of controlled chemical gradients and defect profiles to further manipulate ferroelectric response. Further pushing the boundaries of epitaxy, new hybrid structures are being explored wherein a ferroelectric perovskite is interfaced with nonperovskite materials, or where the ferroelectric is removed from the substrate entirely and studied as a freestanding membrane. Outside of the classical ferroelectrics, complex polar materials such as the relaxor ferroelectrics are now being given the epitaxial treatment, resulting in new understanding of responses to strain, electric field, temperature, and other stimuli. Leveraging close collaborations between theorists and experimentalists, research is also driving the discovery of new perovskite and nonperovskite polar materials using high-throughput methods to push materials discovery beyond the typical trial-and-error approaches. With all of these advances in synthesis, characterization, and fundamental understanding, ferroelectrics are coming full circle and finding both renewed and new interest for a range of technological applications. From the original need for high-dielectric constants, ferroelectrics are now being used in the next generation of high-frequency dielectric applications. Meanwhile, the strong optical, thermal, and mechanical responses of ferroelectrics are also being employed in a number of energy-conversion applications. Finally, the long sought-after use of ferroelectrics as critical components in a new paradigm of memory and logic components is being seriously considered.

2. Classic Epitaxy and the Study of Thin-Film Ferroelectrics

The foundations of modern thin-film-ferroelectric research were laid between the late 1980s and early 2000s—in this section, we review highlights from that era. Among other things, rapidly improving synthetic control provided a new approach for tackling problems that had limited the useful properties of ferroelectric thin films. At the same time, researchers were beginning to understand the critical roles of the various chemical, electrical, and elastic boundary conditions placed on a ferroelectric crystal in an epitaxial thin-film geometry.

2.1. What Is Epitaxy and How Are Films Made?

The great strides made in the manipulation of ferroelectric order and functionality over the last several decades have been enabled by synthetic techniques that result in epitaxial thin films. Epitaxy refers to the growth of a crystal on a crystalline substrate where the orientations of the two crystals have a specific relationship set by the interface between them. For example, assume one has a cubic substrate cut such that the [100] and [010] are in the plane and the surface normal is parallel to the [001]. Upon depositing a film of a similar structure on this surface, one might expect the [100], [010], and [001] of the film to lie parallel to those of the substrate. The result is a distinct relationship between the lattice and lattice parameters of the substrate and deposited film. A thin film is said to be coherently strained to the substrate when it adopts the same in-plane lattice parameters as the substrate throughout the thickness of the film; one can think of this as applying biaxial strain to the film. These are general examples, but other forms of epitaxy are possible. Other substrate orientations [i.e., substrates with surface orientations of, for example, the (110) or (111)] can be used to control the surface orientation of the film. In cases where the lattice mismatch between the film and substrate is too large, partially or fully relaxed films are possible wherein, above some critical thickness, the film adopts the energetically preferred bulk lattice parameters (such relaxation is accomplished by the formation of dislocations at the interface between the film and substrate). Strain and surface orientation serve as the primary means for control of a ferroelectric thin film, but the high quality associated with epitaxial deposition techniques also allows for careful control of thickness and layering, allowing the production of heterostructures and superlattices wherein precise, atomic-scale control is possible. Here, we discuss several prominent synthesis techniques used in the field to accomplish such control.

2.1.1. Pulsed-Laser Deposition

Pulsed-laser deposition (PLD) has become one of the most common methods of depositing epitaxial thin films of complex oxides. In general, PLD relies on the interaction of a focused laser beam with a ceramic (or single-crystal) target, vaporizing the target and producing a plasma that is deposited on a substrate. The light–matter interactions, however, are complex and involve equilibrium and nonequilibrium processes, and the conversion of electromagnetic energy to thermal, chemical, and mechanical energy.[2–4] The resulting plasma contains a complex distribution of ionized and excited atomic species that interact with an ambient gas (often, but not always, oxygen gas) on the way to the surface of the heated substrate. Early demonstrations of the ability to use this plasma as a source for depositing thin films were reported in the 1960s;[5] however, PLD remained a relatively obscure deposition technique limited to some semiconducting and dielectric films until the synthesis of superconducting $YBa_2Cu_3O_7$ films was demonstrated in 1987, thus allowing for the highest critical temperature in thin films reported to that point.[6,7] Since then, the ability to rapidly synthesize films in a relatively inexpensive, compact chamber has made it an attractive research technique for expanding thin-film studies to ferroelectric oxides. PLD can produce oxide thin films with extremely high crystalline quality, and when coupled with reflection high-energy electron diffraction (RHEED) (Section 3.2.1) allows for atomically precise control of oxide interfaces. The highly energetic plasma, which reaches an electron temperature on the order of 10 000 K and adatom kinetic energies that exceed 10–100 eV additionally aides in stabilizing films under far-from-equilibrium conditions. This large parameter space has allowed for the synthesis of films under large strains (Section 2.3), with controlled defect profiles (Section 3.4), and stabilizing metastable phases (Section 4.3) providing a large degree of control over ferroelectric function.

2.1.2. Molecular-Beam Epitaxy

Molecular-beam epitaxy (MBE) serves as the synthetic foil to PLD. Whereas PLD is relatively inexpensive, relies on complex laser–material interactions, is nonequilibrium in nature, and (can be) prone to defect formation in the resulting film, MBE is a relatively simple, equilibrium process which requires relatively expensive equipment but can produce some of the most pristine single crystalline specimens.[8] It should be noted that both PLD and MBE can produce films of the same quality (in the end), but in both cases, that requires careful control and attention to a range of variables. In MBE, a substrate is heated in ultrahigh vacuum and source materials are introduced (often, but not always) via effusion of single-component precursors. Shutters in front of the precursor effusion cells are used to control the flux and thus the stoichiometry of the films. The resulting films can have high purities, low defect densities and layering can be controlled at the atomic level, all of which made MBE an attractive technique for the synthesis of semiconductors through the 1970s,[9] including GaAs–AlAs quantum well superlattices with monolayer periodicity.[10] Despite proving to be a capable synthesis technique, it was not until the 1980s when the increasing interest in thin-film deposition of functional oxide materials drove the development of reactive MBE, first demonstrated for the synthesis of $LiNbO_3$ films in 1985.[11] There, a reactive gas (often and ozone/oxygen mixture) is introduced alongside the precursors to induce oxidation of species at the substrate surface. This has been used to produce a broad range of oxide compounds, including many ferroelectric systems, and is useful for synthesizing precise atomic interfaces in ferroelectric superlattices.[8]

2.1.3. Sputtering

While the above techniques are perhaps the most prominent in the studies of thin-film ferroelectrics over the last two decades, a number of other techniques, with various strengths and weaknesses, exist for the deposition of ferroelectrics.[12] Sputtering is another common technique for depositing thin-film ferroelectric oxides. It is another physical vapor deposition process, thus resembling PLD, wherein material is ejected from a target source of the desired stoichiometry and transferred to an adjacent substrate. In sputtering, the target is bombarded with high-kinetic-energy ions, typically argon, which are responsible for ejecting the target species. In order to deposit oxides, and in particular insulating ferroelectric compositions, radio-frequency (rf)-magnetron sputtering is employed along with introduction of oxygen gas, in addition to the argon that is necessary for sputtering.

2.1.4. Chemical-Vapor Deposition

Chemical-vapor deposition is of particular interest for integration of complex oxides into existing industrial processes. For example, metal–organic chemical-vapor deposition (MOCVD) is commonly used for the deposition of compound semiconductors and has been extended to oxide systems. This approach utilizes metal–organic molecular precursor gases which are flowed over a substrate where the precursors are decomposed, thus allowing the metal centers to react on the substrate surface. A similar technique, atomic-layer deposition (ALD) involves repetition of binary reaction sequences, where each sequence is a self-limiting reaction that produces a single monolayer.[13] In general, these techniques are desirable because they produce conformal films over large substrate areas free of pinholes and other defects, whereas physical vapor deposition approaches (such as sputtering and PLD) are line-of-sight. These techniques are also well-established in the semiconductor fabrication industry, and thus are often utilized in studies with a particular focus on integration into electronics, for example, studies of ferroelectricity in hafnia (HfO_2).[14]

2.1.5. Other Deposition Processes

Other routes toward synthesizing crystalline thin films involve deposition of precursors and subsequent heat treatment to crystallize the film. One common route is sol–gel deposition, where a solution containing oxide precursors is cast onto a substrate, and subsequently annealed.[15] This technique is typically much cheaper than other epitaxial-deposition techniques, but again does not typically result in the same degree of crystalline quality as MBE or PLD, and can often result in amorphous, textured, or polycrystalline films. The need for better crystalline quality and/or for depositing oxides composed of elements with high vapor pressure (e.g., indium, gallium) has made solid-phase epitaxy (SPE) popular for semiconductor synthesis.[16,17] SPE involves vapor deposition of a solid amorphous layer, followed by high-temperature solid-phase crystallization in a controlled atmosphere. This route has been used to provide better control over the stoichiometry of films containing highly volatile elements[16] or layered structures.[18]

2.2. Surfaces and Interfaces in Ferroelectric Devices

Initial interest in thin-film forms of ferroelectric oxides was driven by a desire to leverage the switchable polarization in a new generation of microelectronic memory devices.[19,20] Critical to the use of ferroelectrics in such devices was understanding and controlling switching processes. In particular, questions regarding fatigue and retention of ferroelectric polarization after many switching cycles, and long durations, as well as the impact of reducing the thickness of ferroelectrics on switching behavior were of particular focus.

2.2.1. Problems at Nonoxide Interfaces

Early films deposited on platinum-coated silicon wafers with platinum top electrodes suffered from degradation of the remnant polarization after only 10^4–10^7 switching cycles.[21,22] This "fatigue" behavior was attributed to oxygen vacancies and charge injection at the metal–ferroelectric interface.[21,23,24] Improvements were made by using oxide electrodes, such as RuO_2, IrO_2, and ultimately perovskite electrodes like $La_{0.7}Sr_{0.3}MnO_3$ and $SrRuO_3$, which prevent oxygen vacancy formation and extend the fatigue resistance to 10^{10} cycles.[23,25] Oxide electrodes also served to improve leakage properties of ferroelectric capacitors, again possibly due to the defective interface of noble metals with the ferroelectric films.[26,27] Hysteresis loops which were shifted along the electric-field axis, thus resulting in a preferred polarization state in the material, were also routinely encountered.[28,29] This so-called imprint was an obstacle to the nonvolatility promised for ferroelectric memories, and can be attributed to either internal bias fields within the ferroelectric layer,[30] or asymmetries in the ability of the electrodes to screen the polarization on either side of the capacitor. With improvements in synthesis, the increasing crystalline quality of ferroelectric films, and the growing availability of oxide substrates with appropriate lattice parameters, fully epitaxial heterostructures were soon synthesized, allowing for symmetric electrodes with improved conductivity and pristine interfaces.

2.2.2. Size Effects

One of the biggest questions regarding integration into microelectronics was how thin can a ferroelectric be made and still exhibit robust polarization? From an application-driven viewpoint, it was understood that as a crystal was thinned, the interfaces become an increasingly large fraction of the total device volume, and with that came all of the interface-driven problems described above, as well as an observed reduction of the remnant polarization. It was clear that the increasing role of the depolarization field and gradient energies in reduced dimensions could result in the formation of a polydomain state that limited the usable (switchable) remnant polarization. It remained unknown whether this destabilization could

be so dramatic as to quench ferroelectric order entirely. In fact, researchers, for a number of years, had reported the absence of a ferroelectric transitions in $BaTiO_3$, $PbTiO_3$, and $PbZr_xTi_{1-x}O_3$ in ultrafine grained ceramic samples below some critical thickness,[31–34] yet the precise value of this critical thickness was disputed and varied between 10 and 100 nm across different studies.

Theoretical approaches, on the other hand, had consistently concluded that ferroelectricity should persist to thinner films than were being experimentally realized. A number of early treatments using phenomenological or mean-field approaches considered the effects of depolarization, screening, and anisotropic correlation, resulting in critical thicknesses between 5 and 50 nm depending on composition.[35,36] The experimental measurement of polarization in a 40 Å $PbZr_{0.2}Ti_{0.8}O_3$ thin film deposited via rf sputtering, however, prompted a reassessment of these theoretical results.[37] First-principle calculations were subsequently employed, first utilizing an effective-Hamiltonian,[38] and eventually full density-functional theory (DFT) approaches to simulate isolated slabs of both $PbTiO_3$ and $BaTiO_3$.[39] These results were able to provide more material-specific and microscopic details compared to earlier phenomenological treatments. Moreover, by the early 2000s, computational capabilities had advanced to the point where supercells of ≈100 atoms could be simulated, amounting to a maximum of ≈20 unit cells, and thus the study of size effects appeared to be ideally suited to such theoretical approaches. These studies resulted in critical understanding of the importance of the electrical boundary conditions as well as the effect of different surface reconstructions that could impact the stabilization of ferroelectric polarization, and ultimately suggested that ferroelectricity could be stable down to just a few unit cells. In 2003, simulations of $SrRuO_3/BaTiO_3/SrRuO_3$ heterostructures[40] with electrodes with realistic carrier densities resulted in incomplete screening of the ferroelectric polarization, and ultimately a larger critical thickness of 8 unit cells (**Figure 2**a). Subsequent studies have highlighted the importance of both chemical and electrical boundary conditions, suggesting that with perfect screening and chemical termination, ferroelectricity could be stabilized in films as thin as just 2 unit cells.[41]

The discrepancy between early experimental studies on size effects and the theoretical results suggesting stable ferroelectricity was ultimately attributed to the influence of defects or impurities, or poorly defined electrical and mechanical boundary conditions in ultrafine-grained polycrystalline samples. But, just as computational capabilities were expanding to be able to handle large enough supercells, epitaxial deposition was allowing for even thinner ferroelectric films to be studied. Measuring the electrical properties of ultrathin films, however, is difficult due to problems with leakage current masking the switching current. In 2004, a novel approach utilizing in situ X-ray diffraction during MOCVD deposition of $PbTiO_3$ on a $SrTiO_3$(001) substrate demonstrated the presence of ferroelectric 180° domains in films as thin as 3 unit cells, with only a moderate decrease of Curie temperature, T_C (Figure 1), for films 4 unit cells and larger.[42] This result was in good agreement with predictions from first principles,[38,39] and suggested a simple mechanism invoking reconstructions in the outermost unit cells on each side of the film, leaving a single, middle unit-cell which can maintain a polar distortion (Figure 2b). While promising, this study still did not achieve the monopolar polarization desired for applications, and further thin-film-based studies continued to probe this possibility. Soon, studies on 5 nm thick $BaTiO_3$ films with $SrRuO_3$ electrodes were reporting polarization–electric field hysteresis loops and persistent tetragonality, albeit with reduced remnant polarization.[43] This was again attributed to the formation of polydomain states in the absence of an applied field, due to imperfect screening at the interfaces. In another case, monopolar polarization was reported in 3 unit cell thick films of $PbTiO_3$ utilizing $SrRuO_3$ bottom electrodes and the stability was attributed to environmental adsorbates that could appropriately screen and thus stabilize the polarization.[44] Eventually, heterostructures were imaged using high-resolution transmission microscopy (HR-TEM) and researchers were able to directly image the ferroelectric distortion across the thickness of the film, demonstrating a progressive decrease of the polar distortion in unit cells near the electrode interface.[45,46] In the case of size effects, work continues to push the limits of practically applicable polarization in ultrathin films, and as the work on epitaxial films demonstrates, the interfaces are critically important for maintaining a stable, monopolar polarization in a ferroelectric crystal.

2.3. Epitaxial Strain Enables New Ferroelectric Manipulation

As the study of size effects in ferroelectrics advanced, the critical role of epitaxial strain was becoming more apparent. The piezoelectric nature of all ferroelectrics is a clear indication that stresses applied to a ferroelectric crystal should manipulate the polarization, and as early as the 1950s, experiments were demonstrating that the application of hydrostatic pressure to ferroelectric crystals could change the T_C.[47] In the 1990s, various calculations began suggesting mechanical manipulation could provide an incredible degree of control over ferroelectric order. With developments in epitaxial deposition, a growing selection of commercially available oxide substrates, and strong motivation from theory, thin-film scientists began to push the boundaries of synthetic control and understanding of ferroelectric thin films.

2.3.1. Predicting Strain Effects in Ferroelectric Thin Films

As soon as researchers began to study ferroelectrics as thin films, it was realized that these films exhibited dramatically different properties than their bulk counterparts. Separate from the question of confining the polarization to an increasingly thin slab of material, was the question of how the mechanical boundary conditions imposed by the semi-infinite substrate may change ferroelectric responses. Early understanding of the effect of misfit strain in thin films was developed in the late 1990s via thermodynamic phenomenology based on Ginzburg–Landau–Devonshire (GLD) models. These studies produced some of the first misfit strain–temperature phase diagrams for common ferroelectrics such as $BaTiO_3$[48,49] and the $PbZr_xTi_{1-x}O_3$ system,[50] demonstrating that misfit strain

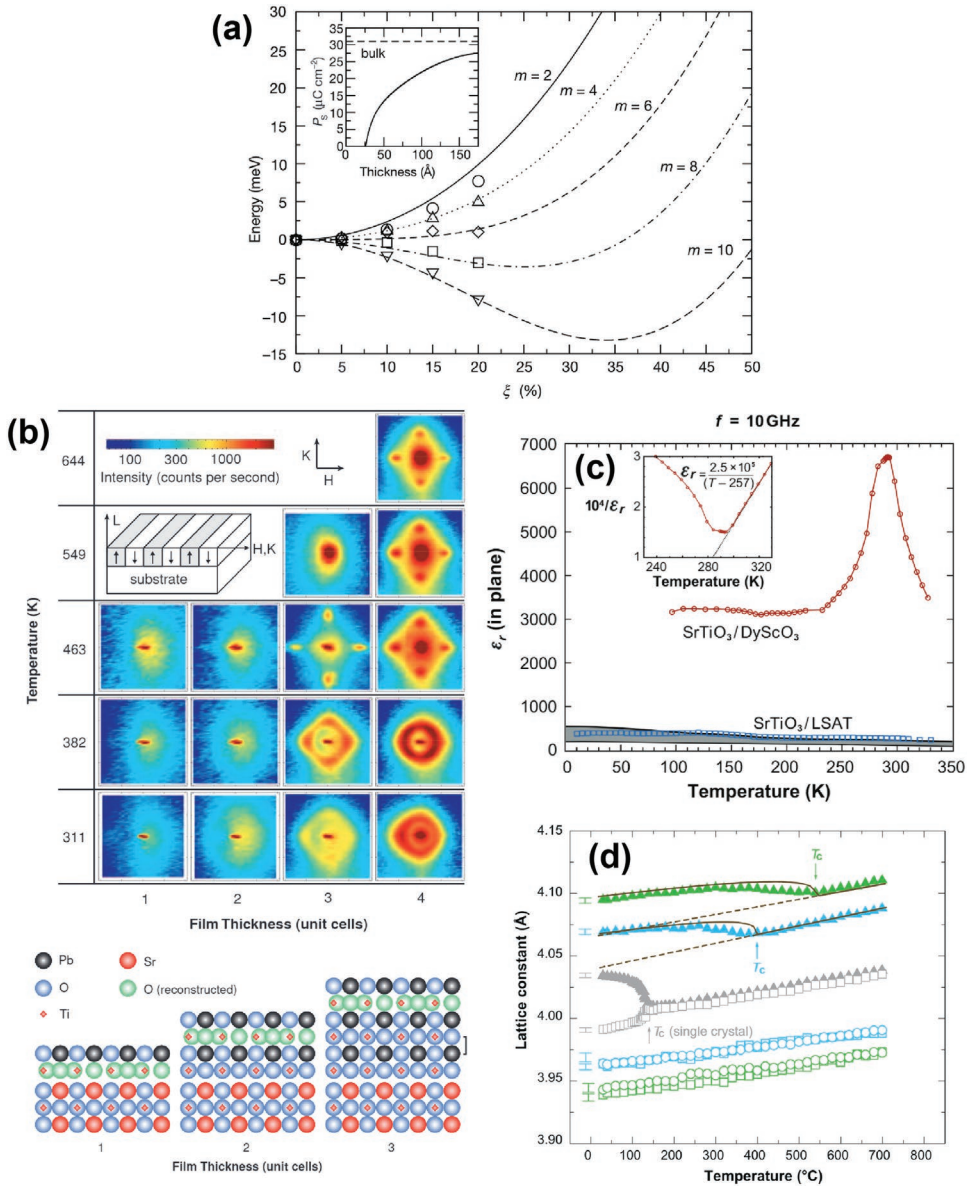

Figure 2. a) Evolution of the energy as a function of the soft-mode distortion ξ for different thicknesses of the ferroelectric thin film. The magnitude of ξ is the percentage of the soft-mode displacements of $BaTiO_3$ atoms in bulk ($\xi = 1$ corresponds to the distortion of the bulk tetragonal ferroelectric phase). The inset shows the evolution of the spontaneous polarization, P_s, with thickness. Reproduced with permission.[40] Copyright 2003, Springer Nature. b) (Top) In-plane diffuse X-ray scattering profiles about the $PbTiO_3$ 303 diffraction condition as a function of film's thickness (1–4 unit cells) and temperature (311–644 K). In each case, the scattering profile extends ±0.2 reciprocal lattice units in the in-plane reciprocal space coordinates H and K. The inset shows the ferroelectric phase of $PbTiO_3$ showing alternating polarity in its domain structure. (Bottom) Schematic of $PbTiO_3$ films 1 to 3 unit cells thick with the top unit cell reconstructed. The 3 unit cell film is the thinnest film having PbO and TiO_2 layers with the nearest neighbor environment of bulk $PbTiO_3$ (indicated by bracket). Reproduced with permission.[42] Copyright 2004, American Association for the Advancement of Science. c) In-plane dielectric constant (ε_r) in strained epitaxial $SrTiO_3$ films as a function of temperature at a measurement frequency $f = 10$ GHz of 500 Å thick $SrTiO_3$/(110)$DyScO_3$ and $SrTiO_3$/(100)$(La_{0.18}Sr_{0.82})(Al_{0.59}Ta_{0.41})O_3$ epitaxial films. These films are under biaxial tensile and compressive strains, respectively. The peak in ε_r of about 7000 indicates that the T_C of $SrTiO_3$ under biaxial tension of $\varepsilon_s = 0.008$ is about 293 K. The inset shows a Curie–Weiss fit to $1/\varepsilon_r$. The shaded region in corresponds to the expected value of the in-plane ε_r for a $SrTiO_3$ film commensurately strained to $La_{0.18}Sr_{0.82})(Al_{0.59}Ta_{0.41})O_3$ ($\varepsilon_s = -0.009$), based on thermodynamic analysis and the range of relevant reported property coefficients for $SrTiO_3$. Reproduced with permission.[64] Copyright 2004, Springer Nature. d) Temperature dependence of the lattice parameters of single-crystal $BaTiO_3$ and strained $BaTiO_3$ thin films grown by MBE on $DyScO_3$ (green data points) and $GdScO_3$ (blue data points) substrates. The in-plane (square) and out-of-plane (triangle) lattice constants of the $BaTiO_3$ thin films and underlying substrates (circle) are shown. The change in slope at high temperature signals a phase transition. The error bars (± standard deviation) of the measured lattice constants are shown at the left edge of each curve. The measured values of the out-of-plane spacing of biaxially strained $BaTiO_3$ are compared with theoretical predictions with (solid line) and without (dashed line) a ferroelectric transition. Reproduced with permission.[65] Copyright 2004, American Association for the Advancement of Science.

allowed for unprecedented control over ferroelectric order, including shifts of the T_C of hundreds of degrees, as well as stabilization of low-symmetry ferroelectric phases that had not been reported in the bulk (e.g., orthorhombic $BaTiO_3$ and rhombohedral $PbTiO_3$).[48] Additionally, these studies predicted strain-induced ferroelectric transitions in otherwise non-ferroelectric cubic systems such as $SrTiO_3$.[51] Phenomenological approaches, however, require the use of experimentally determined properties, including dielectric stiffness, electrostrictive coefficients, and elastic compliances, to produce accurate results, and the lack of this information thus limited the materials systems and temperature ranges that could be reliably studied with these methods.

Early phenomenological results motivated a wave of theoretical studies attempting to tackle the question of strain effects in ferroelectrics, particularly first-principle approaches that did not rely on such experimentally measured parameters. In the early 1990s, first-principle DFT calculations had begun to be employed to study the lattice dynamics of $BaTiO_3$,[52] electronic contributions to ferroelectricity in $BaTiO_3$ and $PbTiO_3$,[53] and to calculate the phonon and band structures of a number of ferroelectric perovskites.[54] These studies noted that results were strongly dependent on unit-cell volume, supporting the idea that ferroelectric properties could be dramatically altered via the application of strain.[52,53] By the early 2000s, DFT approaches were utilized to directly probe the effect of strain on lattice structure, atomic displacements, and polarization in a number of perovskite systems.[55–58] In general, compressive strain was shown to increase the out-of-plane polarization of many ferroelectric thin films, whereas tensile strain could progressively rotate the polarization from out-of-plane to in-plane, as the ferroelectric adopted lower-symmetry monoclinic, orthorhombic, and/or rhombohedral polymorphs, similar to those predicted via phenomenological calculations, resulting in even larger changes to the magnitude of polarization. Interestingly, however, strong strain dependence was not found to be universal to all systems. $BiFeO_3$, for example, was found to undergo antiferrodistortive rotations under compressive strain that destabilize the ferroelectric distortion.[59] Extending first-principle studies to non-ferroelectric perovskites again resulted in reports of strain-induced ferroelectric phases in $SrTiO_3$, as well as other non-ferroelectric titanates (e.g., $CaTiO_3$[60] and $EuTiO_3$[61]) and several manganite systems (e.g., $BaMnO_3$[62] and $CaMnO_3$[63]). In addition to providing critical insight in ferroelectric physics, these studies served as motivation for researchers to begin synthesizing epitaxial ferroelectric thin films under a variety of strain states.

2.3.2. Control of Ferroelectric Phases through Epitaxial Strain

Through the late 1980s and 1990s, increased understanding and experience with oxide epitaxy had driven the production of increasingly high-quality thin films of ferroelectric materials, but it was the continual development and increasing commercial availability of novel single-crystal substrates (e.g., $SrTiO_3$ and the rare-earth scandates) and the subsequent access to the appropriate substrates to synthesize ferroelectrics under a range of misfit strain conditions that accelerated the field. The earliest confirmation of theoretical predictions of a ferroelectric transition in the common dielectric was for $SrTiO_3$,[64] which, despite its chemical similarity to the robust ferroelectric $BaTiO_3$, remains cubic and nonpolar down to 0 K due to quantum fluctuations that stabilize the soft-mode frequency associated with ferroelectric instability (thus leading to it being called an incipient ferroelectric). In 2004, $SrTiO_3$ films deposited via MBE on the newly available $DyScO_3$(110) substrate allowed for the application of +1% biaxial tensile strain and resulted in a ferroelectric transition being observed along with enhanced dielectric response and large dielectric tunability (Figure 2c). Almost simultaneously, were reports of enhanced ferroelectricity in $BaTiO_3$ thin films deposited on $GdScO_3$(110) and $DyScO_3$(110) substrates;[65] the lattice parameters of the substrate here impart an epitaxial compressive strain of –1.0% and –1.7%, respectively. These films demonstrated increased c/a lattice-parameter ratios as well as enhanced T_C of 400 and 540 °C for films on $GdScO_3$(110) and $DyScO_3$(110) substrates, respectively, much larger than the T_C of 130 °C for bulk single crystals (Figure 2d). In addition to enhanced ferroelectricity, new ferroelectric phases were discovered in thin films. One of the most significant results from this work was the synthesis of $BiFeO_3$ thin films on $YAlO_3$(001) substrates, amounting to the imposition of a massive biaxial compressive strain on the parent phase of $BiFeO_3$ of –6.6%.[66] With this large compressive strain, the $BiFeO_3$, which is typically a rhombohedral ferroelectric with the polar axis aligned along the <111>, is driven into a nearly tetragonal symmetry (it is actually monoclinic, but very close to tetragonal) and exhibits a large enhanced polarization. These discoveries served as the initial evidence that theoretical predictions of strain-induced ferroelectric phases could be experimentally realized via epitaxy and have since driven an entire field of theory-guided searches for novel ferroelectric phases stabilized by epitaxy which will be discussed later in this review (Section 4.3).

2.4. Domain-Structure Control

One of the hallmarks of ferroelectrics physics and functionality is the possibility of the formation of complex hierarchical domain structures (**Figure 3**).[67] Through thin-film epitaxy, a range of complex, nanostructured domain morphologies have been experimentally realized and studied. The understanding and utilization of these domain structures has been enabled by advances in both theoretical approaches, including the development of phase-field and molecular dynamics simulations, as well as scanning-probe-microscopy techniques.

2.4.1. Simulating Domain Structures and the Need for Mesoscopic Models

The strain–temperature phase diagrams initially produced by phenomenological and first-principle studies focused on single-phase ferroelectric transitions.[48] Even these early studies, however, acknowledged that at certain conditions, a coexistence of multiple ferroelectric phases should provide the lowest energy state. Subsequent studies allowing for phase coexistence began

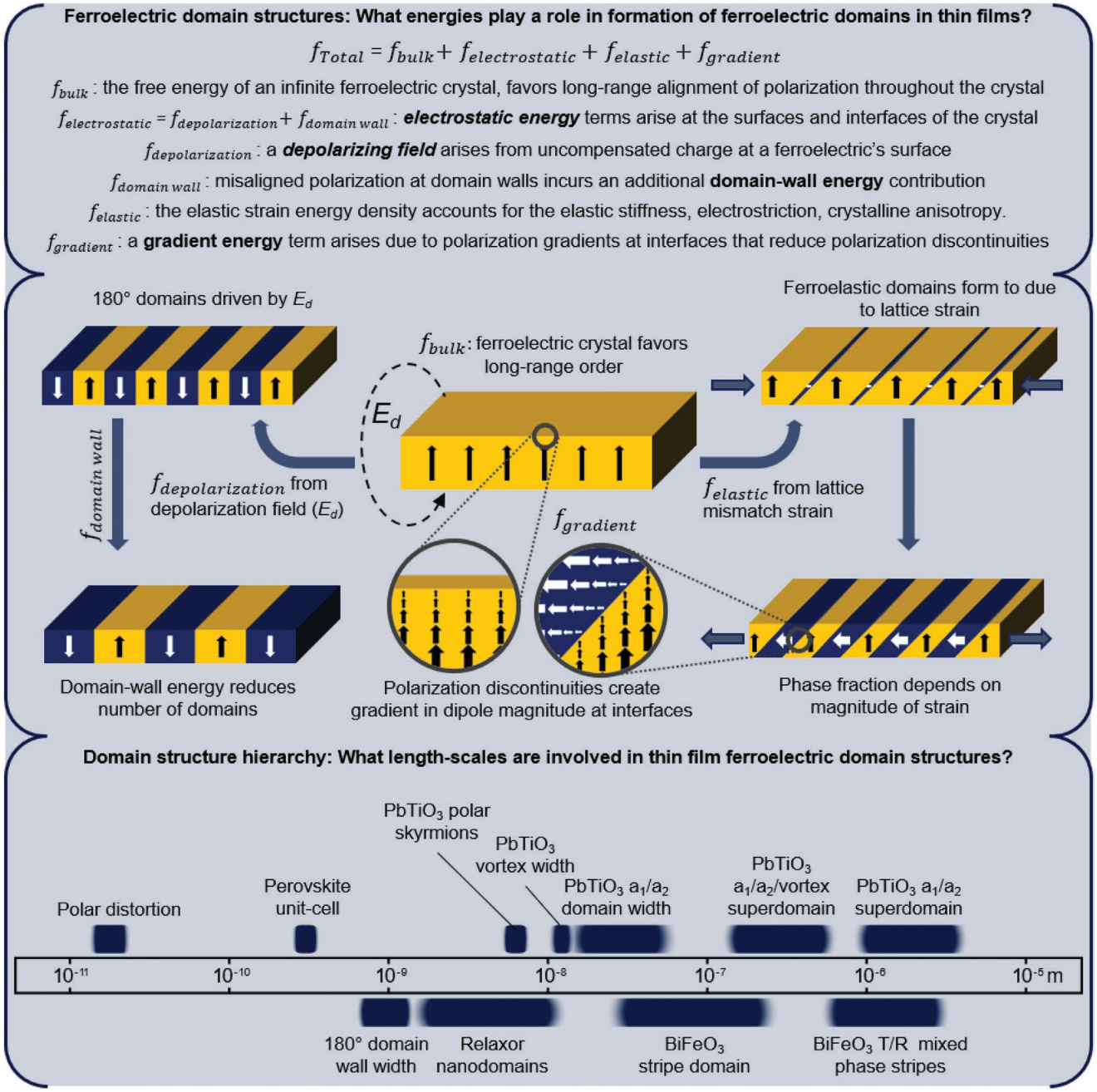

Figure 3. Top) Understanding the energies involved in the evolution of ferroelectric domain structures. Middle) Schematic illustration of different types of domain structures and which energies are important in their formation. Bottom) Number line showing the relative size of different common distortions and domain structures in ferroelectrics.

to produce increasingly complex phase diagrams. For example, early calculations of single-phase $PbTiO_3$ predicted a rhombohedral phase for moderate to large tensile strains.[48,49] With later calculations including phase coexistence, this phase was replaced with a larger region of c/a domains (i.e., coexistence of tetragonal phases with polarization along out-of-plane c and in-plane a directions) which extended into compressive strains as well.[57,68] Similarly, the orthorhombic phase, with polarization along [110], was replaced by a_1/a_2 domains (i.e., coexistence of tetragonal phases with polarization along both the in-plane [100] or [010]). Meanwhile, in $BaTiO_3$, it was predicted that even more complex structures could form, with coexisting regions of c/a domains and a_1/a_2 domains.[69] Standard phenomenological approaches, however, were limited to predicting which ferroelectric phases would form, but provided little information regarding how the resulting domain structures would be distributed in real space. Likewise, the limited cell size that could be handled by first-principle calculations (at the time and even today) made calculating mesoscopic domain structure untenable. To address these gaps, researchers developed phase-field

calculations,[70] which simultaneously accounted for the inhomogeneous dipole–dipole and elastic conditions that arise in a material with a complex domain structure, and included time dependence within the established GLD framework.[71–73] These studies provided mesoscale simulations, allowing researchers to develop a real-space picture of domain structures, and observe the evolution of those domain structures through the various ferroelectric phase transitions. In the mid-1990s, such simulations were used to study the evolution of 180° and 90° domains in 2D,[71,73] but soon developed to allow for full 3D simulations of complex domain structures as a function of strain and temperature.[74] For example, the strain–temperature phase diagram for $BaTiO_3$ exhibits multidomain regions of tetragonal, rhombohedral, orthorhombic, and monoclinic phases with several regions of phase coexistence (**Figure 4**a).[75] 3D domain structures simulated for such regions show hierarchical organization with complex twinning patterns (Figure 4b). An additional benefit of phase-field approaches is the ability to extract individual electrostatic, elastic, gradient, and bulk energy values (Figure 3), providing further insight as to driving forces for various domain configurations.

In parallel, first-principle-based molecular-dynamics simulations were being developed to extract atomistic insight from phenomena associated with mesoscopic domain structures. While the requirement of well-developed material-specific interatomic potentials limits the scope of molecular dynamics, such simulations provide critical insight into the dynamics of ferroelectrics under several applied stimuli. For example, in the late 1990s, the strongly displacive nature of the phase transition in $PbTiO_3$ was brought into question, yet it was not until the development of bond-valence molecular dynamics model of $PbTiO_3$ in 2005 that the order–disorder characteristics could be simulated and observed via local displacements of lead and titanium ions in the paraelectric phase.[76] Further developments allowed for the simulation of domain-wall nucleation and growth in $PbTiO_3$, providing atomic-scale descriptions of individual dipole dynamics under the application of an electric field.[77] Both molecular-dynamics and phase-field simulations have since become critical components of thin-film-based studies of ferroelectric-domain structures, including the understanding of domain formation, transitions, dielectric contributions, and switching dynamics.

2.4.2. Scanning-Probe Microscopy

Just as phase-field and molecular-dynamics simulations filled the gap in mesoscale simulation capabilities, scanning-probe microscopy served the same role for experimentalists probing thin films with complex domain structures. X-ray diffraction can provide macroscopic symmetries for various phases and transmission electron microscopy can provide an ultralocal atomic picture of the structural relationships at domain-wall boundaries. Scanning-probe-microscopy techniques, on the other hand, allow one to probe things at mesoscopic length scales by measuring the interaction of a nanometer sized cantilever probe with the surface of a thin film over regions tens to hundreds of micrometers across. Simple measurements of surface topography, called atomic force microscopy (AFM), rely on electrostatic interactions between the probe and sample surface. Piezoresponse force microscopy (PFM) allows for imaging of ferroelectric domains by electrically driving the material with an AC voltage and measuring the mechanical response induced by the converse piezoelectric effect.[78,79] Measuring PFM both vertically (perpendicular) and laterally (parallel) to the sample surface provides for imaging of domain structures with polarization in 3D.[80] Manipulation of a ferroelectric domain structure is also possible through application of a DC electric field via the probe tip, which can be used to write, and subsequently read, poled ferroelectric regions of arbitrary shape and size. The growing complexity and functionality of thin-film-enabled domain structures have driven even more advanced techniques for characterizing ferroelectric surfaces. For example, conductive AFM has been used to image the conductivity of a sample at the nanometer length scale and has demonstrated, among other things, the presence of conductive domain walls in some ferroelectrics.[81–83] Meanwhile, the complex dynamics of ferroelectric domain walls are now increasingly being studied using band-excitation piezoresponse spectroscopy (BEPS) wherein the excitation and response of the cantilever is expanded to a larger bandwidth for nanoscale mapping of the energy dissipation associated with ferroelectric switching.[84–86]

2.4.3. Discovering and Engineering Complex Domain Structures

The above techniques provided the means for probing and understanding the increasingly complex domain structures being produced in epitaxial thin films. Whereas $BaTiO_3$ has been predicted to exhibit a rich domain evolution with strain, the lack of suitable oxide substrates has limited the realization of such structures. On the other hand, the relatively smaller lattice parameters of $PbTiO_3$-based systems allow for coherently strained films to be produced under a variety of strain states. Early experiments demonstrated the predicted domain evolution in $PbTiO_3$ from monodomain c to polydomain c/a and finally to polydomain a_1/a_2 structures as one moves from compressive to tensile strain with X-ray diffraction and electron microscopy.[87,88] Ultrathin $PbTiO_3$ films used to probe size effects often resulted in the formation of well-ordered 180° c domains with thickness-dependent periodicity.[89] Reducing the thickness of $PbZr_{0.1}Ti_{0.9}O_3$ films under tensile strain was found to result in ultrafine nanodomain patterns with 10 nm periodicity that extend tens of micrometers across the sample.[82,90] Other complex nanodomain structures have been found in films of $Pb_{1-x}Sr_xTiO_3$, where hierarchical a_1/a_2 domain structures were achieved with nanoscale domain ordering of 90° domain walls and mesoscale regions where domain orientation changes by 180°.[91] More recently, $PbTiO_3$ films grown on $GdScO_3$(110) substrates have been observed to have coexisting c/a and a_1/a_2 regions with a complex mesoscopic ordering, as predicted by GLD models (Figure 4c).[85]

In $BiFeO_3$, the rhombohedral crystal structure and resulting eightfold degeneracy of the <111>-type polarization results in complex domain structures that depend strongly on both misfit strain as well as substrate symmetry and vicinality. Compared to the relatively simple 90° and 180° domain walls observed in strongly tetragonal systems like $PbTiO_3$, rhombohedral $BiFeO_3$

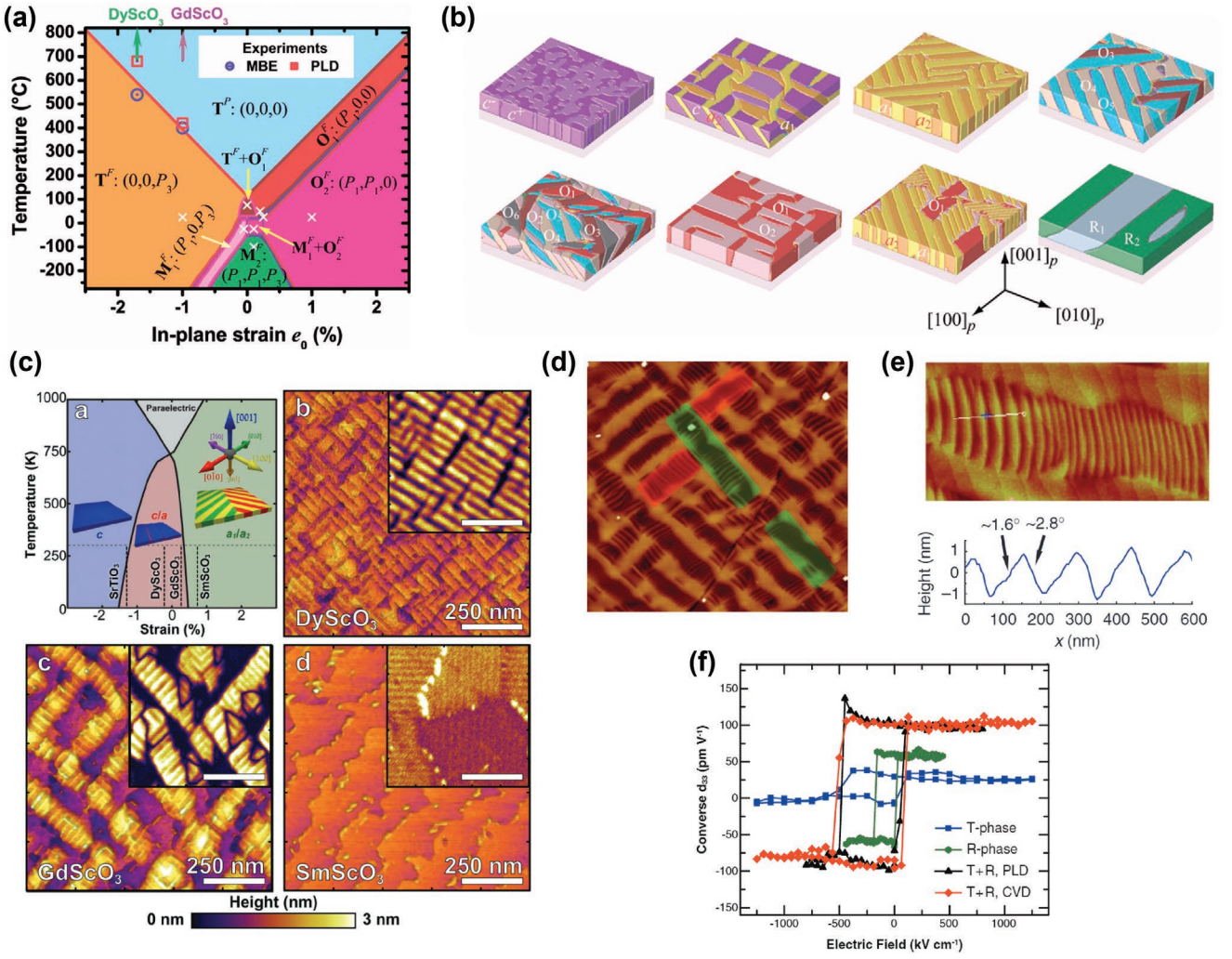

Figure 4. a) Phase diagram of $BaTiO_3$ films as a function of temperature and substrate constraint strain. T^P—tetragonal paraelectric, T^F—tetragonal ferroelectric, O^F—orthorhombic ferroelectric, and M^F—monoclinic ferroelectric. The symbol (×) indicates the locations of the domain structure. Reproduced with permission.[75] Copyright 2006, American Institute of Physics. b) Representative domain morphologies in $BaTiO_3$ films within different domain stability fields. Domain definitions: a_1: (P_1,0,0); a_2: (0,P_1,0); c^+: (0,0,+P_3); c^-: (0,0,–P_3); R_1: (–P_1,–P_1,P_3); R_2: (P_1,–P_1,P_3); O_1: (P_1,P_1,0); O_2: (P_1,–P_1,0); O_3: (P_1,0,P_3); O_4: (P_1,0,–P_3); O_5: (0,P_1,P_3); O_6: (0,P_1,–P_3). a) T^F at T = 25 °C and e_0 = –1.0%; b) $T^F + O_1^F$ at T = 75 °C and e_0 = 0%; c) O_1^F at T = 50 °C and e_0 = 0.2%; d) $T^F + O_1^F$ at T = 25 °C and e_0 = –0.05%; e) O_2^F at T = 25 °C and e_0 = 0.1%; f) O_2^F at T = 25 °C and e_0 = 1%; g) $O_1^F + O_2^F$ at T = 25 °C and e_0 = 0.25%; h) M_2^F at T = 0 °C and e_0 = 0.1%. Reproduced with permission.[70] Copyright 2008, The American Ceramic Society. c) Analytical phenomenological modeling-based temperature–strain phase diagram revealing the stability regimes for c, c/a, and a_1/a_2 domain structures. Strain positions for the substrates used are shown as dashed lines in (a). (b–d) Topography and out-of-plane piezoresponse amplitude (inset) of $PbTiO_3$ films grown on $DyScO_3$ (b), $GdScO_3$ (c), and $SmScO_3$ (d) substrates. Reproduced with permission.[85] Copyright 2017, Wiley-VCH. d,e) Atomic force microscopy topography image of mixed phase $BiFeO_3/LaNiO_3$ heterostructures. Red and green shaded areas indicate two sets of mixed phase features oriented at 90° to each other. d) High-resolution atomic force microscopy topography image of a mixed phase structure. e) Cross-section line profile along the white line in (d). Rhombohedral (R)- and tetragonal (T)-like phases show different slopes of ≈1.6° and ≈2.8°. d,e) Reproduced with permission.[97] Copyright 2011, Springer Nature. f) Piezoelectric hysteresis loops from T-like (blue curve), R-like (green curve), and mixed-phase (purple and red curves) $BiFeO_3$ thin films, grown by pulsed laser deposition (PLD) and chemical vapor deposition (CVD), measured in capacitors with a diameter of 32 µm. Reproduced with permission.[95] Copyright 2011, Springer Nature.

can possess 71° and 109° domain walls which lie in {101} and {100}, respectively, in addition to 180° domain walls. When deposited on a cubic substrate (e.g., $SrTiO_3$(001)), $BiFeO_3$ films adopt a domain structure with four polarization variants, with striped-domain patterns of 71° domain walls running parallel to both the [100] and [010] (i.e., rotated 90° in-plane with respect to each other). Reducing the surface symmetry of the substrate, either through lattice parameter anisotropy or increased substrate miscut, can result in a selection of only one set of stripes (i.e., formation of a two-variant polarization state).[92–94] At larger compressive strains, the coexistence of the strain-induced tetragonal-like (Section 2.3.2) and normal rhombohedral $BiFeO_3$ creates complex mixed-phase domain structures with striped regions with 30–50 nm periodicity (Figure 4d,e).[66,95–97]

The ability to control and produce, in an on-demand fashion, such complex domain structures has afforded unprecedented

control over the properties of ferroelectrics. In $PbZr_xTi_{1-x}O_3$, for example, researchers have shown that such domain structures provide large contributions to both the dielectric and pyroelectric responses.[98–100] Domain engineering has also enabled control over switching pathways by stabilizing intermediate states. In both c/a and a_1/a_2 structures, 90° switching of the polarization has been observed in both in-plane and out-of-plane geometries, suggesting the possibility for "beyond-binary" control of polarization.[85,90] In $BiFeO_3$, control of domain structure enables new low-energy switching pathways involving successive ferroelastic 71° and 109° switching events that circumvent the higher energy ferroelectric 180° switching pathway. Synthesizing ferroelectrics with compositions near the boundary between two distinct crystal symmetries, also known as a morphotropic phase boundary (MPB), has long been a prevailing route for achieving large electromechanical responses. The formation of strain-induced mixed-phase domain structures, on the other hand, has unlocked these large electromechanical effects in materials outside of the typical MPB compositions. Electric-field interconversion between rhombohedral and tetragonal-like phases in $BiFeO_3$ films, for example, was shown to induce large lattice strains (Figure 4f).[66,95] More recently, work has achieved similarly large responses via interconversion a_1/a_2, c/a, and c domains in strained $PbTiO_3$ films.[85] Finally, strain and symmetry constraints imposed via epitaxy have enabled domain structures with conducting domain walls due to carrier accumulation necessary to screen discontinuities in polarization.[82,83,95,101]

3. Advanced Epitaxy and Beyond

The highlights noted in Section 2 represent some of the most influential works in the space spanning the period from (roughly) the mid-1980s to the mid-2000s. These studies have laid the foundational understanding of thin-film ferroelectrics and the groundwork for a number of novel structures and functionalities that are currently under study. In this section, we transition to focus on more recent advances (primarily in the last decade) which have been made by controlling substrate symmetries, ferroelectric interfaces and heterostructures, and controlled chemical and defect profiles. These approaches show how the field has evolved in recent times and what innovation in epitaxial constraint can do to open up new understanding of ferroelectric physics and functionality.

3.1. Orientations beyond (001)

The vast majority of studies on epitaxial thin-film ferroelectrics have been done on (001)-oriented films (be they tetragonal or otherwise ferroelectric). While this does much to simplify such work (in the case of a tetragonal ferroelectric, this can often produce films with all or the majority of the material with the polarization aligned normal to the substrate), it imposes significant limitations on what researchers can study and what can be achieved. It is well understood from single-crystal measurements that materials probed along directions other than their polarization axes exhibit different behaviors, such as enhanced dielectric and piezoelectric responses.[102,103] While such studies are relatively simple for single crystals, typical thin-film device geometries are limited to those done out or in the plane of the film, thus disallowing electrical measurements at intermediate angles. It has also been shown that the surface symmetry of the substrate can alter a number of important properties, including domain structure, dielectric response, phase stability, and polarization;[92,104–108] much of which remains unexplored due to the limitations in studies beyond (001)-oriented films.

DFT studies of (111)-oriented $PbTiO_3$ and $BaTiO_3$[106] revealed interesting phase behavior with important implications for their properties. Under tensile strains greater than 0.2%, $BaTiO_3$ was predicted to adopt a *Cm* symmetry with a slightly reduced (5–10 μC cm^{-2} lower) polarization compared to the bulk, *R3m* phase. Under –0.4% compressive strain, ferroelectricity was fully suppressed due to the formation of a nonpolar *Rm* phase. This suppression has been observed in compressively strained (111)-oriented $BaTiO_3$,[109,110] though this could also be attributed to a cell-doubling transition, which was not considered in the DFT calculations. $PbTiO_3$, instead, adopts an *R3m* phase under compressive strain and relaxes to a monoclinic phase with *Amm2* symmetry. Another monoclinic phase resembling the bulk *P4mm* symmetry was not seen until about 0.3% tensile strain, as the constraints of the (111)-oriented substrate inhibit tetragonal elongation at lower strains. At even larger tensile strains (above 0.8%), a third monoclinic phase is favored due to a lower elastic enthalpy. Unlike $BaTiO_3$, the calculated polarization for (111)-oriented $PbTiO_3$ films did not vary significantly with strain.

Experimental studies on (001)-, (101)-, and (111)-oriented $PbZr_{0.2}Ti_{0.8}O_3$ films revealed that (111)-oriented films form a nanotwinned domain structure with a high density of 90° domain walls due to degeneracy between the *a* and *c* domains caused by the symmetry imposed by the substrate, which, in turn, led to a threefold increase in permittivity.[111] This enhanced permittivity was attributed to both an enhanced intrinsic response and a large contribution from the material within the finite volume of the domain walls—a so-called "frozen" contribution since the domain walls do not move, but simply offer increased response due to an increased susceptibility of the material within the domain walls. Subsequent polydomain GLD calculations on this system supported the notion that different film orientations set the relative amount of intrinsic and extrinsic contributions to permittivity.[104] Specifically, (111)-oriented films exhibit the highest intrinsic contribution, followed by (101)- and (001)-oriented films, due to the larger dielectric response along the [100] in $PbZr_{0.2}Ti_{0.8}O_3$. The reverse is true for the extrinsic contributions, which vanish entirely for (111)-oriented films. The origin of this stationary domain wall contribution was later confirmed through molecular-dynamics simulations that demonstrated that the dipoles within these domain walls experienced stronger fluctuations under subswitching fields than dipoles within the domains.[112] These calculations also show a reduction in the stability of the parent tetragonal phase in (101)- and (111)-oriented films, which instead tends toward monoclinic and rhombohedral phases.[107,108] Whereas typical ferroelectrics have been shown to follow the empirical Janovec–Kay–Dunn (JKD) law, wherein the coercive scales inversely with film thickness (specifically

$E_c \propto d^{-2/3}$), the transition to a low-symmetry monoclinic phase at reduced thickness in (111)-oriented films was shown to subvert typical JKD-scaling and (111)-oriented films maintained relatively low coercive fields at reduced thickness.[113] In addition to reduced thickness scaling, (111)-oriented films were found to adopt alternative switching pathways owing to the stabilization of 90° domain walls. PFM and pulsed hysteresis measurements demonstrated kinetically stabilized multistate switching enabled by successive 90° ferroelastic switching events. Molecular-dynamics simulations confirmed that while (001)- and (101)-oriented films exhibit 180° switching, the epitaxial strain stabilized 90° multistep switching in (111)-oriented films due to the elastic cost of rotating the polarization through the more typical 180° pathway.[114] Using substrate-induced symmetry to confine polarization enables engineering of low-energy switching pathways and multistate functionality in ferroelectrics.

3.2. Controlling Polarization with Superlattices and Interfaces

Advances in deposition techniques have allowed for the production of complex-oxide heterostructures with atomic-level control and an increasing number of studies aimed at taking advantage of interfacial engineering to produce emergent properties.[115–117] In general, such emergent properties are created from the interplay between the fundamental spin, charge, orbital, and lattice degrees of freedom in thin-film heterostructures which are counterpoised via unit-cell level stacking to produce states not seen in nature. Perovskites, in particular, have been widely used as a building block of such artificial heterostructures due to their structural similarity and chemical versatility. Using the plethora of perovskite materials as building blocks, the effects of size, strain, symmetry, and depolarization can be manipulated and such heterostructures have become the subject of much attention in the ferroelectric community.[118]

3.2.1. Complex-Oxide Heterostructures with RHEED-Assisted Growth

Synthesis of atomically abrupt (or nearly so) interfaces is aided by in situ monitoring of the deposition process. While RHEED had been used in the deposition of semiconductor materials for decades, the development of differentially pumped setups that allow for the electron beam to be introduced into the relatively high-pressure growth environments needed for oxides has only really changed the landscape for those working on these materials in the last two decades.[115] RHEED is the combination of reflection and diffraction from the growing film surface, and the measured intensity is proportional to the surface sharpness and crystallinity, allowing for measurement of the completion of a single atomic layer.[119] As layer-by-layer growth progresses, the RHEED intensity oscillates allowing atomic-scale control of the number of unit cells deposited. Control of the deposition of different materials at the unit-cell level provides a pathway to construct high-quality superlattices with atomically precise interfaces.

3.2.2. Asymmetric Superlattices and Ferroelectric Proximity Engineering

The atomic-scale engineering associated with the superlattice approach has enabled new methods for enhancing ferroelectric properties, new avenues for multifunctional coupling, and other means of creating emergent ferroic properties.[115] One example is the creation of asymmetric superlattices, wherein repeating trilayer units (rather than the more typical bilayer units) enables one to artificially break inversion symmetry at the unit-cell level.[120,121] As early as 2000, first-principle simulations were carried out to explore asymmetric $BaTiO_3/SrTiO_3/CaTiO_3$ superlattices,[122] with subsequent calculations reporting enhanced polarization that could be tuned by controlling the periodicity.[123] Experimental realization of $BaTiO_3/SrTiO_3/CaTiO_3$ superlattices observed a 50% enhancement in ferroelectric polarization despite 2/3 of the material being nominally non-ferroelectric.[121] By varying the relative thickness of the three layers in the repeat unit, researchers demonstrated that the enhanced polarization was driven by the built-in asymmetry of the trilayer repeat-unit and local distortions at the various interfaces. More recently, this asymmetric superlattice approach has been used in $BaTiO_3/SrTiO_3/LaTiO_3$ superlattices to couple the ferroelectric distortion from $BaTiO_3$ to the 2D electron gas that forms at the $SrTiO_3/LaTiO_3$ interface.[124] Optical second-harmonic generation measurements confirm the entire structure is non-centrosymmetric while the metallic nature of the $SrTiO_3/LaTiO_3$ interface is maintained, resulting in a so-called polar metal. The results from these ferroelectric-based superlattices have driven interest in utilizing such interface engineering to drive similar polar distortions in other metallic-oxide systems, including inducing broken inversion symmetry and novel spin textures in superlattices of $La_{0.6}Sr_{0.4}MnO_3/LaAlO_3/SrTiO_3$,[120] control of magnetic skyrmions in ultrathin $SrRuO_3$ films sandwiched by ferroelectric $BaTiO_3$,[125] and octahedral-tilt engineering of a polar metal state of single-layer $LaNiO_3$ films.[126] These studies serve as an example of the power of superlattice- and interface engineering to achieve a wide range of properties in ferroelectric oxides.

3.2.3. Topological-Polar Textures in $(PbTiO_3)_n/(SrTiO_3)_n$ Superlattices

Perhaps the most significant demonstration of the rich ferroelectric physics enabled through the synthesis of high-quality, complex-oxide heterostructures came with the discovery of emergent topological-polar textures in $(PbTiO_3)_n/(SrTiO_3)_n$ superlattices (where n is the number of unit cells). The concept of topology has attracted much attention in condensed-matter physics and materials science in recent years, and has been found to give rise to a number of exotic physical phenomena across a variety of materials systems.[127] In general, topology is concerned with the properties of geometric objects subjected to continuous deformation. In the context of condensed-matter physics, these features can exist as objects in reciprocal space, as in the band structures of topological insulators,[128] or as real-space objects, for example, in the spin textures of magnetic skyrmions. In magnetic systems, demagnetization fields

at interfaces drive domain formation and counteract exchange interactions and crystalline anisotropy, both of which favor long-range ordering of spins. While this commonly results in the formation of uniform domains, shifting the relative strength of these various energies can give rise to complex spin textures. Particularly in thin magnetic layers, occurrences of flux-closure,[129] vortex,[130] and skyrmion[131] domains are now well-documented. While often considered analogous to ferromagnetic materials, it was long believed that the strong dipole–lattice coupling and associated crystalline anisotropy in ferroelectrics would prevent formation of vortex- or skyrmion-like domain structures with continuously rotating polarization.

This understanding began to shift in the mid-2000s, when first-principles-based simulations of ferroelectric nanoparticles and nanodots, in part motivated by the same questions regarding size limitations to ferroelectric order discussed before (Section 2.2.2), resulted in polar structures with nonzero toroidal moments and unexpected vortex-like features.[132,133] Key to these studies, which examined prototypical $BaTiO_3$[132] and $PbZr_{1-x}Ti_xO_3$[133] systems, was the removal of the periodic or short-circuited boundary conditions that were standard in other simulations of finite-size effects, highlighting the importance of both reduced length scales and enhanced depolarization fields in driving formation of novel polarization configurations. These studies pushed researchers to reimagine the possibilities for ferroelectric topologies and motivated the experimental pursuit of such structures.

Leveraging understanding of size and strain effects in ferroelectric thin films, researchers began synthesizing superlattices with thin ferroelectric layers sandwiched between dielectric layers to confine the ferroelectric polarization, maximize depolarization fields, and force domain structures to compensate. In 2007, experiments on short-period $(PbTiO_3)_1/(SrTiO_3)_1$ superlattices found that such heterostructures demonstrated improper ferroelectricity arising from antiferrodistortive rotations of the oxygen octahedra induced at the $PbTiO_3/SrTiO_3$ interfaces.[134] Subsequent studies using much thicker (10–20 nm) $PbTiO_3$ layers between $SrTiO_3$ resulted in the formation of periodic arrays of flux-closure domains.[135,136] Finally, in 2016, advances in atomic-resolution scanning transmission electron microscopy (STEM) allowed for vector mapping of the polar displacements in $(PbTiO_3)_n/(SrTiO_3)_n$ (n = 10–20 unit cells) superlattices grown on $DyScO_3$(110) substrates, revealing periodic arrays of continuously rotating polarization in the $PbTiO_3$ layer (**Figure 5**a).[137] Cross-sectional dark-field TEM and subsequent X-ray scattering studies showed that these vortex arrays exhibited long-range, in-plane ordering with vortex periodicity of ≈10 nm (Figure 5b). Ultimately, it was found that the competition between the elastic energy of $PbTiO_3$ on $DyScO_3$, which typically favors c/a domains, the electrostatic energy due to the polar discontinuity at the $PbTiO_3/SrTiO_3$ interface, and the gradient energy associated with rotation provide the driving force for formation of these polar vortices.

The observation of polar vortices in $(PbTiO_3)_n/(SrTiO_3)_n$ superlattices only served as a starting point for a wealth of studies aimed at manipulating this newfound ferroelectric order. Careful tuning of the superlattice periodicity showed that shorter-period superlattices (n = 4–10 unit cells) exhibit traditional ferroelectric a_1/a_2 domains, but for longer-period superlattices (n = 12–18), X-ray diffraction studies showed the coexistence of ferroelectric a_1/a_2 domains and vortex arrays. PFM studies allow for visualization of the real-space distribution of these phases, revealing a mesoscale, fiber-textured, hierarchical superstructure of alternating stripes of a_1/a_2 domains and vortex arrays with ≈300 nm periodicity (Figure 5c,d).[138] This work further confirmed, through PFM and supporting phase-field studies, that the vortex tubes also exhibit a nonzero polarization component along the length of the tube, indicating that these swirling polar textures have an associated toroidal moment. This toroidal moment provided an approach to manipulate the vortex phase by means of an in-plane DC electric field, and subsequent electric-field-driven interconversion between the a_1/a_2 domains and vortex arrays was demonstrated. On the other hand, this discovery also opened the possibility for novel phenomena associated with this emergent toroidal-order parameter, as well as the possibility of emergent chiral order. A chiral object is one which cannot be superimposed onto its mirror image, and thus possesses a handedness, and can typically be detected via interaction with circularly polarized light. Soft X-ray resonant diffraction, whereby the X-ray absorption spectra are collected at specific diffraction conditions associated with the vortex periodicity, showed strong circular dichroism supporting the notion that the vortices are indeed chiral.[139] The properties of these vortex arrays are currently the subject of numerous studies leveraging this unique interaction with incident light. For example, it was found that optical stimulation of superlattices containing coexisting vortex and ferroelectric phases could induce a hidden supercrystal phase which exhibits long-range hierarchical ordering throughout the sample.[140] Studies utilizing terahertz stimulation have further demonstrated that these polar-vortex arrays exhibit emergent collective acoustic modes (dubbed a vortexon), which is associated with the staggered, off-centering of the individual vortices in the array.[141]

While significant effort is being dedicated to understanding the structure and implications of such polar vortices, other novel polar textures have already being discovered. While vortices are observed in $(PbTiO_3)_n/(SrTiO_3)_n$ superlattices under tensile strain on $DyScO_3$ substrates, when the same superlattices are synthesized under slight compressive strain on $SrTiO_3$ substrates, a different novel polar structure was observed. Plan-view STEM measurements revealed an array of long-range ordered circular features with ≈10 nm width and polarization diverging from the center.[142,143] Cross-sectional STEM showed arrays of cylindrical domains, which together, reveal a swirling polar texture resembling a 3D, hedgehog-like skyrmion. 4D STEM, which collects the full momentum distribution at every position, allows for reconstruction of the polarization in the center of the skyrmion feature and has shown that the true polarization structure is consistent with a Bloch-like skyrmion structure, indicating that the 3D polar skyrmion possesses features of two different types of skyrmion structures: hedgehog-type texture at the top and bottom and Bloch-type texture through the middle (Figure 5e,f). The combination of these two features also gives rise to emergent chirality, as demonstrated by X-ray resonant scattering circular dichroism experiments.[142] Simulations had predicted that local negative permittivity is found in a sheath surrounding the core of the polar vortex

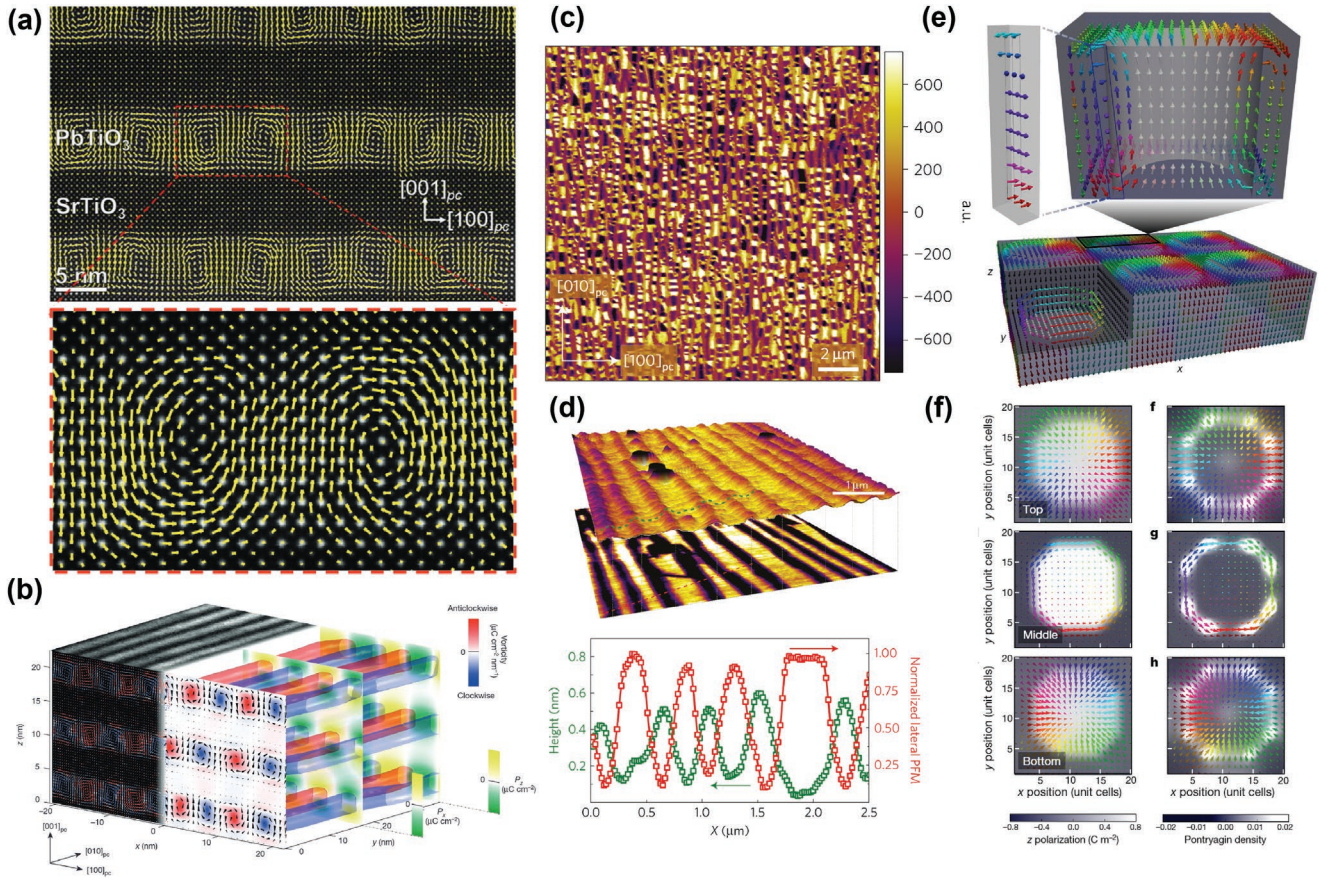

Figure 5. a) Top) Cross-sectional HR-STEM image with an overlay of the polar displacement vectors (PPD, indicated by yellow arrows) for a $(SrTiO_3)_{10}/(PbTiO_3)_{10}$ superlattice, showing that an array of vortex–antivortex pairs is present in each $PbTiO_3$ layer. Bottom) A magnified image of a single vortex–antivortex pair, showing the full density of data points (one for each atom) and the continuous rotation of the polarization state within such vortex–antivortex pairs. b) 3D phase-field simulation for a $(SrTiO_3)_{10}/(PbTiO_3)_{10}$ superlattice. The 3D geometry of the vortex–antivortex array from phase-field simulation of a $(SrTiO_3)_{10}/(PbTiO_3)_{10}$ superlattice is shown on the right. The front cross-section of the model shows the polarization vector P ordered into clockwise (blue) and anticlockwise (red) vortex–antivortex states which extend along the $[010]_{pc}$. For comparison, on the left is shown a cross-sectional HR-STEM image overlaid with a polar displacement vector map and a planar-view DF-TEM image projected onto the front and top planes of the axes, respectively. Red/blue color scales correspond to the curl of the polarization extracted from the phase-field model and the HR-STEM polar displacement map (PPD). The scale bars on P_x and P_z are from –44.81 to 44.81 μC cm^{-2} and from –54.24 to 54.24 μC cm^{-2}, respectively, whereas the vorticity is from –129.36 to 129.36 μC cm^{-2} nm^{-1}. a,b) Reproduced under the terms of the CC-BY Creative Commons Attribution 4.0 International license (https://creativecommons.org/licenses/by/4.0).[454] Copyright 2018, The Authors, published by AIP Publishing. c) Lateral piezoresponse image for $(PbTiO_3)_n/(SrTiO_3)_n$ superlattices (n = 16) synthesized on $SrRuO_3$-buffered $DyScO_3$(110) substrates revealing stripe-like order in which alternating stripes exhibit high (checkered white and black) and low or zero (brown) piezoresponse with a periodicity of ≈300 nm along the $[010]_{pc}$. d) Top) Changes in the lateral piezoresponse amplitude confirm that the vortex phase corresponds to protruding features in surface topography with low piezoresponse, while the a_1/a_2 phase is recessed in topography with large lateral piezoresponse. Bottom) A line trace across the topography (green-dashed line) and lateral piezoresponse images (red-dashed line) revealing opposite and dramatic modulations in surface topography and lateral piezoresponse between the a_1/a_2 and the vortex phases. c,d) Reproduced with permission.[138] Copyright 2017, Springer Nature. e) Top right) A cross-section of the polarization texture predicted by second-principle calculations for $PbTiO_3$–$SrTiO_3$ superlattices grown on $SrTiO_3$(001) substrates. Top left) Bloch walls appear along both the out-of-plane and in-plane directions. Bottom) Repetition of the skyrmion structure in the x- and y-directions, similar to the one observed experimentally. The polarization diverges at the top of the structure, rotating smoothly from $+z$ to $-z$ polarization. At the domain wall of the structure, the polarization component rotates in plane, resembling a Bloch skyrmion. f) Hedgehog-like skyrmion at the top interface between $SrTiO_3$ and $PbTiO_3$. Bloch skyrmion at the central plane in $PbTiO_3$. Hedgehog-like skyrmion at the bottom interface. The up and down domains are represented by white and gray regions, respectively. The arrows represent the normalized electric dipole moments in the x–y-plane. e,f) Reproduced with permission.[142] Copyright 2019, The Authors, published by Springer Nature.

or skyrmions.[144] The suppressed polarization and enhanced energy density at the skyrmion sheath makes the second derivative of free energy be negative, resulting in local negative permittivity. Experimental realization of this local negative permittivity was confirmed in these polar-skyrmion structures at the skyrmion boundary, suggesting that such polar topologies can have novel electrical responses.[143]

Understanding of the formation and topology of these dipolar textures has been enabled by advances in mesoscale phase-field and second-principle simulations.[138,142,145–147] Phase-field simulations have been particularly useful for both predicting and understanding the complex mesoscale structures formed in these superlattices. For example, understanding the nature of phase transitions and domain-wall boundaries in samples

with coexisting vortex and a_1/a_2 domains was made possible by correlating phase-field and PFM studies.[138,147] In general, the direct mapping of the various elastic and electric energy scales in phase-field simulations provide researchers critical insight into understanding how to engineer oxide interfaces to enable new ferroelectric phases and textures. The study of the topology of these dipolar textures has also necessitated novel simulation techniques, and approaches like second-principle calculations have been critical to probing the explicit topological structures and protection that may be observed in these superlattices. These approaches, which extend more typical first-principle DFT-based methods to more out-of-equilibrium structures,[148] have provided real-space 3D descriptions of the polar texture, which can be verified with STEM polar-vector mapping. Such a real-space description allows for determination of the integer invariant skyrmion number of $N_{sk} = +1$ for each layer of the 3D bubble, indicating that the texture is indeed topological, and supporting the determination of the chirality of the system. While these second-principle approaches are relatively new, they will continue to be critical components of studying topological polar textures in ferroelectric systems.

3.3. Elastic and Chemical Gradients

Equipped with the understanding of homogeneous elastic and chemical modification of oxides, and armed with advanced capabilities in oxide thin-film synthesis, researchers can now envision utilizing nonuniform manipulation of the ferroelectric lattice to induce novel behavior. The introduction of strain gradients gives rise to another mechanism for manipulating polarization, called flexoelectricity. At the same time, inducing chemical gradients in films provides a means to creating phase competition and enabling new properties in otherwise traditional ferroelectric systems.

3.3.1. Flexoelectricity

Coupling of inhomogeneous mechanical deformation of a material to the dielectric polarization gives rise to a property called flexoelectricity.[149] The strain gradient associated with this deformation can break inversion symmetry and induce polarization even in non-piezoelectric materials (**Figure 6**a). Mathematically, flexoelectric polarization is given by $P_l = \mu_{ijkl}\frac{\partial u_{ij}}{\partial_k}$, where P_l is the polarization, μ_{ijkl} is the flexoelectric coefficient tensor, and $\frac{\partial u_{ij}}{\partial_k}$ is the strain gradient. Empirically, the magnitude of μ_{ijkl} is known to be proportional to the dielectric susceptibility and inversely proportional to the lattice constant. Most dielectric (oxide) materials are quite brittle under mechanical bending, making it hard to achieve large strain gradients in bulk materials and thus flexoelectric effects are typically negligible in the bulk. On the other hand, the ability of thin films to withstand much larger strain gradients means the energy scale of flexoelectricity can become comparable with that of the dipolar interaction. Flexoelectric effects thus provide another avenue for manipulation of polar order in thin films.[150]

Many pathways have been used to generate strain gradients in thin films. One of the more common methods is via application of a mechanical force from a scanning-probe tip to induce a local strain gradient (Figure 6b).[151–155] The deformation from the pressure of the tip in contact with a film surface, which is dependent on the mechanical stiffness of the material, tip radius, and the force input has been shown to generate strain gradients greater than 10^7 m^{-1} in ultrathin $SrTiO_3$ films, nearly eight orders of magnitude greater than those generated in $SrTiO_3$ single crystals.[153,156] Such large strain gradients are capable of inducing polarizations on the order of 20 μC cm^{-2}. Tip-induced flexoelectric effects thus provide a novel method for manipulation of ferroelectric domains. For example, in-plane switching of $BiFeO_3$ thin films was demonstrated using a trailing flexoelectric field (i.e., dragging the tip while it pushes on the surface) whereby the scan direction of the probe tip provides in-plane control of domain switching.[152] Similar methods have even been used to stimulate controlled movement of oxygen vacancies in $SrTiO_3$.[153] Furthermore, tip-induced flexoelectricity can tune the barrier potential of dielectric materials by electronic band bending, resulting in enhanced conduction in insulating materials.[154,155]

Flexoelectric effects also play a role in local polarization in determining the ferroelectric domain structure. For example, the misfit angle along ferroelastic c/a domain boundaries in clamped $PbTiO_3$ films produces a local strain gradient.[157] As a result, the flexoelectric field from these 90° domain walls locally rotates the polarization direction. Similar effects are observed in tetragonal-like $BiFeO_3$ films grown on $LaAlO_3$ substrates[66,158] where large strain gradients between the tetragonal-like and rhombohedral phases have been shown to contribute to the large piezoresponse in these systems.[158] Strain gradients can also be induced by the relaxation of epitaxial strain.[159–161] The misfit strain from the substrate is generally relaxed above some critical thickness, at which point large strain gradients (up to ≈10^6 m^{-1}) can form. During film growth, this strain gradient provides a flexoelectric field, which acts as a built-in internal field.[159] Whereas the ferroelectric polarization is often small at high growth temperatures, flexoelectric fields from strain relaxation remain and can play an important role in determining the domain configuration of the as-grown ferroelectric films. As a consequence, the built-in flexoelectric field has been used to manipulate ferroelectric switching properties, for example, alignment of defect dipoles resulting in biased hysteresis loops.[160,161]

3.3.2. Compositionally Graded Films

Advanced synthesis techniques also provide a route toward generating controlled compositional gradients, wherein the composition of a thin film smoothly changes as a function of thickness.[162–164] In these films, rather than combining dissimilar structures with sharp interfaces, as in the superlattices discussed before (Section 3.2.3), smoothly varying the composition, such that the composition at the interface with the substrate is distinct from the composition at the film surface, can lead to geometric frustration and give rise to novel domain structures and polarization response.[165] Early studies of films

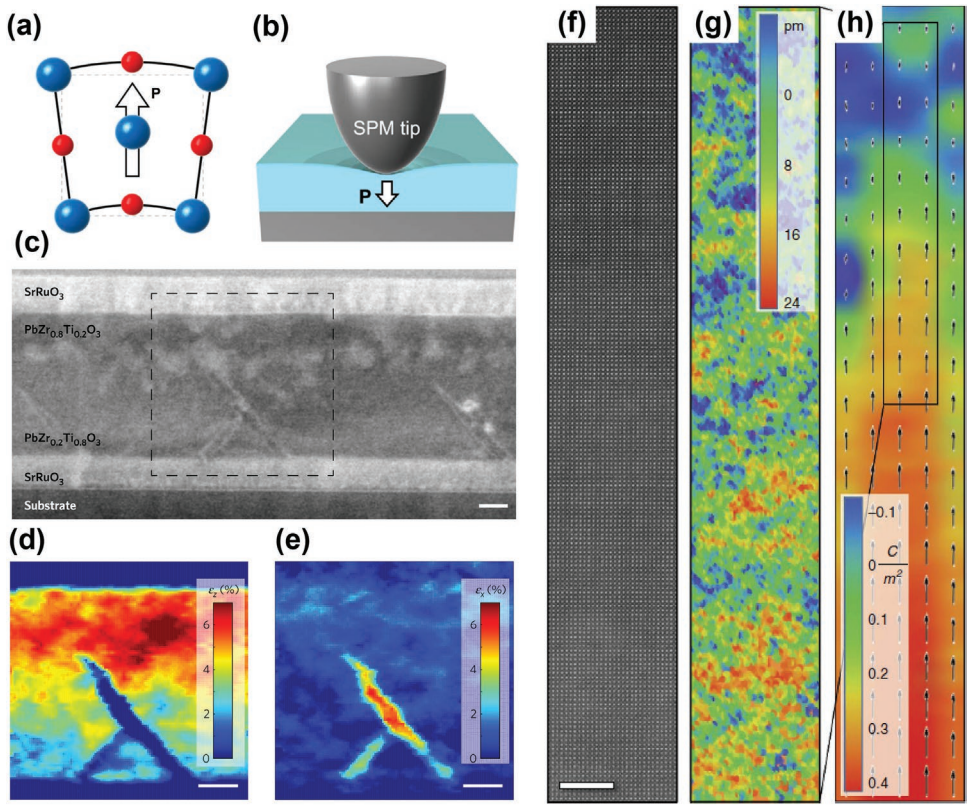

Figure 6. a) General mechanism of flexoelectricity. b) Local probe-induced deformation during scanning probe microscopy (SPM). a,b) Reproduced under the terms of the CC-BY Creative Commons Attribution 4.0 International license (https://creativecommons.org/licenses/by/4.0).[150] Copyright 2020, The Authors, published by AIP Publishing. c) High-angle angular dark-field scanning transmission electron microscopy (HAADF-STEM) image of compositionally graded $PbZr_{0.8}Ti_{0.2}O_3 \leftrightarrow PbZr_{0.2}Ti_{0.8}O_3$ heterostructure grown on $SrRuO_3/GdScO_3(110)$ revealing the presence of needle-like ferroelastic domains. d,e) Nanobeam diffraction-based strain mapping of compositionally graded $PbZr_{0.8}Ti_{0.2}O_3 \leftrightarrow PbZr_{0.2}Ti_{0.8}O_3$ heterostructures reveals the out-of-plane (d) and in-plane strain around the ferroelastic domain (e). Scale bars are 25 nm. c–e) Reproduced with permission.[164] Copyright 2016, Springer Nature. f) Cross-section HAADF–STEM image of the top 72 nm of a compositionally graded (that transitions linearly from $BaTiO_3$ to $Ba_{0.6}Sr_{0.4}TiO_3$ from $SrRuO_3$-buffered/$GdScO_3(110)$ substrate to surface) heterostructure. Scale bar: 5 nm. g) 2D map of local displacement of the Ti ion showing a smooth gradient in the displacement (and therefore polarization) as a function of position. h) Molecular dynamics simulation of the compositionally graded heterostructure showing a large gradient in the polarization throughout the thickness of the heterostructure. f–h) Reproduced under the terms of the CC-BY Creative Commons Attribution 4.0 International license (https://creativecommons.org/licenses/by/4.0).[163] Copyright 2017, The Authors, published by Springer Nature.

graded from $PbZr_{0.75}Ti_{0.25}O_3$ to $PbZr_{0.55}Ti_{0.45}O_3$, for example, showed large polarization offsets due to a built-in field associated with different polarizations in the end-member compositions.[166] More recent studies, on the other hand, have explored compositional gradients between end members with different symmetries. For example, researchers have successfully synthesized coherently strained, compositionally graded heterostructures that change from $PbZr_{0.2}Ti_{0.8}O_3$ (tetragonal) at the substrate interface to $PbZr_{0.8}Ti_{0.2}O_3$ (rhombohedral) at the film surface, amounting to a strain gradient of $\approx 4 \times 10^5$ m^{-1}. In these films, a large offset of ferroelectric hysteresis was observed accompanied by unexpected domain structures.[162] The built-in electric field and competition between tetragonal and rhombohedral lattice symmetry associated with a gradual increase of strain was shown to induce large remnant polarization and low permittivity in this system, while cross-sectional TEM studies revealed the presence of needle-like domain walls terminated halfway through the thickness of the films (Figure 6c–e).[164] Subsequent scanning-probe-based BEPS studies of such films revealed locally enhanced piezoresponse near these needle-like domains. In contrast to homogeneous heterostructures, where volume fractions of *a* domains are typically limited by elastic constraints, the needle-like domains in these compositionally graded heterostructures can expand toward the surface of the film, and the associated ferroelastic $c \rightarrow a$ interconversion provides large local changes in out-of-plane lattice parameter, leading to large piezoresponses. In addition to smoothly varying the film composition between end members with different ferroelectric symmetries, novel polar responses can also be generated by varying the composition between isosymmetric ferroelectrics that possess distinct temperature-dependent responses. Synthesizing compositionally graded heterostructures that varied from $BaTiO_3$ at the substrate interface to $Ba_{0.6}Sr_{0.4}TiO_3$ at the film resulted in films that were coherently strained to the substrate and tetragonal, but with a continuously changing out-of-plane *c* lattice parameter. Cross-sectional STEM and nanobeam diffraction measurements were used to examine the in-plane and out-of-plane strains, revealing large

strain and polarization gradients across the thickness of the film (Figure 6f–h).[163] While in single-layer, homogeneous films of the end members, the T_C shifts by more than 500 °C between $BaTiO_3$ and $Ba_{0.6}Sr_{0.4}TiO_3$, in the compositionally graded films, one obtains a large, temperature-stable permittivity along with a large tunability at all temperatures.

While recent work has focused on vertical compositional gradients, lateral compositional gradients have also been studied for a number of applications. Traditionally, lateral compositional variation in thin films has been used for high-throughput, combinatorial mapping of phase diagrams in search of ferroelectric materials. Synthesis of lateral compositional gradients requires purpose-built deposition systems, typically involving motorized masks to continuously expose or shield the substrate during deposition as the deposition source is changed to create smooth gradients. Similarly, novel approaches for high-throughput measurement of films with high resolution has allowed researchers to search for optimal compositions for a number of functionalities,[167–170] including high dielectric tunability,[171] piezoelectric response (MPB),[172,173] electro-optic properties.[174] Through this, fabrication and study of entire phase diagrams for binary and ternary material systems either as a continuous composition spread or as spatially addressable library in a single thin film is possible. As an example, a past study involved identifying specific material compositions with a high dielectric constant and low leakage current density in $Ba_{1-x}Sr_xTiO_3$ and $(Ba_{1-x-y}Sr_xCa_y)TiO_3$ systems as a function of doping.[175,176] Combining lateral compositional control with RHEED-enabled atomic precision allowed for synthesis of artificial $SrTiO_3/BaTiO_3$ superlattices where the composition is controlled in both vertical and lateral directions.[177] Yet, the complexity involved in deposition has limited the extent to which these techniques have been applied to understand the properties induced by the gradients themselves. Armed with new understanding of vertical compositional gradients, and the novel ferroelectric properties they enable, lateral compositional gradients may soon be revisited as a means to engineer ferroelectric properties and potentially enable novel dipolar textures. In sum, compositional gradients provide a powerful method for inducing strain gradients, polarization gradients, and phase competition that enable one to engineer ferroelectric/dielectric properties and exotic domain structures.

3.4. Defect Engineering

Defective interfaces in ferroelectric structures were one of the earliest concerns of researchers studying ferroelectric thin films, and efforts have been predominantly focused on the removal of defects and creation of more pristine ferroelectric films. In some cases, however, defects have been found to induce unexpected (and even improved) properties in ferroelectrics—observations that are now changing how the community considers and approaches the synthesis of these materials. For example, it has been proposed that defect accumulation at domain walls is at least partially responsible for the onset of domain-wall conduction in materials like $BaTiO_3$[178] and $PbTiO_3$.[179] Such findings have driven application of a range of tools to attempt to characterize defects in ferroelectric films. Aberration-corrected STEM coupled with electron-energy loss spectroscopy (EELS), for example, has been used to map local oxidation states of the charged defects at domain walls in $BiFeO_3$[101] and $PbZr_{0.1}Ti_{0.9}O_3$[180] thin films. The presence of both Fe^{4+} and Fe^{3+} at domain walls in $BiFeO_3$ establishes a p-type hopping-based mechanism for domain-wall conduction.[101] Similarly, in $PbZr_{0.1}Ti_{0.9}O_3$, EELS was instrumental in determining the presence of Ti^{3+} at the charged domain walls indicating n-type conduction by free electrons generated due to charge compensation.[180] At a more macroscopic scale, capacitor-based deep-level transient spectroscopy, a technique traditionally used in the study of semiconductor materials,[181] has been used for measurement of the defect states and provides critical insight for understanding the nature of defect creation and the effect on ferroelectric properties.[182–184]

Ferroelectric oxides, in particular, can accommodate high defect concentrations and large deviations from stoichiometry before formation of secondary phases, and the nonequilibrium nature of many thin-film deposition techniques provides an approach to both manipulate defect concentrations and achieve nonequilibrium concentrations of different defect species.[185] The high-energy adatoms (sometimes in excess of 10–100 eV) generated in PLD, for example, can produce intrinsic point defects and defect clusters to be introduced in perovskite oxides via both stoichiometry variation in the plume and knock-on-damage from the depositing species. Through control of the wide parameter space of PLD, in situ creation of intrinsic defects has been studied in common ferroelectrics such as $BaTiO_3$,[183] $BiFeO_3$,[186] and $PbTiO_3$.[184] Such defects result in changes to the lattice (often expansion of the lattice parameters) and, in turn, marked variation of both transport (**Figure 7**a) and ferroelectric properties. In $BaTiO_3$ films, slight cation nonstoichiometry (something that readily can occur in the deposition of such materials at high temperatures) can result in the formation of defect dipoles that increase the tetragonality and T_C of the material dramatically. These defect dipoles, which also couple to the strain applied from the substrate and the polarization of the material, ultimately lead a preference for the alignment of the polarization in a single direction, causing increased ferroelectric imprint with higher defect concentration (Figure 7b).[183] In $PbTiO_3$ films deposited via PLD, the use of low oxygen pressures during growth resulted in significant knock-on damage resulting in films with relatively poor crystallinity, but saturated and closed hysteresis loops with minimal leakage current density (Figure 7c); properties much more desired to what was observed in "pristine" films grown at higher pressures with nearly ideal crystallinity which exhibited high leakage current density. In yet other systems, such as $BiFeO_3$, it was shown that growth-induced nonstoichiometry can also manipulate ferroelectric order. By varying the deposition conditions, it is possible to produce single-phase $BiFeO_3$ films with varying Bi:Fe ratios and, in turn, achieve a large variety of the as-grown domain structures (from long-range, well-defined two-variant stripe domains with relatively low bismuth content to small, disordered four-variant domain structures with high bismuth content).[186] In antiferroelectric $PbZrO_3$, growth-induced lead excess ($Pb_{1.2}ZrO_3$) was found to destroy the antiferroelectric order as the excess lead was accommodated as antisite

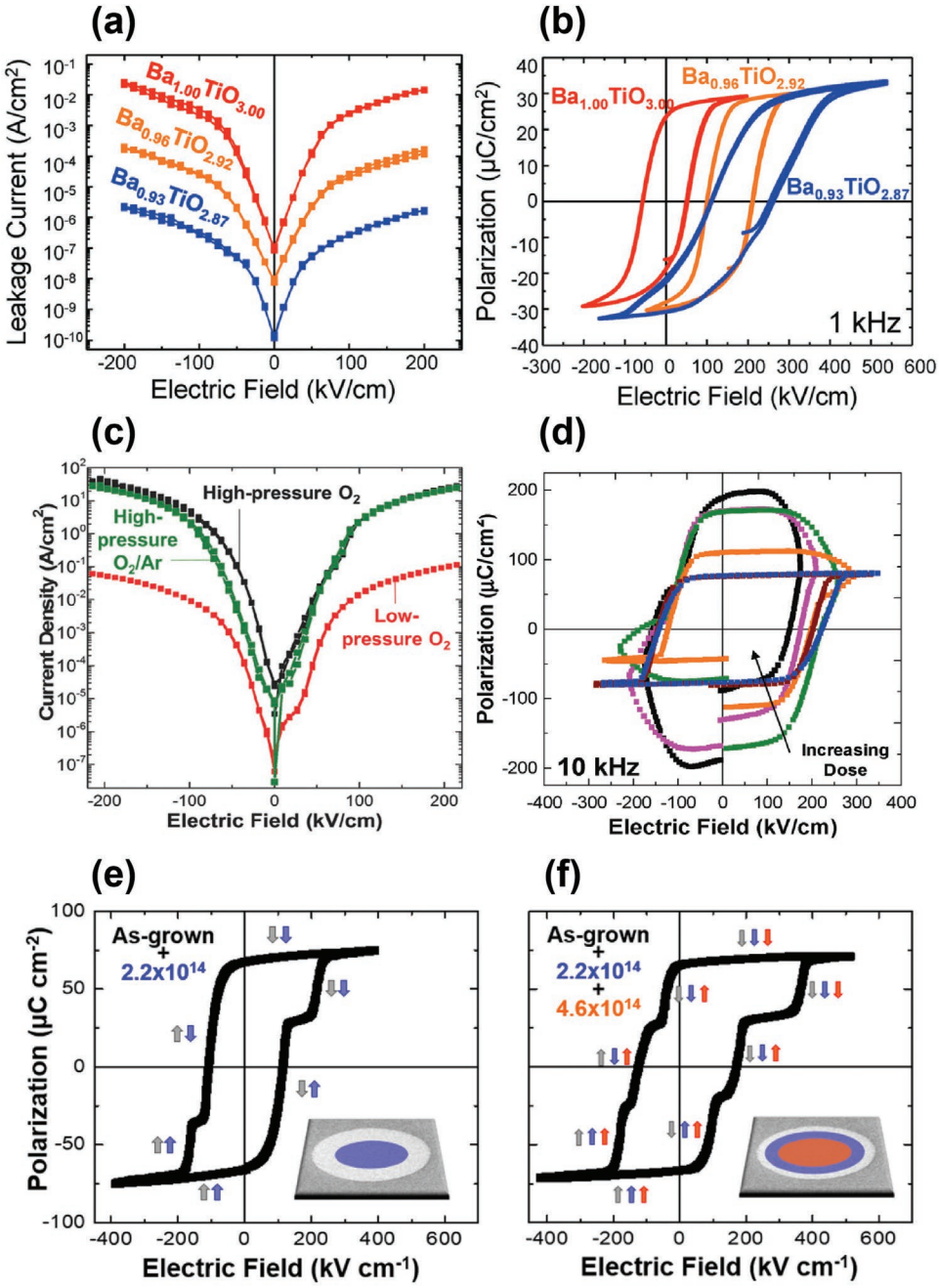

Figure 7. a) Room-temperature leakage current measurements for $Ba_{1.00}TiO_{3.00}$, $Ba_{0.96}TiO_{2.92}$, and $Ba_{0.93}TiO_{2.87}$, b) polarization–electric field hysteresis loops measured at 1 kHz for the same heterostructures. a,b) Reproduced with permission.[183] Copyright 2018, The Royal Society of Chemistry. c) Leakage current density as a function of DC electric field for $PbTiO_3/SrRuO_3$ thin-film heterostructures were grown at high-pressure O_2, high-pressure O_2/Ar, and low-pressure O_2. d) Ferroelectric polarization–electric field hysteresis loops measured at 10 kHz for the same high-pressure O_2 heterostructures after various He^{2+} bombardment doses. c,d) Reproduced with permission.[184] Copyright 2016, Wiley-VCH. Polarization–electric field hysteresis loops for capacitors consisting of $PbZr_{0.2}Ti_{0.8}O_3/SrRuO_3$ heterostructures sequentially bombarded with e) 2.2×10^{14} ions cm^{-2} (blue region), resulting in two-step switching and f) 4.6×10^{14} ions cm^{-2} (red region) resulting in asymmetric three-step switching. e,f) Reproduced with permission.[195] Copyright 2018, American Physical Society.

defects (Pb_{Zr}) that give rise to ferroelectric behavior, rather than the typical antiferroelectricity in $PbZrO_3$.[187]

Apart from nonstoichiometry, substitutional defects can play a major role in manipulating (anti)ferroelectric behavior. A well-studied example is HfO_2 which does not exhibit ferroelectricity in any polymorphic forms due to the presence of an inversion center. Introducing substitutional species (e.g., silicon, aluminum, zirconium, yttrium, strontium, lanthanum, gadolinium, etc.), however, can stabilize a ferroelectric orthorhombic phase via intermediate non-centrosymmetric tetragonal and

monoclinic phases. First-principle DFT calculations have played an important role in identifying pathways toward switchable ferroelectric polarization in such hafnia-based materials.[188–191] Likewise, chemical substitution has been used to improve the properties of many other ferroelectrics—including a long history of improving leakage currents in films. For example, in $BiFeO_3$, which possesses one of the largest spontaneous polarizations (≈95 μC cm^{-2}) of any commonly studied ferroelectric, *A*-site substitution has been found to destabilize polar order, reorient the polarization direction, and reduce the free-energy barrier for ferroelectric switching.[192] In particular, the rotation of the polar axis via lanthanum substitution has been found to reduce the magnitude of the coercive voltage, enabling lower-power switching.[192] Such substitutional studies have also highlighted the connection between polar order, orbital order, and band structure in ferroelectrics. For example, lanthanum (and other rare-earth) substitution has been reported to drive a transition from a direct to an indirect bandgap in $BiFeO_3$ leading to longer carrier lifetimes and higher efficiencies for ferroelectric photovoltaic applications.[193]

Building from a growing appreciation of how the synthesis process can impact defect types and concentrations in ferroelectrics and a how such defects can impact the properties of these materials, researchers are now transitioning to what can effectively be thought of defect engineering approaches to elicit the desired properties through ex situ creation of defects in otherwise high-quality films. Recent years have seen researchers leverage ion beams in a deterministic way to produce the desired properties. For example, by bombarding the ferroelectric heterostructures with relatively high energy (1–6 MeV) He^{2+} ions using pelletron accelerators, bombardment doses in the range 10^{14}–10^{16} cm^{-2} can readily be produced in ferroelectric films. The result is controlled defect densities and profiles that leverage the mature field of ion-induced damage in materials. Ion bombardment of $BiFeO_3$ and $PbTiO_3$ (Figure 7d) films, deposited by either PLD[182,184] or MBE[194] has been found to create defect complexes and clusters which can reduce the free-carrier transport via the formation of deep trap states in the bandgap. What this means is that it is now possible to "fix" deficient properties in a material after the fact (i.e., after it is grown). This could be a key enabling processing approach as we push to integrate such materials into increasing complex device structures that might limit growth to nonideal conditions. In addition to reducing leakage current, which is (of course) favorable for many applications, such defects can also serve as pinning sites for domain walls,[182,194,195] and can lead to an increase in the coercive field which is typically less desirable for applications relying on traditional bipolar switching of a ferroelectric. As understanding of how these ion beams can control ferroelectric properties grew, researchers have now been able to utilize these features which were once considered only deleterious to ferroelectric properties to produce novel functionality. For example, utilizing a helium-ion microscope with a focused-He^{2+} beam with nanometer-scale spatial resolution, deterministic nanoscale defect profiles could be created, resulting in spatially varying coercive field in a single device.[195] Switching studies demonstrated that a single capacitor could exhibit multistate polarization switching (Figure 7e,f). This field of defect engineering thus serves as a new facet for engineering ferroelectric functionalities in next-generation electronic devices.

3.5. Hybrid Epitaxy—Integrating Ferroelectric Oxides with Semiconductors and Beyond

With an eye to exploiting ferroelectric functionalities in nonvolatile memories, logic devices, sensors, and beyond,[196] there has been increasing attention to the exploration of how one can integrate these complex-oxide materials onto nonoxide semiconductor substrates (e.g., silicon, germanium, III–V compounds, etc.) to be compatible with the existing complementary metal–oxide–semiconductor (CMOS) platforms used in the electronics industry. Epitaxial integration, however, is challenging and is still limited by the large lattice mismatch and difference in thermal expansion coefficients between ferroelectric oxides and semiconductor substrates,[197] reactions between some oxides and some substrates,[198,199] as well as the highly defective interface between the oxide layer and the silicon caused by the formation of an amorphous SiO_2 layer during the deposition.[196,198] This SiO_2 layer can be detrimental to the applications requiring strong electrical coupling between the polarization in ferroelectric oxide and the semiconductor channel as in, for example, the metal–oxide–semiconductor (MOS) structure in a ferroelectric field-effect transistor (FeFET).

Although different deposition methods, including sputtering, chemical vapor deposition, PLD, and ALD have been used to grow oxide materials on semiconductors,[200–202] most of the work in the past two decades has been focused on MBE.[203–206] With MBE, (extensive) oxidation of the silicon surface can be avoided by carefully adjusting the growth parameters during the deposition, suppressing the formation of thick SiO_2 layers and producing a relatively abrupt interface between the ferroelectric and underlying substrate.[198,203,207] A few perovskite oxides have been integrated onto Si (001) substrates with RHEED-assisted MBE such as $SrHfO_3$ and $BaTiO_3$.[204,208,209] Unlike Si (001), Ge (001) has a smaller lattice mismatch and thermal expansion coefficient difference with $BaTiO_3$ and does not oxidize as easily as silicon, which makes it somewhat easier to achieve direct integration (i.e., without a buffer layer) of $BaTiO_3$ films with high crystallinity.[210]

The most successful integration of oxides onto silicon, however, has been the monolithic growth of $SrTiO_3$ onto Si (001) substrates, which was first realized in 1998.[207,211–213] The large lattice mismatch between the diamond-cubic structure of silicon (a = 5.43 Å) and the perovskite $SrTiO_3$ (a = 3.905 Å) requires that $SrTiO_3$ coherently strains along the face-diagonal direction of the silicon resulting in an in-plane orientation of $SrTiO_3$[100]//Si [110] to maintain an out-of-plane orientation of $SrTiO_3$(001)//Si (001).[196] To avoid interfacial reaction problems between oxygen, titanium, and silicon, a strontium sub-monolayer is typically deposited onto the cleaned Si (001) surface[214] (obtained by thermally removing the native SiO_2 layer in situ prior to deposition). Alternatively, because strontium can also act as a catalyst for the thermal desorption of the native SiO_2 layer at a lower temperature,[215] the strontium can be deposited onto the uncleaned Si (001) surface to completely desorb the SiO_2. Ultimately, one-half monolayer of strontium

is formed to passivate the silicon surface, and subsequent oxidation forms a SrO monolayer that serves as the perovskite template.[216,217] The next few layers, namely, TiO_2 and SrO, have to be grown at relatively low temperature to suppress the oxidation of the underlying silicon surface and thus the growth must be followed by an annealing process to enhance the crystallinity of the $SrTiO_3$.[218] Using $SrTiO_3$ as a perovskite template on silicon substrates, many ferroelectric oxides have been produced with high crystallinity, including ferroelectric $BaTiO_3$,[204,219,220] multiferroic $BiFeO_3$, and relaxor $(1-x)PbMg_{1/3}Nb_{2/3}O_3$–$(x)PbTiO_3$.[221] For example, for $BaTiO_3$ films deposited on $SrTiO_3$/Si, cross-sectional TEM (**Figure 8**a) reveals the production of high-quality interfaces and epitaxial growth between the $BaTiO_3$ and $SrTiO_3$ layers, and PFM (Figure 8b) reveals stable polarization switching. Moreover, the $SrTiO_3$/Si (001) pseudosubstrate is manufacturable with industry-scale MBE,[222,223] thus providing a promising route to wide-scale adoption of novel nonvolatile memories, logics, and other devices. Utilizing similar methods, studies have also demonstrated successful deposition of ferroelectric films on $SrTiO_3$-buffered or MgO-buffered GaAs substrates, greatly expanding the applications of such ferroelectric oxides into the optoelectronic regime.[224–226]

In parallel, there has been increasing interest in using epitaxial ferroelectrics as a substrate for devices based on 2D materials. One particular point of focus is electrical control of the electronic properties of 2D materials such as graphene and the 2D transition metal dichalcogenides in FET geometries. Fabrication of such devices can be tricky, as interface states can screen ferroelectric polarization. Studies utilizing graphene/ferroelectric heterostructures, for example, report gating or hysteretic switching dominated by trapping/detrapping of interface and defect trap states.[227,228] With particular attention paid to maintaining a pristine interface, researchers have transferred graphene to epitaxial $PbZr_{0.2}Ti_{0.8}O_3$ films with $SrRuO_3$ bottom electrodes, providing a means to reliably switch the ferroelectric polarization.[229] In turn, the ferroelectric polarization at the interface with graphene was shown to directly modulate charge carrier type and densities (Figure 8c). Environmental adsorbates, however, were still found to influence the nature of ferroelectric–graphene coupling, and alternative approaches, using fast voltage sweeps or device operation in vacuum, were

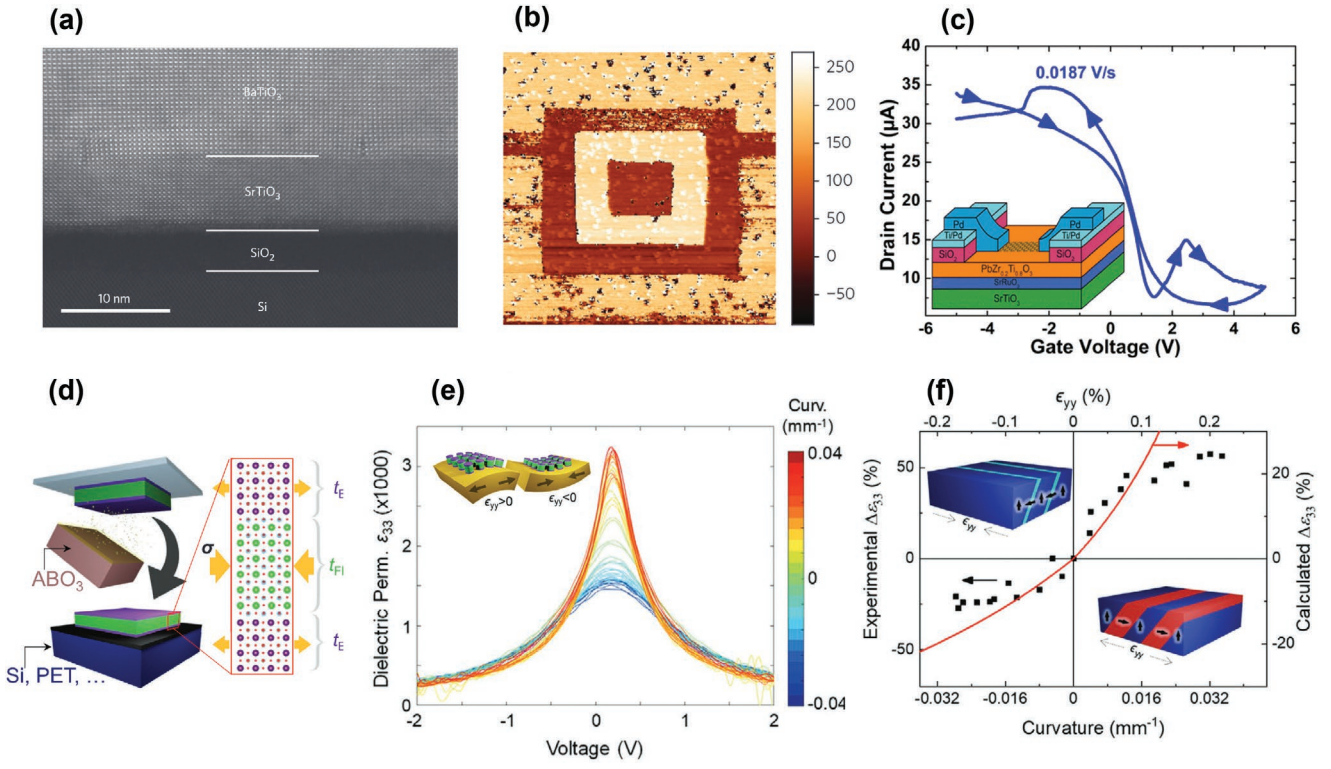

Figure 8. a) TEM image emphasizing the interface between $SrTiO_3$ and $BaTiO_3$ in $BaTiO_3$/$SrTiO_3$/amorphous interfacial layer (silicate and SiO_2) stack grown on Si substrate. b) Piezoresponse force microscopy phase contrast for a 16 nm thick $BaTiO_3$ film in the stack for (a) poled with +5, −5, and +5 V over 3, 2, and 1 μm regions, respectively. The images were collected over 4.5 × 4.5 μm^2 areas. a,b) Reproduced with permission.[204] Copyright 2013, Springer Nature. c) Complex I_D–V_G characteristic for large gate voltages with a drain voltage of 50 mV and a gate voltage sweep rate of 0.0187 V s^{-1} for a graphene transistor on $PbZr_{0.2}Ti_{0.8}O_3$ (inset). Reproduced with permission.[229] Copyright 2013, American Chemical Society. d) Fabrication of $BaTiO_3$ membranes via sacrificial layer etching and subsequent transfer via polymer stamp onto an arbitrary substrate. After releasing the films from the substrate, the elastic balance between the electrode (E) and ferroelectric (FE) layers creates an internal stress σ. e) Voltage dependence of dielectric permittivity measured at 10 kHz under different substrate curvatures. f) Measured (left axis) and calculated (right axis) bending-induced dielectric tunability as a function of substrate curvature (bottom) and estimated bending strain (top). Experimental data are obtained from the peak dielectric permittivity in (e); the red line shows the strain dependence obtained from a phenomenological polydomain model; schematic drawings show the expected domain configurations from the model, for the largest strain values reached in the experiment. d–f) Reproduced with permission.[235] Copyright 2020, Wiley-VCH.

used to avoid such extrinsic effects. Similar coupling has since been demonstrated in $MoS_2/PbZr_{0.2}Ti_{0.8}O_3$ devices, where hysteretic control of the MoS_2 conductivity was demonstrated in films with "pristine" interfaces, but could be easily disrupted by imperfections at the ferroelectric surface.[230] Hybrid epitaxy between oxide ferroelectrics and nonoxide systems thus represents a new avenue for integration ferroelectrics and enabling new function.

3.6. Freestanding Thin Films

The rich physics and novel functionalities observed in ferroelectric thin films discussed to this point has been enabled by high-quality oxide substrates; however, these same substrates quite literally impose significant mechanical constraints on what is possible. While there are many more substrates (and thus strain states) available to researchers today, they still do not provide continuous control of materials. Taking inspiration from the field of exfoliated 2D van der Waals materials,[231,232] researchers have begun to release freestanding membranes of ferroelectric perovskites and transfer them to a variety of substrates. Such studies are demonstrating a new paradigm for control of ferroelectric order. Here, we briefly review recent progress in freestanding ferroelectric membranes.

Releasing ferroelectric thin films provides a pathway to achieve all the synthetic control afforded by epitaxy in a single crystalline specimen free of the mechanical constraints imposed by the relatively large, stiff oxide substrate required for high-quality epitaxial growth. Early results utilized well-known chemical etching of the surface of $SrTiO_3(001)$ substrates to etch the surface SrO layer between the $SrTiO_3$ substrate and a 50 nm $SrRuO_3$ film deposited on top.[233] Following release, these films were transferred to silicon or sapphire substrates which could then be used as a template to grow high-quality $PbZr_{0.2}Ti_{0.8}O_3$ films, thus providing a pathway for deposition of perovskite ferroelectrics on an arbitrary substrate. The particularly harsh chemical treatment used in this work, however, limited the materials and substrates that could be used. To expand the range of materials, a number of epitaxial sacrificial layers have been employed, including water-soluble $Sr_3Al_2O_6$[234] and acid-etchable $La_{1-x}Sr_xMnO_3$ layers.[235] In these cases, high-quality heterostructures may be synthesized with thin (5–20 nm) sacrificial layers underneath, without much deviation from standard thin-film synthesis routes. More exotic methods have also been developed, including remote epitaxy, wherein a layered van der Waals material, often graphene, is deposited on an oxide substrate.[236,237] The atomic potential of the substrate penetrates the graphene, allowing the growing oxide layer to "feel" the surface of the oxide substrate remotely, without chemically bonding to the substrate. After deposition, the oxide layer can be exfoliated from the substrate via typical techniques. Various polymer support layers have been demonstrated as effective methods for transferring oxide membranes to a variety of substrates.[238,239]

Such freestanding oxide membranes provide a means to mechanically manipulate the oxide lattice like never before, illustrating possibilities for new ferroelectric control, as well as dramatic changes to the material's elastic properties. In ultrathin 3 nm thick $BiFeO_3$ films, enhanced tetragonality was observed in films after release from the substrate.[240] Freestanding membranes have also been demonstrated to have uncharacteristically large elasticity.[241] For example, a strain-induced phase transformation between rhombohedral and tetragonal-like structures (Section 2.4.3) in $BiFeO_3$ nanoribbons was shown to enable highly elastic 180° bending, equivalent to lattice strains greater than 5%.[242] The elastic moduli of $SrTiO_3$ membranes supported over a Si_3N_4 mesh were measured via bending experiments with an AFM cantilever. A nonlinear change to the elastic moduli for both bending and stretching was observed as a function of thickness, with large increases observed below 30 nm.[243] Other modes of active straining of oxide membranes have been demonstrated. Thin films transferred to stretchable polyimide layers were shown to withstand strains greater than 8%.[244] Using this method to apply tensile strain to freestanding $SrTiO_3$ films resulted in the formation of in-plane polarized ferroelectric domain structures with 180° domain walls,[245] akin to the strain-induced ferroelectric transition in substrate-supported $SrTiO_3$ (Section 2.3.2). Bending of freestanding ferroelectric capacitor heterostructures transferred to flexible substrates has also been demonstrated as a means to control the dielectric tunability of ferroelectrics (Figure 8d–f).[235] In this example, concave bending resulting in compressive strain of the ferroelectric layer resulted in enhancements in dielectric permittivity upward of 50%. Another means for controlling the properties of freestanding films is through strain imposed by the epitaxial electrodes. When an electrode–ferroelectric–electrode trilayer is released from the substrate, the lattice will adopt a structure based on the balance of elastic compliance and thickness of the various layers. Choosing the appropriate electrode thickness thus makes available a continuous tuning of the strain imposed on the ferroelectric layer. Such control has been demonstrated in freestanding $BaTiO_3$ where ferroelectric properties including the c/a lattice parameter ratio, T_C, remnant polarization, and coercive field could be controlled via electrode-imposed strain.[235] Those results illustrate the promise of freestanding ferroelectrics to provide all of the strain-induced phenomena associated with epitaxial deposition, in an active, continuous fashion. Aside from providing further methods of strain control, it was found that the freestanding membranes had markedly increased switching speeds and reduced coercive fields, pointing to the significant role that elastic constraints can play in ferroelectric switching processes and warranting further study.[246] Utilizing freestanding membranes of oxide ferroelectrics is still in its infancy, and researchers are envisioning new experiments in hybrid epitaxy to combine perovskite and nonperovskite layers to achieve new ferroic coupling, for example, magnetoelectric coupling,[247] as well as novel Moire pattern physics in oxide systems.[248]

4. New Materials and Epitaxy

The great successes of ferroelectric thin-film research and the general methodologies afforded to the study of epitaxial thin films have driven interest in applying these approaches to a broader class of polar materials. Thin-film-based studies of

relaxor ferroelectrics, for instance, have lagged those of their ferroelectric cousins, and the understanding of relaxors stands to benefit greatly from studies employing epitaxy. Moreover, a broad push toward discovering new functional materials, and in particular metastable compounds, through automated computational methods is particularly amenable to the discovery of new polar systems. Here, we discuss how epitaxy is being used to advance the understanding of materials outside of the classical ferroelectric systems.

4.1. Relaxor Ferroelectrics

The control and understanding of ferroelectric thin films has come a long way since the advent of oxide epitaxy, but other polar materials have not necessarily received the same treatment. While relaxor ferroelectrics (**Figure 9**) were discovered not long after the discovery of ferroelectric $BaTiO_3$,[249] thin-film synthesis has been limited, in part due to their chemical complexity, known problems with achieving phase pure films, and lack of large-lattice parameter oxide substrates that would allow for the production of coherently strained films.[250] At the same time, studies have heavily relied on single-crystal samples to understand the chemical disorder and complex polar structure that drives ultrahigh piezoelectric responses. Even with such pristine samples, however, the polar structure and/or origin of desirable piezoelectric responses remains the subject of much debate.[251,252] In general, it is agreed that disordered, nanometer-sized polar regions or domains are responsible for novel properties in such materials. Where researchers differ, however, is the nature of order within and surrounding these regions, with the predominant theory for many years focused on so-called polar nanoregions embedded in a nonpolar, paraelectric matrix.[253,254] More recently, however, this description has come under scrutiny,[255] and an alternative theory suggesting the polar structures are best described as nanodomains separated by low-angle domain walls, which behave like an ice-water slush, rather than as isolated entities, has been put forward (**Figure 10**a).[256] This debate is, in part, fueled by the difficulty in developing a coherent picture from the many unique approaches taken to analyzing relaxor structure and properties.[252] The study of relaxor ferroelectrics thus stands to benefit from the more holistic approach applied to the study of ferroelectric thin films, wherein macroscopic, microscopic, and theoretical techniques can be combined to develop a more comprehensive understanding.

The nanoscale disorder driving relaxor responses necessitated advanced characterization techniques. One of the most critical structural characterization techniques for the study of relaxors is X-ray diffuse scattering, wherein the polar disorder associated with randomly oriented off-centering of polar cations (often lead) gives rise to an additional diffuse intensity about X-ray or neutron Bragg diffraction peaks. This diffuse scattering can provide a quantitative measure of the size, shape, and orientation of the nanoscale polar regions in a relaxor.[257–259] In the past, such studies have been limited to single crystals, but

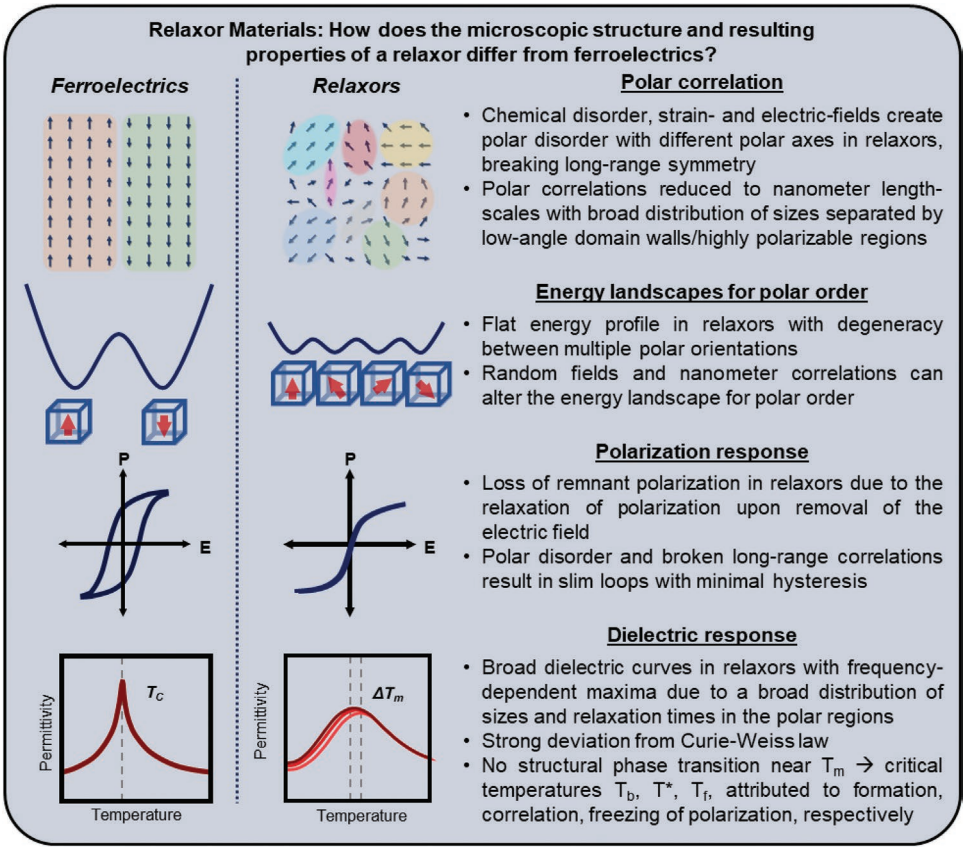

Figure 9. A comparison of ferroelectric and relaxor materials.

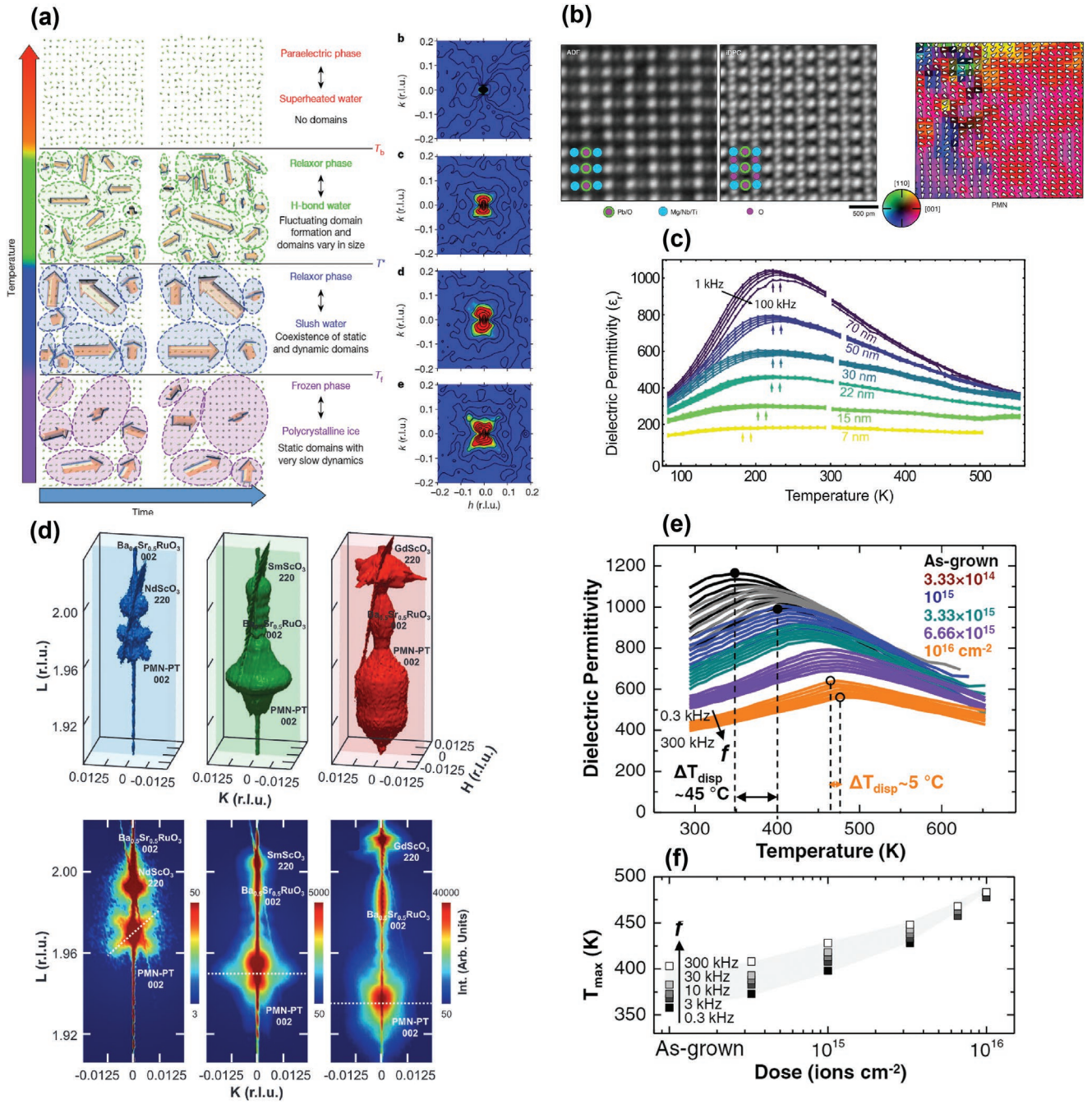

Figure 10. a) Schematic of slush-like model for the phase transitions in relaxors. Reproduced with permission.[256] Copyright 2017, Springer Nature. b) Left) Annular dark-field (ADF) and integrated differential phase contrast (iDPC) images for $PbMg_{1/3}Nb_{2/3}O_3$ single crystals along the <110> projection. (Right) Projected displacement (polarization) for the $PbMg_{1/3}Nb_{2/3}O_3$ unit cells in representative iDPC images atomic resolution polarization mapping. The projected displacement (polarization) magnitude ranges from 1 to 20 pm and is indicated by luminosity. Reproduced with permission.[266] Copyright 2020, The Authors, published by Springer Nature. c) Temperature-dependent dielectric permittivity studies for $PbSc_{0.5}Ta_{0.5}O_3/SrRuO_3/DyScO_3$ heterostructures show the suppression of permittivity at reduced thickness. T_m (marked with arrows for 1 and 100 kHz) changes only below 22 nm. Reproduced with permission.[262] Copyright 2020, American Physical Society. d) 3D reciprocal space mapping about the $0.68PbMg_{1/3}Nb_{2/3}O_3$–$0.32PbTiO_3$ 002-diffraction condition for heterostructures grown on $NdScO_3$, $SmScO_3$, and $GdScO_3$(110) substrates, corresponding to –0.5%, –1.0%, –1.5% compressive epitaxial strains, respectively. Reproduced with permission.[261] Copyright 2019, Wiley-VCH. e) Dielectric permittivity as a function of temperature and frequency (0.3–300 kHz) for $0.68PbMg_{1/3}Nb_{2/3}O_3$–$0.32PbTiO_3$ thin films bombarded with various He^{+2}-ion doses, along with f) extracted values of $T_{max.}$ as a function of ion dose at various frequencies (0.3–300 kHz). e,f) Reproduced with permission.[278] Copyright 2019, American Physical Society.

advances in diffraction techniques now allow diffuse-scattering measurements to be performed on small sample volumes, and over large portions of reciprocal space,[260] allowing 3D scattering to be measured on thin films.[261,262] Of particular interest is the evolution of the polar structure under applied fields, due to the large electromechanical coupling associated with relaxors particularly in compositions near the MPB. Diffuse-scattering experiments have been carried out on single crystals under applied electric field, with surprising results.[263] More recently, such studies have been carried out on thin films utilizing synchrotron-based X-ray microdiffraction to focus an X-ray beam onto an individual capacitor just tens-to-hundreds of micrometers across and thus observe polarization rotation from rhombohedral (R) to tetragonal (T) phases in action. In $0.68PbMg_{1/3}Nb_{2/3}O_3$–$0.32PbTiO_3$ films, it was found that the multiple polarization orientations persist even at high fields and that the rotation pathway through the M_a (monoclinic distortion of R) and M_c (monoclinic distortion of T) phases was strongly frequency-dependent.[264] X-ray diffraction, even with a micrometer-scale spot, can probe the nanoscale structure through diffuse scattering, yet these measurements provide an averaged picture of a complex structure. The recognition that the local coupling of chemical, structural, and polar disorder is critical for understanding relaxors and has driven interest in mapping such disorder with TEM-based approaches to develop real-space understanding.[265] Combining annular dark field (ADF) and integrated differential phase contrast (iDPC) into STEM has allowed for simultaneous imaging of cation- and anion-sublattices in various compositions of $(1–x)PbMg_{1/3}Nb_{2/3}O_3$–$xPbTiO_3$. Here, researchers were able to directly relate polar displacements to local structural and chemical inhomogeneities (Figure 10b).[266] Such experiments are now being applied to thin films under applied heating and fields to understand local responses in relaxor systems. These advancements in characterization are enabling the understanding of relaxor thin films and enabling new modes of control.

Questions which have been widely studied in ferroelectric thin films, such as those around size effects and the role of strain in manipulating polar, had, until recently, remained essentially unexplored in relaxors. In just the last few years, for example, films of $PbSc_{0.5}Ta_{0.5}O_3$ deposited on $DyScO_3$ substrates were used to explore the question of thickness scaling in relaxors.[262] In films >30 nm thick, no change to T_b, T^*, or T_m (see Figure 9 for details on these various temperatures) was observed, yet the polarization and dielectric responses were continually suppressed with decreasing thickness (Figure 10c). In films <30 nm thick, however, a rapid collapse of critical temperatures as well as the polarization and dielectric response was observed, until at ≈7 nm, the films behaved like linear dielectrics. This collapse coincided with reducing the thickness below the polar correlation length of ≈20 nm (as extracted from diffuse-scattering measurements), suggesting a lower limit for thickness for large responses in relaxors. The availability of large lattice-parameter scandate substrates, for example, $SmScO_3$ and $NdScO_3$, has also made it feasible to synthesize coherently strained films of relaxors like the prototypical $0.68PbMg_{1/3}Nb_{2/3}O_3$–$0.32PbTiO_3$ and to explore the evolution of relaxor order as a function of epitaxial strain.[261] 3D diffuse-scattering measurements carried out on films under –0.5% compressive strain showed classic "butterfly" shaped diffuse scattering, and a correlation length of ≈8 nm, similar to that observed in single crystals. Increasing the epitaxial strain resulted in an increase in the correlation length to ≈13 and ≈25 nm in films under –1.0% and –1.5% strain, respectively. The "butterfly" shaped diffuse scattering was also changed to a more "disk-like" diffuse scattering indicating that epitaxial strain had driven a rotation to the domain direction to be aligned along the *c*-axis in addition to increasing the polar correlations (Figure 10d). This increased correlation at large compressive strain was associated with higher critical temperatures, but overall reduced polarization, dielectric, and piezoelectric responses. Corroborating these data were molecular-dynamics simulations, which were able to reproduce key parts of the diffuse scattering for each strain state, and provide microscopic images of the polar structure evolution with epitaxial strain. Multimodal studies leveraging structural and electrical characterizations in concert with theoretical simulations thus provide a pathway for a more holistic understanding of relaxor physics.

Such molecular-dynamics studies, as well as other first-principle-based Monte Carlo simulations have been critical in developing microscopic understanding of various relaxor systems. Compared to their more "static" ferroelectric cousins, relaxors are susceptible to thermal fluctuations that drive a dynamically evolving polar structure over short timescales. Combining first-principle effective Hamiltonian calculations with Monte Carlo simulations has been widely used to simulate relaxor polar structures,[267] providing information on dynamics, correlation lengths, temperature dependence of the polar structure of relaxors, in addition to studying the effect of strain.[268–271] The application of this approach allows for a microscopic understanding of local structure in a broad range of compositions including $PbMg_{1/3}Nb_{2/3}O_3$, $(1–x)PbMg_{1/3}Nb_{2/3}O_3$–$xPbTiO_3$, and $BaZr_xTi_{1–x}O_3$. With further increasing computing power, molecular-dynamics simulations on large supercells are now feasible and are proving to be a powerful tool for predicting and recreating experimental results in single crystals and thin films.[256] While they require development of material-specific classical potentials,[272] such simulations have been applied to common systems like $(1–x)PbMg_{1/3}Nb_{2/3}O_3$–$xPbTiO_3$, and provide a virtual platform for experimenting on relaxor thin films, including applying strain,[261] simulating dielectric response,[273] and observing phase transitions.[256] The microscopic picture developed through these simulations goes so far as to map correlations between individual dipoles, representing a new methodology for quantifying changes in an otherwise untenably complex system.

As researchers begin to employ epitaxy to manipulate and study relaxor properties, one particular area of focus is synthetic control of the polar structure. Because relaxor order is attributed to the cationic charge and size mismatch associated with disordered *B*-site cations in most relaxors,[274] control over local ordering in such systems could enable a new degree of control over relaxor properties. One such attempt involved sequential deposition of niobium- and magnesium-rich layers onto a (111)-oriented substrate to induce long-range chemical ordering of the *B*-site cations in $PbMg_{1/3}Nb_{2/3}O_3$ thin films.[275] Whereas long-range order cannot be achieved in $PbMg_{1/3}Nb_{2/3}O_3$ ceramics, deposition enabled synthesis of films

with more chemically ordered regions on the order of 100 nm wide. Meanwhile, recognition that competition and disorder are responsible for their highly susceptible polarization response, other researchers have attempted to increase such competition by stabilizing solid solutions of ferroelectric and dielectric systems, for example, in $(1–x–y)BiFeO_3–(x)SrTiO_3–(y)BaTiO_3$ films, which were reported to exhibit ultrahigh density energy storage.[276,277] Forcing competition between cubic $SrTiO_3$ and the ferroelectric phases of rhombohedral $BiFeO_3$ and tetragonal $BaTiO_3$ creates a highly degenerate energy landscape for polar distortions. Engineering disorder, however, is not always straightforward. Based on the understanding of defect formation in ion-bombarded ferroelectric films, researchers studying the role of defect-induced structural disorder in $0.68PbMg_{1/3}Nb_{2/3}O_3–0.32PbTiO_3$ films found that increased defect concentrations resulted in reduced relaxor-like response, with decreased permittivity and associated frequency dispersion of the dielectric maximum (Figure 10e,f).[278] In the case of ion bombardment, defects (and defect dipoles) serve to pin otherwise mobile polarization and stabilize a preferred polarization direction, reducing the dielectric and polarization responses. The study of relaxors as epitaxial thin films is still relatively new, and yet understanding of polar structures and responses has already benefitted greatly.

4.2. Beyond Perovskite Ferroelectric Oxides

Historically, the occurrence of ferroelectricity in oxides has been found to be favored by the presence of small, highly polarizable cations within a corner-sharing oxygen octahedron. This criterion is satisfied by multiple oxide-based structures, other than the ABO_3-type perovskites, including layered perovskite, tungsten-bronze, and pyrochlore structures. Additionally, polar order in binary oxides and hexagonal perovskites have posed important questions about the mechanism(s) of ferroelectricity. Advances in both computational prediction and thin-film synthesis have opened the door to discovery and design of new materials with potential for uncovering unexplored mechanisms for polar order and functionalities unavailable in traditional ABO_3-type oxides.

4.2.1. Layered Perovskites

Bismuth-based layered perovskite structures of the form $Bi_2A_{m-1}B_mO_{3m+3}$ (where $A = Na^+$, K^+, Ba^{2+}, Bi^{3+} and $B = Fe^{3+}$, Ti^{4+}, Nb^{5+}, W^{6+})[279] were explored in the 1990s for potential application in nonvolatile ferroelectric memories as fatigue-resistant alternatives to $PbZr_xTi_{1-x}O_3$, optoelectronic devices, and as high-k dielectrics.[280–283] The structure consists of m layers of perovskite-like BO_6 octahedra between $(Bi_2O_2)^{2+}$ layers in a monoclinic or orthorhombic unit cell. In $Bi_4Ti_3O_{12}$, for example, the tetragonal phase is paraelectric and transforms to a ferroelectric monoclinic phase driven by displacement of the Bi^{3+} and Ti^{4+} cations along a polar axis that is rotated away from the a-axis toward the c-axis by 4°–5°. The resulting structure exhibits a relatively large spontaneous polarization (≈50 μC cm^{-2}) along the a-axis.[284] Additionally, the chemical flexibility and ability to modify the layering of this system has been used to engineer relaxor,[285] photovoltaic,[286] and multiferroic[287,288] properties. While the complex layered structure (Bi_2O_2 layers and crystallographic glide planes) enables multiple functionalities, it also limits the epitaxial orientations that can be achieved on perovskite substrates. Specifically, the half-unit cell translation between one triple-perovskite layer and the next along the c-axis precludes synthesis of high-quality films with the polar a-axis out-of-plane, since half of the layers will be mismatched with perovskite substrates.[289] In order to leverage the high fatigue resistance provided by this material class, new synthetic approaches to achieve epitaxial thin films of layered perovskites on perovskite substrates must be developed.

4.2.2. Tungsten-Bronze Structures

Tetragonal tungsten-bronze (TTB) compounds, with a complex chemical structure $(A1)_2(A2)_4(C)_4(B1)_2(B2)_8O_{30}$,[290] span an expansive set of materials with diverse dielectric and magnetic behavior. The structure can be described as a network of distorted, corner-sharing BO_6 octahedra, with $A1$-, $A2$-, and C-type interstices forming pentagonal, square, and triangular tunnels, respectively.[291–293] The large number of cationic sites enable researchers to carefully tune properties of interest through chemical substitution. Many TTB compounds are either ferroelectrics or relaxors and are largely influenced by a difference in $A1$–$A2$ ionic radii, with smaller $A1$ cations favoring ferroelectric nature.[294–296] The $Ba_2LnFeNb_4O_{15}$ (where Ln is a lanthanide such as La^{3+}, Nd^{3+}, Eu^{3+}, Sm^{3+}, etc.) family of TTBs belong to a unique class of composite room temperature multiferroics, in which magnetic $BaFe_{12}O_{19}$ spontaneously forms within the ferroelectric $Ba_2LnFeNb_4O_{15}$ matrix.[297,298] Though first discovered as bulk ceramics,[299] this phenomenon has recently been extended to epitaxial thin films as well.[297,298,300] Despite the large chemical flexibility, synthesis of epitaxial films is still limited, as with the layered perovskites, due to the structural mismatch between the layered structure and currently available substrates.

4.2.3. Pyrochlores

Though possessing a relatively simpler crystal structure than the preceding cases, pyrochlores, with formula $A_2B_2O_7$, have received considerable attention in recent years, largely due to their unique electronic and magnetic structures which have been found to exhibit exotic electronic properties including superconductivity, spin-liquid states, spin-ice states, and other novel spin textures.[301–306] The octahedral network is far more disordered than the ABO_3 perovskites, giving rise to more disordered polar structures, which is thought to be a limiting factor for long-range ferroelectric order in pyrochlores.[307] Nevertheless, reports of ferroelectric phases in systems like $Cd_2Nb_2O_7$[308] suggest a route to engineering pyrochlores where even weak ferroelectric order may be coupled with exotic magnetic or electronic states to create exotic new functionalities. Additionally, certain pyrochlore oxides (e.g., $Sn_2Nb_2O_7$, $Bi_2Ti_2O_7$) have been predicted to possess quasiflat electronic

band structures near the fermi level which has the potential to induce effects like superconductivity, quantum Hall effects, and various topological states.[309] While, the chemical compatibility between the pyrochlore and perovskite structures suggests a path toward synthesizing multifunctional thin films, the large lattice parameters[310] (e.g., $a = 10.365$ Å for $Cd_2Nb_2O_7$[306]) associated with pyrochlore phases makes synthesizing high quality epitaxial films on the commercially available perovskite substrates a major obstacle. Additionally, pyrochlore phases as ferroelectrics tend to have a T_C below room temperature (e.g., $T_C =$ 205 K for $Cd_2Nb_2O_7$[306]) which limits their utility in real-life applications. Advanced thin-film fabrication using appropriate compositional modification or buffer layers can be helpful in tailoring the pyrochlore phases favorably while retaining their useful functionalities.

4.2.4. Hexagonal Perovskites and Improper Ferroelectricity

Even within the typical ABO_3 chemistry, alternative ferroelectric structures have been studied. Specifically, a class of hexagonal rare-earth manganites $ReMnO_3$ (Re = Sc, Y, Dy–Lu), first reported in 1963,[311] and other isostructural compounds such as $LuFeO_3$, offer a new perspective on the role of crystal structure in ferroic order. While most ferroelectrics exhibit key similarities in electronic configuration, namely a d^0 and/or $6s^2$ cation, which are responsible for their net spontaneous polarization, ferroelectricity in hexagonal perovskites is classified as improper in that it arises due to a buckling of oxygen polyhedra and trimerization of apical oxygen anions, resulting in the offset of rare-earth cations and generating a relatively small polarization (1–5 μC cm^{-2}) along the *c*-axis (**Figure 11**a).[312] This phenomenon is often termed geometric ferroelectricity due to the constraints imposed by the size mismatch of the *A* and *B* cations.[313] The unique mechanism of polar distortion gives rise to ferroelectric physics fundamentally different from that observed in more typical perovskites. For example, a strong frequency dispersion of the coercive field in $LuFeO_3$ thin films was measured, along with defect-enhanced switching, in contrast with results reported for traditional ferroelectric $PbTiO_3$ films.[314] In $ErMnO_3$, complex domain structures have been observed, including topologically protected trimerized vortex domains[315] and charged domain walls that can be reversibly switched on and off.[316] Below 70–90 K, geometric frustration of Mn^{3+} produces planar 120° noncollinear antiferromagnetic order with four possible orientations, denoted A_1, A_2, B_1, and B_2 (Figure 11a).[317,318] While the ground state B_2 phase forbids linear magnetoelectric coupling, the application of a large enough magnetic field along the *z* axis promotes a transition to the A_2 phase, generating a net magnetic moment M_z due to a canting of Mn^{3+} spins.[317] Using magnetoelectric force microscopy (MeFM), a technique combining magnetic force microscopy (MFM) with in situ modulated electric fields, magnetoelectric domains have been observed and can be mapped directly to ferroelectric domains in the same region (Figure 11b,c). In addition to direct multiferroism, hexagonal perovskites also enable a new path toward composite multiferroics. For example, $LuFeO_3/LuFe_2O_4$ superlattices synthesized via MBE demonstrated coupling of the improper ferroelectricity from $LuFeO_3$ and ferrimagnetism from $LuFe_2O_4$ at room temperature. In addition to rare-earth manganites and ferrites, recent reports of high-pressure synthesis of metastable rare-earth indates,[319] as well as first-principle calculations predicting analogous compounds in the rare-earth gallates,[320] suggest new system which may be stabilized through epitaxy. While the production of high-quality epitaxial films of hexagonal perovskites is still limited by the availability of substrates and appropriate electrodes, further advances in the understanding of ferroelectric physics in these materials stand to expand the realm of ferroelectricity.

4.2.5. Binary Structures

Whereas the materials discussed above are (generally) far more complex than typical ABO_3 perovskites, there is emerging interest in binary compounds that exhibit ferroelectricity.[321] HfO_2, in particular, is commonly used as a high-κ gate dielectric layer in MOSFET and dynamic random-access memory (DRAM) architectures, but the discovery of ferroelectricity in $Hf_{1-x}Si_xO_2$ promised a potentially simple route toward integration of ferroelectrics into existing fabrication processes.[322] Initial studies focused on ALD of polycrystalline thin films[188,322–324] but have recently evolved to include epitaxial films grown in yttria-stabilized zirconia,[325] pyrochlore electrodes,[326] and even directly on silicon through in situ scavenging of native SiO_2.[327] While, chemical substitution (including with silicon, aluminum, yttrium, strontium, lanthanum, gadolinium, etc.) has been the main route to stabilizing the metastable ferroelectric phase,[328] and, in particular, ferroelectricity has been confirmed over a wide composition range in $Hf_{1-x}Zr_xO_2$, prepared both by ALD and PLD.[326,329] From this work, however, the understanding of unconventional ferroelectricity in this system has been leveraged to induce ferroelectric phases in both the binary compounds HfO_2 and ZrO_2.[330]

As interest in HfO_2- and ZrO_2-based ferroelectrics grows, a number of new approaches for stabilizing ferroelectric phases have been developed. In HfO_2 films deposited with chemical solution deposition, PLD, or ALD, it has been shown that control of film thickness/crystallite size,[14,323,326,331] for example, in epitaxial $Hf_{0.5}Zr_{0.5}O_2$ films with pyrochlore electrodes, reducing film thickness below 30 nm, results in the ferroelectric orthorhombic structure; increasing the thickness above this value allows for formation of the non-ferroelectric monoclinic phase.[326] On the other hand, $Hf_{0.8}Zr_{0.2}O_2$ films deposited by ALD on silicon remain polycrystalline down to nearly 2 nm, below which films become textured and adopt a ferroelectric phase, as confirmed by grazing-incidence X-ray diffraction (GI-XRD). Due to the difficulty of probing structural distortions in ultrathin films, particularly in polycrystalline films, X-ray absorption linear dichroism (XLD) has been used to probe the orbital asymmetry associated with non-centrosymmetric distortion of the oxygen tetrahedra (Figure 11d). The inversion in the oxygen absorption at reduced thickness demonstrates a change in the electronic structure accompanying the formation of the ferroelectric orthorhombic phase observed via GI-XRD.[14] This sort of "reverse" size effect, wherein a ferroelectric phase is stabilized, rather than destabilized at reduced thickness

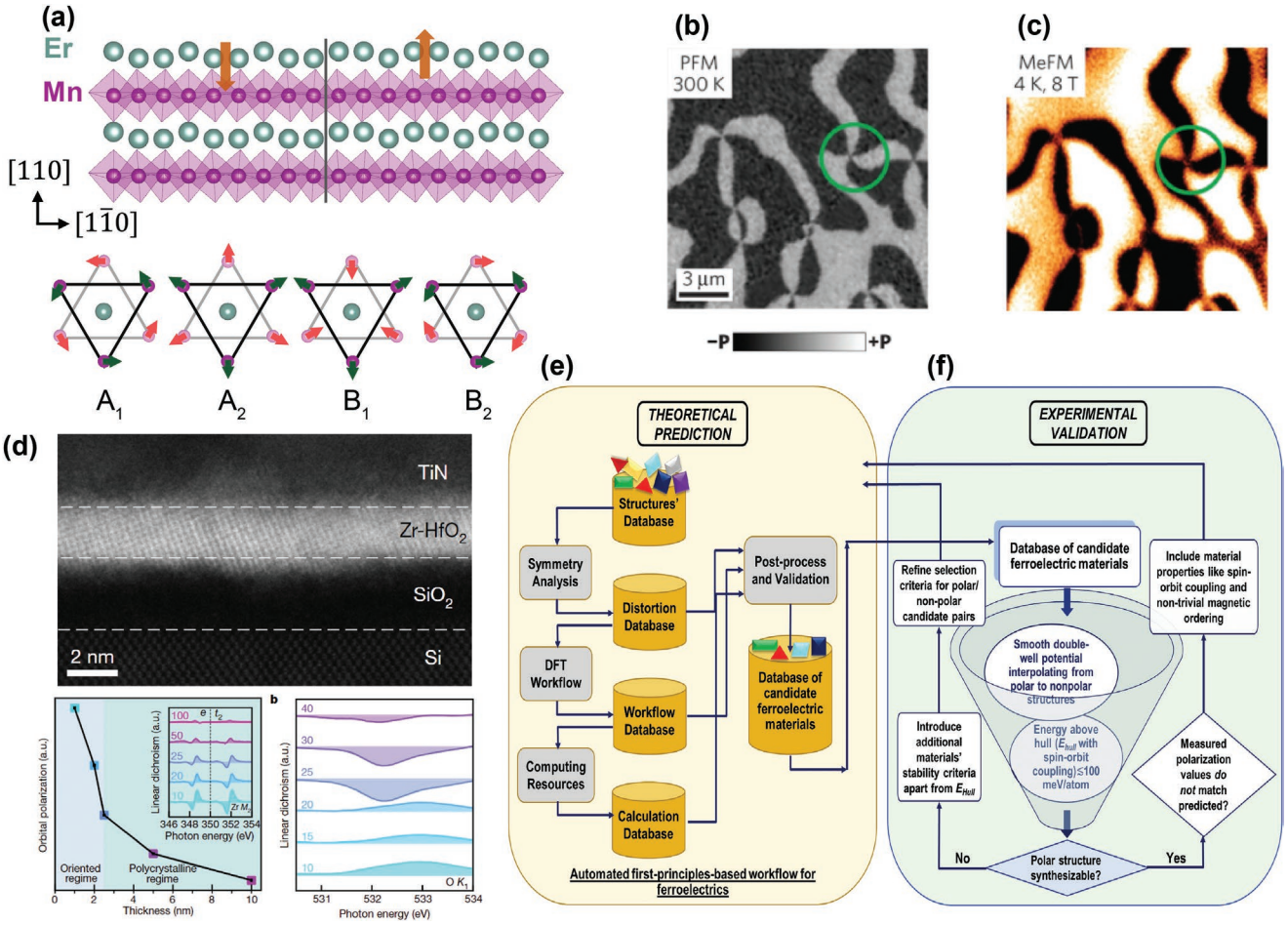

Figure 11. a) Schematic mechanism for ferroelectricity in hexagonal $ErMnO_3$. A net polarization is observed in the alternating pattern of Er^{3+} cations induced by a trimerization of apical oxygen on the Mn^{3+} octahedra. b) This mechanism results in unique vortex domain structures observable in PFM scans of 001-oriented single crystals. The presence of magnetically active cations enables antiferromagnetic order in four possible orientations allowed by the crystal symmetry, where B_2 is the ground state order and A_2 is induced by a strong enough magnetic field along the *z*-axis and exhibits a net magnetic moment in the [001]. The dark purple circles and their associated green spin direction arrows represent the top layer of Mn^{3+} cations, while the lighter pink circles and their associated red spin direction arrows represent the underlying layer of Mn^{3+}, separated by Y^{3+} cations. c) Magnetic order is observed to be coupled to ferroelectricity, as seen in MeFM scans of the same region as (b). b,c) Reproduced with permission.[317] Copyright 2014, Springer Nature. d) Top) Representative TEM scans of highly oriented, ultrathin (2 nm) Zr–HfO_2 on Si. Bottom left) Orbital polarization is seen to increase with decreasing thickness as observed in XLD of the Zr M_2 edge (inset). This enhancement corresponds to a significant degree of crystal alignment, as indicated by (bottom-right) an inversion in the XLD of the O K_1 edge at lower thicknesses. Reproduced with permission.[14] Copyright 2020, The Authors, published by Springer Nature. e) Automated first-principle-based workflow for ferroelectrics. f) Proposed refined workflow for searching new ferroelectric candidates. e,f) Reproduced with permission.[355] Copyright 2020, American Chemical Society.

demonstrates the potential for novel ferroelectric behavior in other nonperovskite systems that can help circumvent limitations to traditional ABO_3 ferroelectrics. In ZrO_2, on the other hand, a field-driven ferroelectric transition has been observed to stabilize ferroelectricity in films with thicknesses on the order of several hundreds of nanometers. This so-called "wake-up" effect, wherein cycling an electric field across the ZrO_2 film gradually increases the remnant polarization, has been attributed to an electrically driven redistribution of oxygen vacancies, which facilitate a structural transition to the orthorhombic $Pca2_1$ phase.[329] These novel mechanisms for ferroelectricity promise new routes toward tackling classic problems of depolarization and finite-size effects faced in conventional perovskite ferroelectrics.

While these results are promising for rapid integration of ferroelectrics into existing CMOS-compatible processes, the key factor preventing integration of HfO_2- and ZrO_2-based ferroelectrics is their high coercive field, which leads to increased power consumption and reduced cycling endurance in devices. This behavior has been suggested to be intrinsic to HfO_2, arising from thin domain walls with exceedingly large energy barriers to motion, thus preventing the efficient nucleation and growth of domains.[332] One recent approach to solving this problem is to engineer a domain wall with more favorable switching. First-principle calculations suggest that inserting nonpolar spacer layers between oppositely poled regions will form a new type of topological domain wall that does not require a chirality reversal for expansion,[333] thereby reducing

the energy cost for domain growth. These simulations inspired the synthesis of alternating polar/nonpolar $Hf_{0.5}Zr_{0.5}O_2/ZrO_2$ nanolaminates where formation of a nonpolar phase at domain walls acts as a "grease" to increase domain-wall mobility, ultimately resulting in a 40% decrease in the coercive field.[334] Further work combining theory and experiment on these unconventional ferroelectrics will be essential in addressing problems of high coercive fields and poor fatigue resistance typical of ferroelectric HfO_2- and ZrO_2-based materials, yet the demonstration of switchable polarization in a material amenable to current industry processes is promising for its near-future integration into novel ferroelectric devices.

In just the last few years, ferroelectricity has also been reported in several wurtzite-structured compositions. The wurtzite structure, typical of several common semiconductors, including AlN and ZnO, lacks inversion symmetry and is a known pyroelectric. Switchable ferroelectric polarization, however, had not been achieved with electric fields lower than the breakdown strength of the compounds. Recently, chemical substitution of polar wurtzite compounds has been shown to induce a switchable polarization. Initially predicted in DFT simulations,[335,336] switchable polarization in a wurtzite structure was ultimately achieved in $Al_{1-x}Sc_xN$, where ferroelectricity has been observed in compositions with x = 0.1–0.42 with increasing scandium content reducing the coercive field and remnant polarization.[337] Several studies have since confirmed ferroelectric switching in various $Al_{1-x}Sc_xN$ compositions, reporting large polarizations near 100 μC cm^{-2} and large coercive fields of several MV cm^{-1} and switchable polarization in films as thin as 9 nm.[338,339] In this system, substitution with scandium serves to stabilize a metastable intermediate structure similar to the nonpolar, hexagonal ScN structure, ultimately reducing the ionic potential between the two stable polar wurtzite states.[337] Ferroelectricity has also been reported in $Al_{1-x}B_xN$ at relatively small boron concentrations.[340] This approach has more recently been applied to other wurtzite structures including $Zn_{1-x}Mg_xO$ which has been found to exhibit ferroelectricity.[341] In a similar fashion to $Al_{1-x}Sc_xN$, $Zn_{1-x}Mg_xO$ was found to exhibit switchable polarization with large (≈100 μC cm^{-2}) remnant polarization and large (≈2 MV cm^{-1}) coercive fields in films with x = 0.3–0.37. For $Zn_{1-x}Mg_xO$ compounds with $x < 0.3$, electrical breakdown occurs before the coercive field is reached due to the relatively small bandgap of pure ZnO. As such, substitution with magnesium both increases the bandgap and stabilizes a hexagonal intermediate state, allowing for switchable polarization.[342] Interestingly, these ferroelectric $Zn_{1-x}Mg_xO$ compositions also undergo a "wake-up" process resembling that seen in HfO_2- and ZrO_2-based ferroelectrics. Recent results suggest that destabilization of strongly polar, but not yet switchable, structures may provide new routes to accessing ferroelectricity in many nonperovskite crystal structures. Like HfO_2-based materials, synthesis and fabrication of semiconductors in existing processes is well developed. As such, studies of the mechanisms underlying ferroelectricity in these compounds and efforts aimed at reducing the (potentially) prohibitively large coercive fields are key to realizing the promise for such new routes for integration of ferroelectrics in future devices.

4.3. Discovery and Design of Ferroelectric Materials

While most of the families of commonly used ferroelectrics were discovered as a result of chemical intuition driven trial-and-error approaches, the need to systematically study and engineer polar materials has been rising steadily. Despite a growing number of potential applications, the community still primarily uses a few "classic" systems that are, in many cases, not well suited or designed for all the applications they are used in or considered for. With advances in first-principle approaches, the ability to generate and manage a large volume of computational data (relaxed crystal geometries and the associated total energy/atom, electronic band structures, and density of states) in open repositories has improved. Hence, an increasing number of electronic-structure databases consisting of both theoretical and observed compounds have emerged.[343] DFT has evolved as a popular route for assessing the spontaneous electric polarization for the polar compounds using the Berry-phase approach.[344] Further, combining perturbation theory with DFT has unlocked a relatively easy way of determining functional properties such as phonon frequencies, elastic constants, optical and static dielectric constants, piezoelectric tensors, and others. While thermodynamic stability criteria like energy above hull[345] and the amorphous limit[346] act as primary descriptors to assess the synthesizability of a compound, additional descriptors have been used to screen materials' databases and populate automated databases with targeted functionalities by employing high-throughput workflows.[347–350] Historically for ferroelectrics, group-theory-based symmetry criteria have been used to screen through the Inorganic Crystal Structure Database and identify potential ferroelectric candidates.[351–353] With advances in modeling Hamiltonians with "artisanal" ab initio calculations, some studies combined both DFT and principles of group–subgroup relations to identify and model the paraelectric-to-ferroelectric structural phase transition. Others used the presence of soft phonon modes through vibrational studies to propose potential ferroelectric candidates.[347,350,354] The screening criteria in the automatically curated databases constantly need to be reevaluated and augmented based on the input obtained from experimental trials for improved accuracy. One such attempt was made with a new and relatively unexplored ferroelectric candidate, $BiInO_3$, which underlined the importance of the magnitude of the barrier along the energy pathway calculated by DFT across the nonpolar to polar structural distortion.[355] Hybrid workflows (Figure 11e,f)[355] combining both computational and experimental aspects are likely to accelerate the process of rationally designing new materials and/or realizing new functionalities in the known materials.

Combining such high-throughput approaches with versatile synthesis approaches, such as PLD or MBE, promises to rapidly expand the realization of novel ferroelectric materials in a systematic manner. Taking inspiration from some of the earliest theoretical predictions of strain-induced ferroelectricity in $SrTiO_3$ (Section 2.3.2), several materials with completely novel functionality have been realized through theory-driven discovery. One prime example is that of $PbVO_3$, which was predicted to form with a supertetragonal structure (i.e., c/a = 1.229) composed of vanadium–oxygen square pyramids (rather than the typical octahedra in perovskites of the same generic

chemistry) and to exhibit simultaneous antiferromagnetic order and a large ferroelectric polarization (≈152 μC cm^{-2}).[356] Initial attempts at synthesizing $PbVO_3$, which is usually unstable due to the unfavorable V^{4+} oxidation state, utilized high-pressure synthesis and resulted in bulk specimens with tetragonal $PbVO_3$ along with several phase impurities.[357] Taking inspiration from the high-pressure bulk synthesis, single-phase thin films of $PbVO_3$ were synthesized by leveraging biaxial compressive strain imposed via PLD on (001)-oriented $LaAlO_3$ substrates. The resulting films exhibited a tetragonality ($c/a = 1.32$) larger than that reported in the bulk phase (i.e., $c/a = 1.229$).[358] Piezoelectricity was subsequently confirmed via PFM along with antiferromagnetic order below 130 K.[359] Similar ideas of stabilizing metastable vanadate compounds using epitaxy have been extended to KVO_3 and $NaVO_3$ using DFT calculations.[360]

Another example of successful theory-guided discovery of new ferroic materials was the synthesis of $EuTiO_3$ thin films which demonstrated simultaneous ferroelectric and ferromagnetic orders.[361] First predicted via first-principle studies, it was suggested that biaxial compressive strain could drive a transition from the antiferromagnetic, quantum paraelectric ground state to both ferromagnetic and ferroelectric orders.[61] Limited by the availability of suitable substrates to provide the requisite compressive strain, researchers utilized tensile strain by depositing $EuTiO_3$ on $DyScO_3$ substrates, inducing a ferroelectric transition around 250 K and ferromagnetic transition below 5 K.[361] These cases only serve as examples of how leveraging the capabilities for manipulation of materials' structure and chemistry through thin-film epitaxy provides the means to experimentally realize materials predicted via newly developed high-throughput techniques.

While a great majority of the theoretical work concerns primarily the ABO_3 perovskite materials due to the simplicity of the crystal structure, the control of octahedral tilt in other families of complex oxides like layered *A*-site-ordered double perovskites, superlattices, and Ruddlesden–Popper phases has been equally interesting. In fact, layering of nonpolar perovskites has been found to induce a new type of ferroelectricity in which controlled octahedral rotations can induce electric polarization which can be then manipulated using an external electric field. One such specific example would be replacing alternating LaO layers in $LaGaO_3$ with YO to form a $LaYGa_2O_6$ superlattice. Considering the strong tendency of $LaGaO_3$ and $YGaO_3$ to form a nonpolar *Pnma* structure individually forces their superlattice to exhibit $a^-a^-c^+$ octahedral tilt pattern.[362] This further leads to a net polarization due to the antipolar displacement of La and Y ions which do not completely cancel each other, resulting in a net "ferrielectric" polarization while driving the overall symmetry of the superlattice to be polar ($Pmc2_1$). Another fascinating example of such an approach being applied has been in the $Sr_3Zr_2O_7$ (Ruddleson–Popper) phase. The phonon dispersion curves in the distortion-free *I*4/*mmm* phase were calculated along multiple directions in the Brillouin zone to determine the energy-lowering and symmetry-reducing atomic displacement patterns with unstable (imaginary frequency) phonon modes and helped identifying $A2_1am$ as a favorable ferroelectric structure.[116,363,364] Such predictions about new polar materials, however, need to be questioned cautiously as many of the exotic material properties and chemistries may not be stable and feasible for synthesis as thin films.[365] Such lack of certainty necessitates for new advances in ab initio synthesizability descriptors, as well as appropriate feedback and integration with experimental approaches for more fully automated synthesis workflows.

4.4. Enabling Epitaxial Thin Films of New Ferroelectric Oxides

A key step in studying strain-enabled or strain-enhanced functionalities in both newly predicted and existing oxides as high-quality epitaxial thin films is expanding the range of available crystalline templates for epitaxy. A wide variety of perovskite-, fluorite-, and rock-salt-based single crystal substrates (with lattice parameters 3.68–5.13 Å) are commercially abundant. With an increasing number of functional perovskite oxides with pseudocubic (subscript "pc") lattice parameters larger than 4 Å, there is a serious dearth in available perovskite substrates, with a_{pc} = 4.01 Å ((110)-oriented $NdScO_3$) as the largest lattice parameter which can strain a perovskite-based system epitaxially. The recent developments in growth of single crystals of $LaScO_3$, $LaLuO_3$, and their solid solutions with a_{pc} in the range 4.05–4.18 Å are encouraging as a future avenue for exploratory studies to identify newer perovskite substrates.[366]

The relative ease of electrically stimulating a ferroelectric oxide in the out-of-plane direction as compared to that in-plane calls for new oxide-based electrodes which can be grown on the substrates with large lattice parameters. The availability of well-studied, electrically conductive oxide-based electrodes has been primarily limited to $La_{0.5}Sr_{0.5}CoO_3$, $La_{0.7}Sr_{0.3}MnO_3$, $LaNiO_3$, and $SrRuO_3$, due do their lattice parameters being in close proximity to well-studied ferroelectrics (e.g., $PbTiO_3$, $BiFeO_3$, $BaTiO_3$, etc.) However, these standards are often not ideal for less traditional materials, synthesis conditions, and/or measurements. Some electrodes with large a_{pc} under investigation are $BaPbO_3$,[367,368] transparent oxides like Sn-doped In_2O_3, Sn-doped CdO, and $CdIn_2O_4$,[369–372] and pyrochlores $Pb_2Ir_2O_7$ and $Bi_2Ru_2O_7$.[326] Apart from appropriate lattice parameters, obtaining electrodes with high conductivity is equally valuable and comes with its own set of challenges. Some highly conducting vanadates, such as $CaVO_3$[373] and $SrVO_3$[374] can only be synthesized in a low-oxygen environment to promote the +4-oxidation state for vanadium, thus making them incompatible with ferroelectric oxides which prefer an oxidizing atmosphere.[375] The chromium-based electrodes $CaCrO_3$, $SrCrO_3$,[376–378] and $SrMoO_3$[379] demonstrate a similar oxygen-sensitive behavior. All the less-studied oxide electrodes are plagued with their own set of synthesis- or conductivity-based limitations and need extensive experimental investigation to be established as standard choices for ferroelectric heterostructures.

5. Where Are Thin-Film Ferroelectrics Making Impact?

Ferroelectric materials have found relevance in a wide range of technological applications. Beginning in the 1990s, ferroelectric thin films gained considerable relevance for use in non-volatile memory-based applications. Today, in addition to new

manifestations of such memory applications, there is growing interest in these materials for next-generation logic, tunable microwave dielectrics, energy harvesting, conversion, and storage (i.e., dielectric, piezoelectric, pyroelectric, photovoltaic), nonlinear optical modulators, and other areas. Here, we review some of the major prospects for ferroelectric thin films in applications today.

5.1. Return to Nonvolatile Memories and Logic

The ability of ferroelectric materials to exhibit multiple polarization states, switch between them with an applied electric field, and to retain a state even in the absence of an applied field provides the basis for the binary code-based (Boolean algebra's "1" and "0") nonvolatile random-access memories (NVRAMs). In the 1950s, ferroelectric thin films were first pitched as potential replacements for the commercially prevalent DRAM as either NVRAMs or DRAMs based on their low power consumption, high permittivity values, faster switching speeds, and nonvolatility, encouraging a new era in digital computing.[380] This motivated further research to understand the polarization switching dynamics and the limit for the film's thickness for retaining a stable polarization state in the ferroelectric layer. In the following decades, immense progress has been made in the understanding and controlling ferroelectric polarization and this has, in turn, renewed interest in integration of ferroelectrics in devices.

While capacitor-based memories using perovskite $PbZr_xTi_{1-x}O_3$ and layered perovskites (e.g., $SrBi_2Ta_2O_9$ and $Bi_4Ti_3O_{12}$) were promising prior to the 2000s, further work was soon discontinued due to the scaling limitations and increasing cost per bit. The discovery of HfO_2-based ferroelectrics, however, has changed the scenario. Considering HfO_2 has been well-established in CMOS processes as a dielectric, it could easily address fabrication-related issues (Section 3.5) when integrated on semiconductors irrespective of the data-storage mechanism. Additionally, based on studies of certain antiferroelectric alloyed-HfO_2 compositions, which tend to have a higher field-cycling endurance than ferroelectrics,[381] the idea of antiferroelectric-based devices, where a built-in bias allows for a nonzero polarization state at zero bias, is also gaining momentum.[382,383] The major limitation for practical applications in either case, though, is the high coercive field associated with switching HfO_2-based systems which is currently an emerging field of investigation.

Furthermore, integration of (anti)ferroelectric oxides is generally predicated on achieving high remnant polarization, low-coercive fields, and fast switching speeds in ultrathin films on the order of nanometers. Thus, researchers are again turning their attention to the role of ferroelectric interfaces in dictating switching properties. Recent work points toward the impact of atomic-scale structure at ferroelectric–metal interfaces on switching properties. For example, 2 nm thick $BiFeO_3$ films deposited on $TbScO_3$ substrates were observed to form a periodic rumpled structure. Despite the relatively low lattice mismatch, the domain structure resembled that of the mixed tetragonal-like/rhombohedral phase $BiFeO_3$ films under large compressive strains (Section 2.3.2). Ultimately, the surface rumpling, and associated enhancement in polarization, was attributed to formation of a parasitic Bi_2O_{3-x} monolayer at the film surface.[384] Local structural relaxations have been found at ferroelectric interfaces, and can dramatically impact switching. In $SrRuO_3/BaTiO_3/SrRuO_3$ capacitors, asymmetric termination gives rise to a $BaO–RuO_2$ layer, creating a pinned interfacial dipole which enhances depolarization effects and facilitates backswitching of the polarization to a preferred state.[385] Including 2 unit cells of $SrTiO_3$ to change this termination layer converts the $BaO–RuO_2$ to a more symmetric $SrO–TiO_2$ interface, eliminating the interfacial pinning. Further studies leveraging atomic-scale synthesis and characterization, and particularly at ferroelectric–semiconductor interfaces, will be required to truly enable integration of ultrathin ferroelectrics.

Upon integration into a memory cell, ferroelectrics can function either with a data readout scheme that is destructive (e.g., ferroelectric random access memory, FeRAM) or nondestructive (e.g., FeFET or ferroelectric tunnel junction (FTJ)).[386] The destructive readout scheme of FeRAM involves a ferroelectric capacitor biased in a particular polarization state and the polarization state is detected by the detection (or absence of) a switching current following a read pulse. Such readout schemes, however, require a writeback as they destroy the information stored previously. On the other hand, in nondestructive readout schemes, like that in the FeFET where a ferroelectric replaces the gate dielectric of a typical FET, the change in polarization state leads to a shift in the current–voltage curve of the transistor, enabling the polarization state to be detected.[387] Finally, in a FTJ, a thin ferroelectric layer is used as a tunnel barrier and the polarization state changes the electron tunneling transmission coefficient.[388]

5.2. Beyond CMOS with Ferroelectrics

The size scaling of nanoelectronics based on CMOS transistors has been tremendously successful for the past five decades, following Moore's law of 1965[389] (i.e., that the density of transistors per chip should roughly double every two years) and Dennard's scaling of 1974[390] (i.e., that the voltage and current should scale with the size of the transistors on the chip and, thus, decrease 30% every year, with the areal power density remaining the same at a 40% higher operation frequency). Current device architectures, however, are beginning to approach sizes that encounter fundamental physical limits.[391] First, the "Boltzmann tyranny," resulting from the thermal-energy distribution of charge carriers in semiconductors, dictates a limitation of 60 mV dec^{-1} in current modulation[392,393] (the current ratio between on and off states in a transistor needs to be large enough for normal operations). Second, as the transistor size shrinks, the leakage current becomes larger, further increasing the total power consumption.[394] Researchers have, therefore, begun exploring device alternatives to fundamentally redesign the building blocks of computing beyond CMOS. New order parameters (e.g., polarization, magnetization, strain) are now being considered for computing logics and memories. These novel devices exhibit strong thresholding behavior that makes them suitable candidates to bypass the "Boltzmann tyranny" in traditional transistor structures.[393,394] Ferroelectrics, with

their bistable polarization states, are poised to enable both nonvolatility and low read/write energies through multiple device designs (e.g., FeRAM, FeFET, FTJ), as well as enable new combined logic-in-memory applications.[19,386,395,396]

With a nondestructive data-readout scheme, FeFETs (**Figure 12**a,b) combine the memory and logic functions, forming a single "logic-in-memory" device structure which can overcome the memory–logic interconnect bottleneck in traditional von Neumann architectures based on semiconductors.[395] Further, the realization of multistate polarization control that has been demonstrated through domain and defect engineering enables fundamentally new computing approaches. With potential access to multiple configurational states, FeFETs can serve as fundamental components in beyond binary ("0" and "1") architectures, including analog weight cells for deep neural networks and artificial neurons for spiking neural networks. Ferroelectrics also possess the unique potential of exhibiting negative capacitance, wherein the charge of a ferroelectric capacitor flows opposite to the applied voltage during ferroelectric switching. Integrating a ferroelectric layer into the gate of traditional FETs as a so-called negative-capacitance field-effect transistor (NC-FET) therefore allow for amplification of the applied gate voltage, steeper subthreshold slope, and ultimately overcoming the 60 mV dec^{-1} Boltzmann tyranny, thus providing a pathway to massive data processing with high throughput and energy efficiency.[397–400] On the other hand, the small tunneling current density in FTJ operation can be beneficial for massive parallel operation and synapse fabrication in neuromorphic applications.[401,402] There are challenges associated, however, with the integration of the ferroelectric materials onto the semiconductor substrate (Section 3.5). The discovery of ferroelectricity in HfO_2-based systems (and other related binary oxides), however, seems promising for the successful integration of ferroelectrics onto commercial semiconductors (Section 4.2.5).

More exotic devices based on ferroelectrics have also been proposed. While monodomain ferroelectric layers are more desirable for the devices described above, the observation of

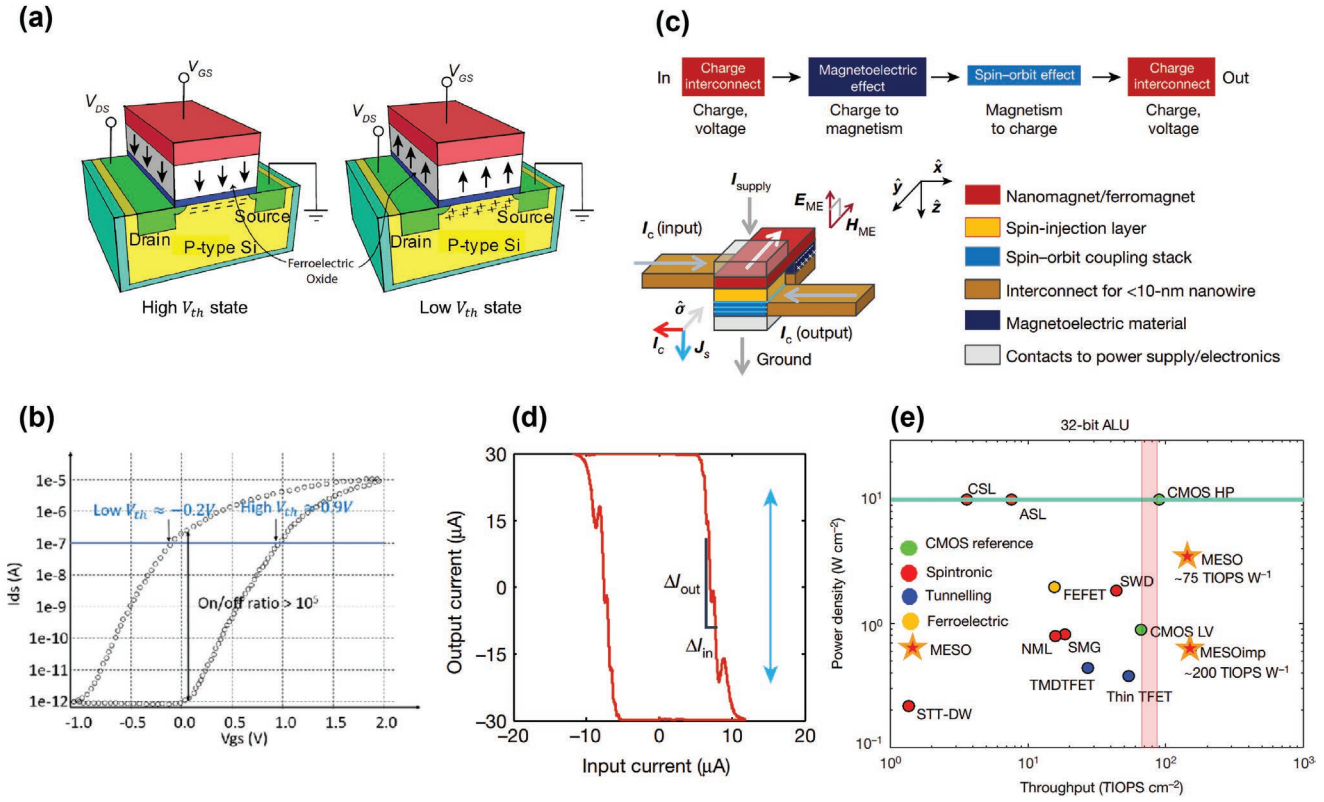

Figure 12. a) FeFET structure and its ON/OFF state. b) *I–V* curves of the device shown in the FeFET structure. a,b) Reproduced under the terms of the CC-BY Creative Commons Attribution 4.0 International license (https://creativecommons.org/licenses/by/4.0).[396] Copyright 2019, The Authors, published by IEEE. c) Top) Transduction of state variables for a cascadable charge-input and charge-output logic device. The magnetoelectric effect transduces the input information to magnetism, and the spin–orbit effect in a topological material transduces the magnetic state variable back to charge. Bottom) MESO device formed with a magnetoelectric capacitor and a topological material. The device comprises a spin-injection layer for spin injection from the ferromagnet to the topological material, an interconnect made of a conductive material, and contacts to the power supply and ground. The logical state of the charge input (current in the +*x*-direction) is inverted by the operation shown to charge output (current in the –*x*-direction). Power for energy gain is injected from the power supply (arrows). The white arrow represents the magnetization direction of the ferromagnet. The gray arrows represent electric currents at the input and output, power supply, and ground. Injection of the power supply current allows for energy gain, large signal gain, and the ability to drive larger output devices. d) Spin–orbit transfer function, showing conversion of a state to charge output. The response of the device is indicated for small signal gain (black line) and the full signal range (–15 to 15 μA; blue arrow). e) Power per unit area versus throughput (that is, number of 32 bit arithmetic logic unit (ALU) operations per unit time and unit area, in units of tera-integer operations per second; TIOPS) for CMOS and beyond-CMOS devices. c–e) Reproduced with permission.[393] Copyright 2019, Springer Nature.

domain-wall conduction in a number of ferroelectric systems including $BiFeO_3$,[81,101,403] $PbZr_xTi_{1-x}O_3$,[83] and $LiNbO_3$[404] (Section 3.4) has driven interest in using the domain wall itself (rather than the domain) as a functional entity. The presence or absence of a domain wall within a ferroelectric capacitor can create a low- (on) or high-resistance (off) state. Moreover, it opens the possibility for multistate architectures, where the number of domain walls written into the device allows for multiple, distinct resistance states.[81] Importantly, compared to more common ferroelectric devices, the state can be read in a nondestructive manner.[405] Further, the individual memory units can be incorporated in commercially established crossbar array architectures to create promising ultrahigh-density, low-power data-storage circuitry.[406] Further work is needed, however, to address limitations of domain-wall devices. Material challenges including increasing the on/off ratio from current values of $\approx 10^3$ and increasing domain-wall currents to microampere levels must be addressed. Additionally, device-specific questions remain, requiring appropriate protocols for write and read operations within the walls, increased operational speeds, and fatigue endurance among others, will require further efforts to enable future devices.[405,407,408]

Finally, enabling electric-field control of alternative order parameters can be achieved through coupling to ferroelectric polarization. The coupling of ferroelectric order with (anti) ferromagnetic order in multiferroic ferroelectrics like $BiFeO_3$ leads to magnetoelectric switching. Magnetoelectric switching is expected to be an energy-efficient mechanism for logic operations with the intrinsic switching energy $E = 2 \times P_s \times V_c$, where P_s is the switched polarization and V_c is the critical voltage for switching. Further, magnetoelectricity can be combined with other physical phenomena (e.g., spin–orbit transduction where the angular momentum of an electron is coupled with its linear counterpart) to form new kinds of beyond-CMOS logic, such as the magnetoelectric spin–orbit devices (MESO) (Figure 12c).[409] The core of a MESO device consists of a magnetoelectric switching capacitor and a spin-to-charge conversion module based on topological or high-spin–orbit-coupling (SOC) materials. When an input signal driven by charge/voltage is triggered, an electric field will be established in the magnetoelectric capacitor, converting charge to magnetism. The generated magnetic field will switch the magnet, which will then trigger spin-to-charge transduction via the SOC materials, converting magnetism back into charge. Following this, an output current will be generated with an inverted direction (Figure 12d). The MESO logic device, it is proposed, can also be scaled down to small sizes (the current goal being 10 nm) and be operated with low switching voltages (≈100 mV) and switching energies (≈1 aJ per bit), thereby gaining its superiority over other leading beyond-CMOS and highly scaled advanced CMOS devices for high-density operations and modern high-throughput computing (Figure 12e).[409]

5.3. Tunable-Microwave Dielectrics

The development of modern thin-film versions of ferroelectrics was largely motivated by the needs of memory applications, but ferroelectrics have several other potentially important roles to play in modern electronics beyond just memory. Ferroelectrics such as $BaTiO_3$ have been used commercially as multilayer ceramic capacitors (within 100–300 MHz frequency range) and embedded capacitors (up to 3 GHz) in integrated circuits due to their large capacitance values and operational voltages. With the semiconductor industry advancing toward transistors operating with oscillation frequencies in the gigahertz regime, there is an increasing demand for materials which can exhibit high dielectric constant, tunability, and low loss, drive-power consumption above 10–20 GHz.[410] Both ferroelectric and paraelectric phases (the latter being historically preferred due to the lack of hysteretic losses) can be used in such tunable microwave devices, making them suitable for integration in telecommunication devices such as phase shifters, antennas, resonators, etc., especially in the gigahertz frequency regime. Some initial work focused on quantum paraelectrics (e.g., $SrTiO_3$, $KTaO_3$, $CaTiO_3$), but these materials require cryogenic temperatures to attain reasonable tunability. The idea of using alloyed versions of ferroelectrics (paraelectrics), especially $Ba_xSr_{1-x}TiO_3$, proved to be a better choice for industrial devices at room temperature. One of the major challenges for such ferroelectric-derived phases, however, is the temperature dependence of the dielectric permittivity.

Through advanced epitaxy-enabled tools like defects,[411] strain,[412] compositional grading,[163] and artificially layered heterostructures, researchers are able to transcend the intrinsic limits to a material's dielectric properties. New paradigm-breaking observations, however, are rewriting what we thought we knew about these materials. For example, large tunability through enhancement in dielectric susceptibility due to the coexistence of multiple domain variants has been realized in $Ba_{0.8}Sr_{0.2}TiO_3$ thin films using a biaxial strain imparted through the substrate.[412] These films also exhibited low dielectric loss, a parameter generally higher in magnitude for systems with large tunability, thus overcoming the traditional concern associated with the use of ferroelectric (as opposed to paraelectric) materials such that the use of domain engineering could open new doors for microwave dielectrics (**Figure 13**a). In other seminal work, attempts to create isotropic free-energy-polarization landscapes (in $Ba_xSr_{1-x}TiO_3$) and mitigate defect contributions to dielectric loss led researchers to low-loss $Sr_{n+1}Ti_nO_{3n+1}$ phases, based on the Ruddlesden–Popper structure wherein n corresponds to the number of perovskite layers of $SrTiO_3$ sandwiched between rock-salt $(SrO)_2$ layers, which were explored as epitaxially strained thin films.[413] For phases with $n \geq 3$, the application of a biaxial strain through the substrate led to the emergence of a local ferroelectric instability in the perovskite layers. Additionally, along with periodic horizontal $(SrO)_2$ planes, aperiodic vertical $(SrO)_2$ planes were observed in the strained heterostructures, which served to segregate defects. The resulting (nearly) dispersionless dielectric response over the radiofrequency and microwave range accompanied with low loss achieved a figure-of-merit (50 at 10 GHz) higher than that in the prototypical tunable dielectric $Ba_xSr_{1-x}TiO_3$ (<10 at 10 GHz) (Figure 13b). Beyond traditional perovskite-based oxides, improper ferroelectrics (Section 4.2.4), known for their unique mechanism for ferroelectricity, do not obey the traditional Curie–Weiss law and are likely to exhibit a dielectric susceptibility with a weak electric-field dependence essential

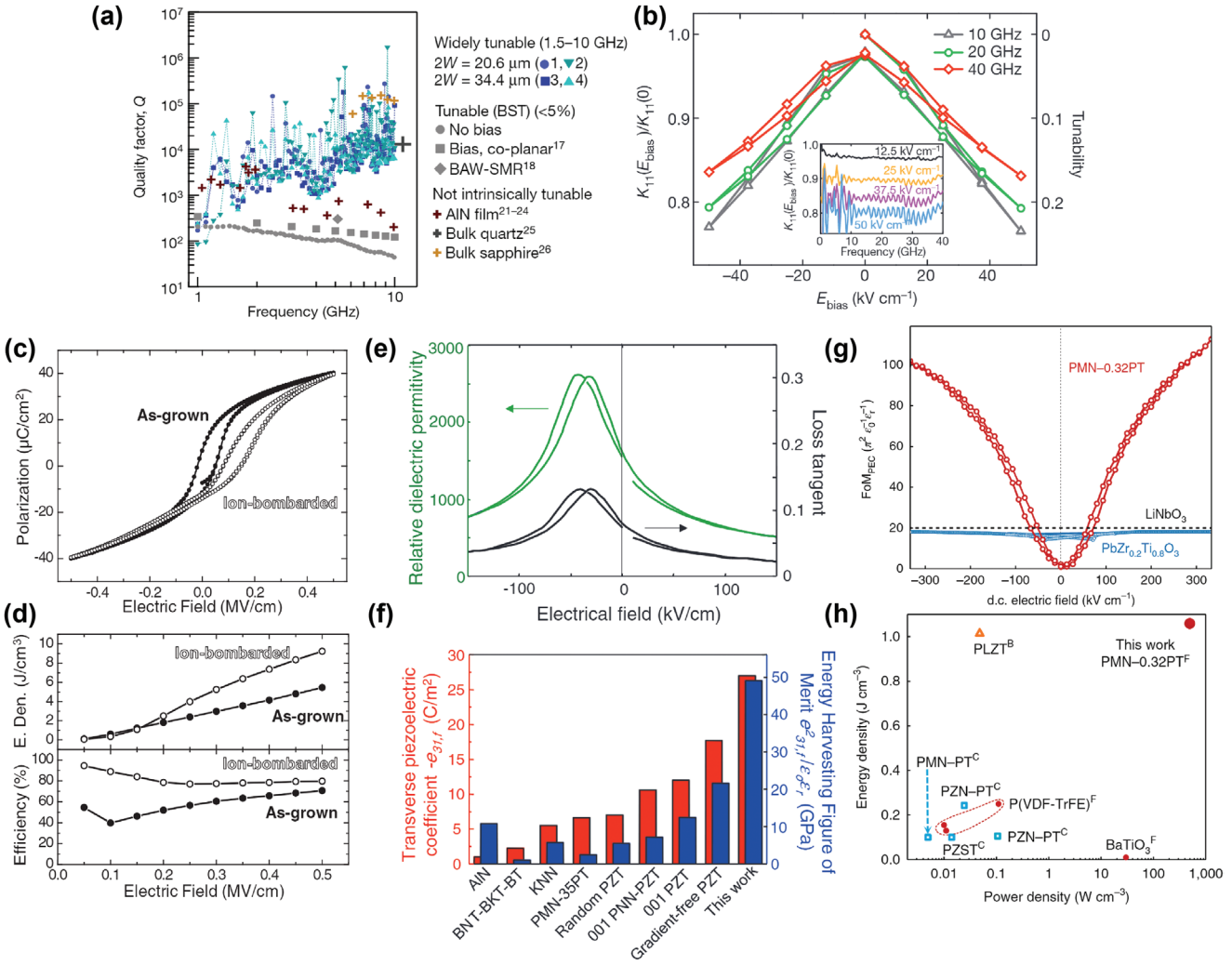

Figure 13. a) Peak Q values were collected at 100 frequencies in four distinct devices for $Ba_{0.8}Sr_{0.2}TiO_3$ (BST) films. The data show an increase of more than one order of magnitude over approximately one frequency decade, deviating strongly from the usual f^{-1} scaling law. Shown for comparison are the highest values reported for piezoelectric resonators made of bulk single-crystal quartz, sapphire, and AlN film, none of which is intrinsically tunable (each point represents an individual device), and values reported for intrinsically tunable BST films, including a bulk acoustic-wave solidly mounted resonator (BAW-SMR) film. Reproduced with permission.[412] Copyright 2018, Springer Nature. b) The ratio of K_{11} under an applied bias field (E_{bias}) to that at zero bias field (left-hand axis) and tunability (right-hand axis) of the $n = 6$ sample of $Sr_{n+1}Ti_nO_{3n+1}$ ($n = 2$–6) films deposited on $DyScO_3$(110) at different frequencies in the microwave range. The inset shows the dielectric constant ratio as a function of frequency at different applied biases. Reproduced with permission.[413] Copyright 2013, Springer Nature. c,d) Hysteresis loops out to $E = 0.5$ MV cm^{-1} measured at 10 kHz for the as-grown and ion-bombarded 0.68 $PbMg_{1/3}Nb_{2/3}O_3$–0.32$PbTiO_3$/$Ba_{0.5}Sr_{0.5}RuO_3$/$NdScO_3$(110) thin-film heterostructures. Energy density (J cm^{-3}) and efficiency (%) calculated from the obtained unipolar hysteresis loops for the as-grown and ion-bombarded heterostructures. c,d) Reproduced with permission.[416] Copyright 2020, American Association for the Advancement of Science. e,f) Dielectric and piezoelectric properties of the $PbMg_{1/3}Nb_{2/3}O_3$–$PbTiO_3$ film on Si substrate. Dielectric permittivity versus electric field measurement at 1 kHz with a 30 mV_{rms} (rms, root mean square) oscillating voltage. Comparison of figure-of-merit for micromachined actuators and energy harvesters of $PbMg_{1/3}Nb_{2/3}O_3$–$PbTiO_3$ films with other reported values. e,f) Reproduced with permission.[221] Copyright 2011, American Association for the Advancement of Science. g,h) Pyroelectric properties of 0.68$Pb(Mg_{1/3}Nb_{2/3})O_3$–0.32$PbTiO_3$ thin films under 0.5% compressive strain. FoM_{PEC} as a function of applied DC electric field. The measured FoM_{PEC} for a $PbZr_{0.2}Ti_{0.8}O_3$ thin film (blue) and literature values for $LiNbO_3$ (black dashed line) are provided for comparison. Comparison with experimentally achieved energy and power densities from a number of prior studies of pyroelectric energy conversion using thermodynamic cycles. The superscripts B, C, and F correspond to bulk-ceramic, single-crystal, and thin-film samples, respectively. g,h) Reproduced with permission.[451] Copyright 2018, The Authors, published by Springer Nature.

for high tunability.[414] Such examples are likely to motivate newer design approaches and material systems like relaxors to be explored via epitaxy for decoupling the mutually interdependent parameters like dielectric constant, loss, tunability, and temperature dependence.

5.4. Energy Harvesting, Conversion, and Storage

Ferroelectric thin films have also found applications in the fields of energy harvesting, conversion, and storage based, in large part, on the inherent interrelationships between electrical,

mechanical, and thermal properties of solids. Recalling that every ferroelectric is also a piezoelectric and pyroelectric material (often with large responses due to the large intrinsic polarization) allows ferroelectrics to be of great utility in multiple applications (**Figure 14**).

5.4.1. Capacitive-Energy Storage

With the growing need for storing electrical energy, a number of energy-storage devices have evolved over the years with their own set of advantages and disadvantages. While fuel cells (≈1000 W h kg^{-1}) and batteries (≈300 W h kg^{-1}) tend to offer high energy-density values, their charge–discharge cycles tend to be long due to the slow movement of charge carriers causing a low power density (<500 W kg^{-1}). Electrochemical capacitors, on the other hand, do provide moderate power density (≈100 W kg^{-1}) at moderate energy density (≈30 W h kg^{-1}), their charge–discharge process still requires a few seconds or more. Nonlinear dielectric capacitors, however, are capable of power density as high as 10^8 W kg^{-1} owing to their extremely high discharge speed (milliseconds), making them ideal for pulsed power electronics. Among the nonlinear dielectrics, (anti)ferroelectrics and relaxors are gaining attention in the community owing to their large magnitude of spontaneous polarization. The critical parameters involved are the electric breakdown strength (E_{max}), recoverable energy density (W_{rev}), energy storage efficiency (η), fatigue endurance, and thermal stability. While ferroelectric thin films can be modified by chemical substitution or as multilayered heterostructures to enhance their energy-storage performance, antiferroelectric[415] and relaxor-based[276,277,416] thin films have proven to be more efficient candidates. Antiferroelectrics have the inherent advantage of demonstrating a high W_{rev} with a double hysteresis loop (unlike ferroelectrics) due to the electric-field-induced antiferroelectric-to-ferroelectric phase transition. The most

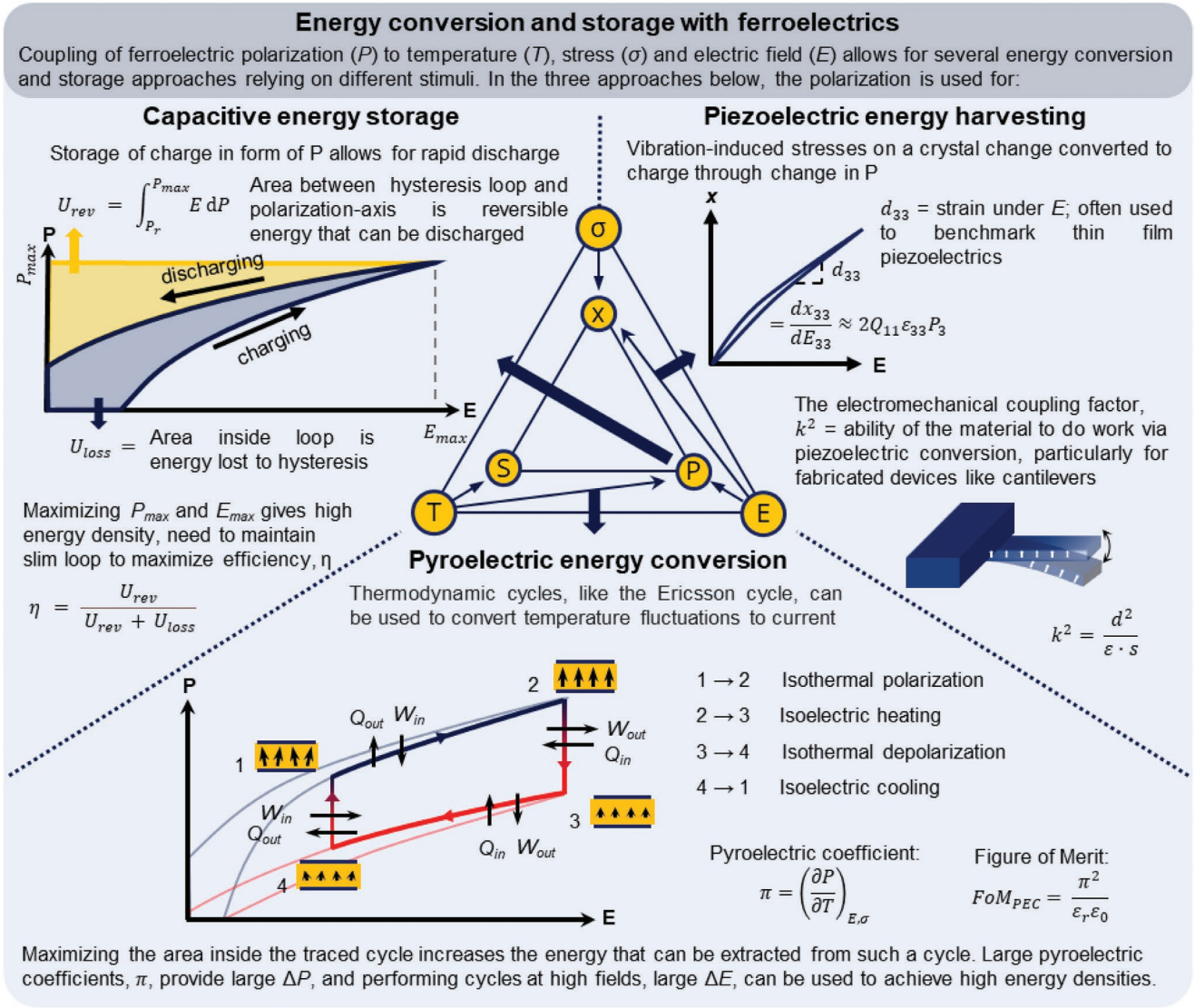

Figure 14. Energy conversion and storage with ferroelectrics.

studied material systems have been limited to pure and modified forms of $PbZrO_3$,[417] $PbHfO_3$,[415,418] $Pb_{1-x}La_xZr_yTi_{1-y}O_3$,[419] and doped HfO_2[420] with the major challenge being attaining simultaneous enhancement in W_{rev} and η.[421,422] Relaxor ferroelectrics,[423,424] on the other hand, have gained popularity due to the minimal hysteresis in their nonlinear polarization response and high polarization, a combination ideal for high W_{rev} and η. Traditionally, studies have focused on modifying the polarization response in oxide thin films using compositional or interfacial routes, but the growing understanding of ex situ defects introduced through high-energy helium-ion bombardment (Section 3.4) has provided new approaches. Recent results on ion-bombarded $0.68PbMg_{1/3}Nb_{2/3}O_3$–$0.32PbTiO_3$ thin films demonstrated that ion bombardment allowed for simultaneous reduction of leakage current and enhancement of high field polarizability and breakdown field (Figure 13c,d) such that large energy-storage density (133 J cm^{-3}), high efficiency (>75%), good reliability (>10^8 cycles), and temperature stability (−100 to 200 °C) were achieved.[416] In other work, researchers inspired by polar disorder of relaxor ferroelectrics (Section 4.1) synthesized $BiFeO_3$–$BaTiO_3$–$SrTiO_3$ solid solutions as thin films to engineer similar polar disorder and realize a flattened domain-switching pathway resulting in low hysteresis loss accompanied with high saturation polarization. The resulting high energy-storage density (112 J cm^{-3}), high efficiency (80%), good reliability (>10^8 cycles), and temperature stability (−100 to 150 °C).[276] As such, these examples illustrate how the understanding and capabilities of thin-film epitaxy provide multiple pathways to enhance the energy-storage performance in different polar materials.

5.4.2. Piezoelectric-Energy Harvesting

Recent advances in microelectromechanical systems (MEMSs) such as microsensors and microactuators combined with the possibility of harvesting electrical energy from ambient (mechanical) sources,[425–428] have introduced new ways to generate sustainable energy using piezoelectric materials. Typical piezoelectric systems include perovskite ferroelectrics $BaTiO_3$ and $PbZr_xTi_{1-x}O_3$, as well as wurtzite structures ZnO and AlN, with $PbZr_{1-x}Ti_xO_3$ of primary interest for applications due to its relatively large piezoelectric coefficient and in turn large electromechanical coupling factor, k which serves as a figure-of-merit for mechanical energy harvesting with piezoelectric cantilevers (Figure 14). On the other hand, single crystals of relaxor ferroelectrics, particularly $(1-x)PbMg_{1/3}Nb_{2/3}O_3$–$(x)PbTiO_3$[265] have large piezoelectric coefficients due to the large strains associated with rotation of polarization (Section 4.1). For successful integration with standard MEMS fabrication routes, however, deposition on silicon is preferred. As such, there has been a significant effort in the last few decades to grow epitaxial piezoelectric thin films on silicon substrates (Section 3.5) in hopes of achieving higher piezoelectric performance than can be obtained in polycrystalline films.[221,429,430] For example, epitaxial $0.67PbMg_{1/3}Nb_{2/3}O_3$–$0.33PbTiO_3$ thin films synthesized on $SrTiO_3$-buffered Si substrates using sputtering were reported to have a large transverse piezoelectric coefficient (e_{31}) comparable to that for $0.67PbMg_{1/3}Nb_{2/3}O_3$–$0.33PbTiO_3$ single crystals (Figure 13e,f).[221] With the control provided by advanced thin-film synthesis, and the understanding of the importance of structural disorder, a recent study utilized Na deficiency in $NaNbO_3$ which resulted in vertical nanopillars embedded in a perovskite matrix with highly defective interfaces. These $Na_{1-\delta}NbO_3$ films ultimately were reported to have a d_{33} = 1098 pm V^{-1},[431] outperforming many known ferroelectric candidates. Similar design criteria can be extended to well-established material systems as well to enhance their piezoelectric coefficients further. One limiting factor to researching piezoelectricity in thin films is the difficulty in accurately measuring small displacements associated with thin-film piezoresponse. Several techniques have been developed with varying resolutions, including single- and double-beam laser interferometry (0.1–1 pm), scanning laser doppler vibrometry (1 pm), photonic sensors (400 pm), piezoresponse force microscopy (1 pm), and scanning tunneling microscopy (5 pm).[432] While such approaches have been used on occasion, a fail–safe measurement of piezoelectric responses in all thin-film geometries remains to be developed; such an advance could greatly extend the potential of such applications.

Another particularly detrimental aspect of thin-film piezoelectrics, in particular, is the clamping by the large, piezoelectrically inactive substrates required for thin-film deposition. Novel approaches using freestanding membranes (Section 3.6) are promising, but still in their infancy. More common is the use of micro- and nanofabrication to engineer device architectures which reduce clamping of the piezoelectrically active region of the film. One of the most common approaches is the fabrication of cantilever beams (unimorph or bimorph), wherein a large portion of the film is underetched to release from the substrate, which can be fabricated from either single-crystal or thin-film samples. For example, an output power of 4.16 mW has been reported for $0.71PbMg_{1/3}Nb_{2/3}O_3$–$0.29PbTiO_3$ single crystals fabricated into cantilevers.[433] The operational frequency, however, is limited to relatively high frequencies, and efficiency rapidly decreases at off-resonance frequencies. The effect of substrate-induced clamping has also been suppressed by lateral scaling, or in other words, removing the piezoelectrically inactive region of thin films surrounding the active region, creating single capacitors that are isolated islands. By fabricating discrete 1 μm^2 islands from epitaxial $PbZr_{0.2}Ti_{0.8}O_3$ films, researchers showed increased polarization and piezoelectric responses, which were ultimately attributed to enhanced contributions from ferroelastic 90° domain motion.[434] Other studies show that increasing the aspect ratio of isolated capacitors of highly textured $0.70PbMg_{1/3}Nb_{2/3}O_3$–$0.30PbTiO_3$ films resulted in increased domain mobility and intrinsic dielectric response, ultimately resulting in large piezoelectric coefficients.[434–436] Other studies have focused on depositing polycrystalline films on flexible substrates, for example, sol–gel-deposited $PbZr_{0.52}Ti_{0.48}O_3$ films on poly(ethylene terephthalate) (PET) substrates, which resulted in output powers of 2.2 mW, or ZnO-based nanowire arrays which produced output power densities of 2.7 mW cm^{-3}).[437,438] Along with energy harvesting for self-powered applications,[439–442] there has been a constant drive toward developing MEMS devices for sensing and actuating applications with smaller sizes, increased integration density, higher speed, and larger range of mechanical displacement.

Currently, most devices incorporate actuation through passive mechanical elements driven by electrostatic field. Incorporation of piezoelectric thin films directly into the device structure, however, enables direct coupling between the mechanical deformation and the internal electric field, resulting in low power consumption while combining sensing and actuation in one device. Additionally, piezoelectric MEMS devices demonstrate higher energy density values while enabling high frequency and temperature-stable resonant devices as compared to the electrostatic actuators.[429,430] Considering most high-performing piezoelectric material systems are also ferroelectric, the piezoelectric community has benefitted immensely by the infrastructure developments resulting from ferroelectric memories.[435–438]

5.4.3. Pyroelectric and Electrocaloric Applications

One fundamental property of ferroelectrics, namely the temperature-dependent polarization provides a unique method for utilizing ferroelectrics in the conversion of temperature variations into current. More specifically, the pyroelectric effect is defined as the change in the polarization (P) as a function of temperature (T) and is characterized by the pyroelectric coefficient, $\pi = (\partial P/\partial T)_E$. Conversely, the electrocaloric effect involves the isothermal entropy (S) or adiabatic temperature change associated with alignment of polar dipoles under and applied electric field (E), and is characterized by the electrocaloric coefficient, $\Sigma = (\partial S/\partial E)_T$. This coupling of polarization and temperature can be leveraged to harvest waste heat to generate clean electrical energy (via pyroelectric energy conversion) and for environment-friendly solid-state cooling (via the electrocaloric effect).[440] Incorporating them in thin-film devices provides added advantages like enhanced susceptibilities and low thermal mass, while also enabling the use of all the epitaxy-based tools discussed in this review to enhance a material's pyroelectric response.[443–445] Despite these advantages, the study of pyroelectric and electrocaloric effects in thin films presents significant challenges, requiring advanced capabilities in synthesis, characterization, and material modeling.

Of particular importance for engineering large responses is quantifying the various contributions to the pyroelectric and electrocaloric effects. The total pyroelectric response can be defined as

$$\pi_{\text{total}} = \pi_{\text{primary}} + \pi_{\text{secondary}} + \pi_{\varepsilon} + \pi_{\text{tertiary}} \tag{1}$$

$$\pi_{\text{total}} = \phi\left(\frac{\partial P}{\partial T}\right)_x + P\left(\frac{\partial \phi}{\partial T}\right)_x + \left(\frac{\partial P}{\partial X}\right)_T \left(\frac{\partial X}{\partial x}\right)_T \left(\frac{\partial x}{\partial T}\right)_X + \varepsilon_0 E\left(\frac{\partial \varepsilon_r(E)}{\partial T}\right) + \pi_{\text{tertiary}} \tag{2}$$

where ϕ is the fraction of ferroelectric domains contributing to the pyroelectric response, x is the strain, ε_0 is the permittivity of free space, and ε_r is the relative dielectric permittivity. π_{primary} is a combination of both intrinsic $\left(\phi\left(\frac{\partial P}{\partial T}\right)_x\right)$ and extrinsic $\left(P\left(\frac{\partial \phi}{\partial T}\right)_x\right)$ effects. The intrinsic contribution arises from the temperature dependence of polarization within the ferroelectric domains and the extrinsic contribution arises from thermally induced changes in the overall domain structure (fractions). $\pi_{\text{secondary}}$ accounts for temperature-induced changes in polarization due to the piezoelectric effects (change in unit-cell volume). π_{ε} arises from the temperature and electric-field dependence of ε_r. Finally, π_{tertiary} arises from nonuniform stresses induced by the piezoelectric effect from inhomogeneous heating (and is often considered to be negligible in thin films). For electrocaloric measurements, the low thermal mass of thin films with respect to the substrate makes direct measurements of the temperature changes in adiabatic conditions particularly difficult. In lieu of direct approaches, measurement of $((\partial P/\partial T)_E)$ followed by application of the appropriate Maxwell relations $((\partial P/\partial T)_E = (\partial S/\partial E)_T)$ to obtain the associated changes in temperature and entropy, allows for indirect estimation of the isothermal dipolar entropy change (ΔS_{iso}) and the adiabatic temperature change (ΔT_{ad}) as

$$\Delta S_{\text{iso}} = \int_{E_1}^{E_2} \left(\frac{\partial P}{\partial T}\right)_E \mathrm{d}E \tag{3}$$

$$\Delta T_{\text{ad}} = -\int_{E_1}^{E_2} \left(\frac{T}{C(T,E)}\right)\left(\frac{\partial P}{\partial T}\right)_E \mathrm{d}E \tag{4}$$

where, $C(T,E)$ is the volumetric heat capacity.[446] To achieve accurate results with such indirect methods, however, requires careful consideration of the appropriate mechanical boundary conditions, as clamping by the substrate breaks the thermodynamic equivalence of Σ and π. Recently, development of microfabricated device structures has allowed for direct measurement of pyroelectric and electrocaloric effects in thin films.[446] In direct pyroelectric measurements, $\partial P/\partial T$ is measured via phase-sensitive detection of the pyroelectric current (i_P) in response to an applied temperature oscillation. For direct electrocaloric measurements, an AC electric field can be applied across the ferroelectric capacitor, and the resulting temperature change of a microfabricated thermometer can be measured using a modified 3-omega methods typically used for measurements of thermal conductivity in thin films, which then can be used to extract Σ and the average change in temperature in the ferroelectric (using analytical heat transport models). Equipped with the appropriate measurement techniques, researchers have been utilizing thin-film epitaxy to study and enhance the various contributions and approaches for enhancing pyroelectric and electrocaloric effects.

Initial questions regarding pyroelectric responses in thin films were centered on the role of domain structure and how the various contributions (e.g., primary, secondary, tertiary) could be impacted. Early studies combining GLD simulations and experimental measurements of $PbZr_{0.2}Ti_{0.8}O_3$ films under various strain states suggested large contributions from extrinsic effects in c/a domain structures, which can also give rise to enhanced dielectric and pyroelectric responses compared to single phase c or a_1/a_2 counterparts.[98,100] Moreover, it was found that secondary contributions, that is, those arising from piezoelectrically induced changes to polarization due to a thermal-expansion mismatch between the film and substrate,

could account for up to 50% of the room-temperature total pyroelectric response.[447] As phase-sensitive measurements became more mature, further studies on strained $PbZr_{0.2}Ti_{0.8}O_3$ films with complex mixed-phase domain structures were used to distinguish extrinsic contributions using a reference film of monodomain purely *c*-oriented film. Interestingly, this study demonstrated that extrinsic ferroelastic domain interconversion counteracted the total pyroelectric response in compressively strained films, while increased the total response in films under tensile strain, ultimately indicating that the sign of the extrinsic contribution was different depending on the strain state and nature of the domain structure.[448] Using high frequency and high DC bias voltages to turn on and off various responses, researchers were further able to systematically and individually quantify intrinsic, extrinsic, dielectric, and secondary contributions in compositions across the $PbZr_{1-x}Ti_xO_3$ MPB without the need for a monodomain reference.[449] While much of this work has used the well-understood $PbZr_{1-x}Ti_xO_3$ system as a model system, it has laid the groundwork for expanding these methodologies to any number of new pyroelectric materials.

As with piezoelectric responses, traditional approaches to enhancing pyroelectric responses involve perching materials near temperature- or chemistry-driven phase transitions to enhance the magnitude of the pyroelectric or electrocaloric changes. As discussed above, extrinsic contributions do not always enhance pyroelectric responses, as can be seen in measurements of $PbZr_{0.52}Ti_{0.48}O_3$, which sits at the MPB, where the large dielectric response counteracts the moderate intrinsic response. As such, other methods for engineering novel structures have been explored. For example, utilizing films with a compositional gradient (Section 3.3.2) from $PbZr_{0.2}Ti_{0.8}O_3$ to $PbZr_{0.8}Ti_{0.2}O_3$ leveraged the built-in field associated with the polarization gradient to reduce the dielectric response while maintaining large intrinsic responses.[450] Recently, studies on $0.68Pb(Mg_{1/3}Nb_{2/3})O_3$–$0.32PbTiO_3$ thin films found that despite small pyroelectric responses at zero field, applying a background DC bias simultaneously produced a large pyroelectric coefficient and suppressed the dielectric contribution. These films, which possessed remarkable figures-of-merit, were used to perform pyroelectric energy conversion cycles, ultimately producing the highest reported energy density (1.06 J cm^{-3}), power density (526 W cm^{-3}), and efficiency (19%) as compared to traditional ferroelectrics (Figure 13g,h).[451]

On the other hand, electrocaloric measurements in thin films are relatively less common. Measuring temperature changes in small volumes of material is challenging and thus makes direct measurements of the electrocaloric effect particularly difficult, and indirect measurements tend to produce inaccurate or unrealistic values. Yet, there are exciting opportunities for using thin films in electrocaloric devices, with the promise of on-chip, solid-state cooling, as well as novel methods of engineering large electrocaloric responses by leveraging direct measurement techniques. For example, extrinsic contributions were found to enhance electrocaloric effects in $PbZr_{0.2}Ti_{0.8}O_3$ films in the same fashion as that observed for pyroelectric responses.[448] The critical role of entropy in the electrocaloric effect further suggests pathways toward engineering large responses. For example, electrocaloric measurements in ferroelectric $Hf_{1-x}Si_xO_2$ thin films, where defect dipoles were found to contribute to a wake-up behavior in the pyroelectric response, also demonstrated electrocaloric coefficients 4 times larger than the corresponding pyroelectric coefficients, suggesting that disordering of defect dipole could serve as a method for creating additional entropy.[452] These examples only serve as preliminary motivation of the potential for engineering and understanding large electrocaloric responses in thin films enabled by advances in direct measurement methodologies.

6. Outlook: Where Do We Go from Here?

The year 2020 marked the 100-year anniversary of the discovery of ferroelectricity. The field has come a long way in this time and, as we stand looking at the first decade of the second 100 years of ferroelectricity, there is much to be excited about. As has hopefully been demonstrated, the field of thin-film ferroelectrics has been and remains vibrant. As we look to the future, it appears clear that ferroelectric films will continue to be widely studied both from the fundamental, basic science point of view and from an applied, applications point of view. From continued work on the discovery of novel materials to ways to push the limits of material function to the realization of a new generation of devices based on these materials, the near-term future will explore the limits of functionality, integration, and beyond.

6.1. New Materials, New Possibilities

Despite 100 years of research on ferroelectrics, most research and nearly all applications are based on just a handful of materials. While recent attention on binary-oxide ferroelectrics and 2D systems seems poised to open new possible directions, researchers continue to ask the question of what else is out there. As noted above (Section 4.3), there is a growing push to accelerate the discovery of new polar and ferroelectric materials. The next decade is likely to see growing utilization of high-throughput workflows and target searches through known-material databases in hopes of finding a proverbial "diamond in the rough" in the form of a new ferroelectric material. But more than this, it is likely that the coming decade will show a marriage between state-of-the-art computation (in particular approaches augmented by machine learning and artificial intelligence), real-time synthesis control, and advanced characterization in a closed-loop cycle that will enable rapid design and control of designer material function. This may not mean the identification of totally "new" materials, but the thoughtful manipulation of known materials to coax out new properties. The potential for such closed-cycle approaches to dramatically impact in different applications spaces remains to be realized, but represents the ultimate culmination of many fields in this space.

6.2. Exotic Dipolar Textures and Emergent Phenomena

As was introduced (Section 3.2.3), the observation of polar vortices and skyrmions has piqued the interest of researchers

around the globe—the search of exotic dipolar textures is now well underway. Researchers are working to develop better ways to synthesize and control the artificial heterostructures required to produce this order and to probe, understand, classify, and, ultimately, use these exotic states of matter. This is a field that will require the cooperative development of multiscale modeling approaches, advanced materials synthesis, and state-of-the-art characterization to enable advances. Ultimately, the community does not fully know all the possible variations of topological states built from polar order that can be obtained—the coming years are sure to provide several new observations and surprises in this regard. While these searches will primarily focus on real-space textures, the potential to identify momentum-space (or electronic structure) features in polar, ferroelectric materials that give rise to exotic phenomena is also a field with great potential. For example, topological insulators, which have different band topologies compared with those of conventional insulators such that interfaces between topological and conventional insulators must always be conductive, are being explored in conjunction with ferroelectrics. The unique characteristics of topological insulators mean that they might have intriguing and synergistic interactions with ferroelectrics, because ferroelectric nanomaterials require conductive surfaces to compensate their bound charge and reduce the depolarizing field. Recent work,[453] for example, suggests that under pressure, $CsPbI_3$ could exhibit a transition to a topological insulating phase and to a switchable ferroelectric phase. Studies on such dipolar textures and the associated behavior in complex ferroelectric heterostructures not only has advanced the understanding of the physics of ferroelectricity, but also has directed the community to newer dimensions in terms of device architectures. Deriving inspiration from analogies in the magnetic systems, the real space topologies such as vortices and skyrmions in ferroelectric heterostructures can lead to a new paradigm in memory storage where the information bits are encoded in the form of the chirality of the vortex/skyrmion. Additionally, the negative capacitance embedded within the core of the vortex and skyrmion textures can be instrumental in designing NC-FETs (Section 5.2). While magnetic textures are manipulated using a cross-coupling between electric and magnetic fields, chirality in ferroelectric textures is expected to be easier to switch with electric field, reducing overall power consumption. Practical realization of these functionalities, however, requires more in-depth studies of proposed device architectures as well as methods for switching the chirality in order to perform read/write operations in real devices.[454–457]

At the same time, there is growing interest in materials exhibiting the so-called persistent spin texture (PST). This is part of growing interest in materials where quantum effects imposed through crystal symmetry lead to novel physical properties for spintronic applications. Additionally, though large spin–orbit-coupling is useful for such applications, it turns out to be detrimental for the spin lifetime. Traditionally, spin–orbit field is dependent on the momentum, which causes impurities and defects to scatter electrons by changing their momentum and spin orientation, resulting in a shortened spin lifetime. PST, however, enables momentum-independent unidirectional spin orientation (texture) at the band edges facilitating infinite spin lifetime. PST has been observed for semiconductor quantum-well structures (GaAs/AlGaAs[458]) experimentally; however, such structures require fine control of the quantum well width. There is an interest, however, to study PST as a material's intrinsic property (i.e., symmetry-protected PST), as has been predicted to occur when a nonsymmorphic symmetry operation (e.g., glide symmetry operation with a mirror plane and translation) commutes with the spin–orbit field in a noncentrosymmetric material. Ferroelectrics, by virtue of their noncentrosymmetric crystal symmetry have the potential to exhibit such spin textures. Further, PST can be coupled to the spontaneous polarization and thus manipulated by its orientation and magnitude.[459] Based on theoretical calculations, materials like $BiInO_3$ and various $A_3B_2O_7$ have been put forth as potential candidates.[364,460,461] The challenge, however, is to make these insulating oxides electrically (semi)conducting with suitable chemical doping to characterize the spin texture. Such studies can further explore the coupling between spin, orbital, and lattice degrees of freedoms in ferroelectrics, leading to nonvolatile spintronic devices like a spin-field-effect transistor.

6.3. Beyond CMOS, Internet of Things, and Energy-Efficient Computing

As noted above, ferroelectrics are strong candidates to find a place in next-generation applications in memory and logic operation. The question remains, however, as to what materials and in what form this will be achieved. The coming decade is sure to be critical in the articulation of a realistic pathway to scalable devices in this space based on ferroelectric thin films. Binary systems like the HfO_2-based materials have good potential, should the community be able to better understand the mechanisms underlying polarization switching, wake-up, and related phenomena and address the added challenge that the coercive voltages are very large. At the same time, continued work on creating ideal versions of these (and other) ferroelectric materials will likely help push down switching energies and voltages, and attention to synthesis will enable deterministic control of structure and interfaces and computational approaches will provide insights on how to tune switching phenomena and open the doors to achieve the desired functions in these materials. Of particular importance will be the development of pathways to deterministically manipulate the energy landscape of ferroelectrics—thus tuning switching energies, pathways, and polarization state (perhaps even enabling beyond-binary function). In just the last few years, a marked increase in the interest and demonstration of ferroelectrics in many forms in realistic devices suggests this is going to be a reality and, likely, a busy near-term future for the field.

6.4. Probing the Limits of Ferroelectric Thin Films

Something that goes hand-in-hand with the applications noted above are efforts to probe the limits for ferroelectric function. In essence, to enable the devices and functions we hope to achieve, it is critical that we learn how to extend our already deep understanding of ferroelectrics to the length, time, and energy scales that are important for real applications. In this

regard, the community needs to address the question of how we can produce, process, and study materials at length (both thickness and lateral), time, and energy scales that approach 1–10 nm, <1 ns, and 1–100 aJ, respectively? This calls for advances and concerted efforts in modeling, synthesis, fabrication, and characterization using a diverse range of techniques. Be it operation in a logic device or in 5G (and beyond) communications technologies, there is often a gap between traditional academic research and understanding of the needs of advanced technology. Finding ways to address this gap—melding understanding and questions from both sides—in the research of any class of materials is key for impact. A critical part of this work will be leveraging recent concerted investment in real-time studies of ferroelectrics and their devices. Such studies are already taking advantage of the evolution of modeling and characterization methods that can increasingly provide understanding across huge time and length scales. Key studies of in operando function—watching realistic devices operate under applied stimuli and at the time and length scale of interest—will be required to truly advance the field. For example, advances in hardware and the development of novel transmission electron microscopy methods (including aberration correction and 4D approaches), scanning-probe spectroscopies, and synchrotron-based scattering and spectroscopy methods can now provide unprecedented chemically specific, nano- and atomic-scale insight of ferroelectrics at the timescales at which real processes which are important for device operation happen. This, combined with better data analysis and big-data approaches that are now circulating in the community could provide unprecedented insight on how ferroelectrics work in real systems. The next decade is primed for advances in each of these spaces to be brought together to make lasting impact.

6.5. Arbitrary Heterostructures and Devices and Scaling Ferroelectrics

One of the hanging questions for the future of ferroelectrics is whether they can be made compatible with the devices of tomorrow. Continued work on the integration of oxide ferroelectrics on semiconductors is thus important, but new advances like the liftoff process and pick-and-place approaches stand poised to enable the integration of ferroelectrics and a range of dissimilar materials. Whether it is placing ferroelectrics on demand in CMOS stacks or creating new interfaces and heterostructures with other 2D materials (such as chalcogenides) or even mixing nonclassical nitride-based ferroelectrics with the above, there is a nearly limitless potential for impact and development in this regard. That work could, in turn, lay the foundation for greatly expanding the types of materials used in commercial electronics and open new possibilities for device designers.

7. Conclusions

Functional materials, and ferroelectrics in particular, have been an important class of materials both for fundamental research and for applications for the past 70 years. The complex interplay between multiple degrees of freedom in these materials means that techniques developed to study them have been applied to other condensed matter physics fields with great success (and vice versa). Each year brings new insights and new understanding of these complex materials, as well as new potential applications. In the end, the diverse functionalities of ferroelectrics mean that this complex class of materials will continue to attract interest as their performance in existing devices is improved and novel applications are developed in the years to come. Ultimately, disruptive breakthroughs in high-quality growth, epitaxial nanoscale control and multiscale modeling will provide the ability to create new materials with unprecedented combinations of functional properties. In the long run, the breakthroughs in the field of ferroelectrics will potentially transform society—from energy and medicine, to information and communications.

Acknowledgements

The authors wrote this review on behalf of numerous collaborators and colleagues who have provided critical insights, support, and feedback over the years. Over the years, the team has received support from numerous sources for the development of these techniques and scientific studies, including: the Army Research Office under Grant Nos. W911NF-10-1-048, W911NF-14-1-0104, W911NF-21-1-0118, W911NF-21-1-0126, and the ETHOS MURI via cooperative agreement Grant No. W911NF-21-2-0162; the Army Research Laboratory via the Collaborative for Hierarchical Agile and Responsive Materials (CHARM) under cooperative agreement Grant No. W911NF-19-2-0119; the Intel Corporation via the FEINMAN and COFEEE Programs; the National Science Foundation under Grant Nos. DMR-1149062, DMR-1451219, CMMI-1434147, DMR-1708615, and DMR-2102895; the U.S. Department of Energy, Office of Basic Energy Sciences under Award Nos. DEFG02-07ER46459, DE-SC-0012375, DE-AC02-05-CH11231 (Materials Project Program No. KC23MP), and DE-AC02-05-CH11231 (Codesign of Ultra-Low-Voltage Beyond CMOS Microelectronics (MicroelecLBLRamesh)).

Conflict of Interest

The authors declare no conflict of interest.

Keywords

epitaxy, ferroelectrics, piezoelectrics, pyroelectrics, thin films

Received: November 2, 2021
Revised: March 3, 2022
Published online: June 10, 2022

[1] G. H. Haertling, *J. Am. Ceram. Soc.* **1999**, *82*, 797.
[2] J. T. Cheung, H. Sankur, *Crit. Rev. Solid State Mater. Sci.* **1988**, *15*, 63.
[3] J. Cheung, J. Horwitz, *MRS Bull.* **1992**, *17*, 30.
[4] D. B. Chrisey, G. K. Hubler, *Pulsed Laser Deposition of Thin Films*, Wiley-VCH, Weinheim, Germany **2003**.
[5] H. M. Smith, A. F. Turner, *Appl. Opt.* **1965**, *4*, 147.
[6] D. Dijkkamp, T. Venkatesan, X. D. Wu, S. A. Shaheen, N. Jisrawi, Y. H. Min-Lee, W. L. McLean, M. Croft, *Appl. Phys. Lett.* **1987**, *51*, 619.

[7] X. D. Wu, D. Dijkkamp, S. B. Ogale, A. Inam, E. W. Chase, P. F. Miceli, C. C. Chang, J. M. Tarascon, T. Venkatesan, *Appl. Phys. Lett.* **1987**, *51*, 861.
[8] D. G. Schlom, *APL Mater.* **2015**, *3*, 062403.
[9] A. Y. Cho, J. R. Arthur, *Prog. Solid State Chem.* **1975**, *10*, 157.
[10] A. C. Gossard, P. M. Petroff, W. Weigmann, R. Dingle, A. Savage, *Appl. Phys. Lett.* **1976**, *29*, 323.
[11] R. A. Betts, C. W. Pitt, *Electron. Lett.* **1985**, *21*, 960.
[12] N. Izyumskaya, Y. Alivov, H. Morkoç, *Crit. Rev. Solid State Mater. Sci.* **2009**, *34*, 89.
[13] S. M. George, *Chem. Rev.* **2010**, *110*, 111.
[14] S. S. Cheema, D. Kwon, N. Shanker, R. dos Reis, S.-L. Hsu, J. Xiao, H. Zhang, R. Wagner, A. Datar, M. R. McCarter, C. R. Serrao, A. K. Yadav, G. Karbasian, C.-H. Hsu, A. J. Tan, L.-C. Wang, V. Thakare, X. Zhang, A. Mehta, E. Karapetrova, R. V. Chopdekar, P. Shafer, E. Arenholz, C. Hu, R. Proksch, R. Ramesh, J. Ciston, S. Salahuddin, *Nature* **2020**, *580*, 478.
[15] Y. Xu, J. D. Mackenzie, *Integr. Ferroelectr.* **2006**, *1*, 17.
[16] H. Ohta, K. Nomura, M. Orita, M. Hirano, K. Ueda, T. Suzuki, Y. Ikuhara, H. Hosono, *Adv. Funct. Mater.* **2003**, *13*, 139.
[17] N. Cherief, C. D'Anterroches, R. C. Cinti, T. A. N. Tan, J. Derrien, *Appl. Phys. Lett.* **1989**, *55*, 1671.
[18] Y. Nezu, Y.-Q. Zhang, C. Chen, Y. Ikuhara, H. Ohta, *J. Appl. Phys.* **2017**, *122*, 135305.
[19] J. F. Scott, C. A. P. de Araujo, *Science* **1989**, *246*, 1400.
[20] C. A. Paz De Araujo, L. D. McMillan, B. M. Melnick, J. D. Cuchiaro, J. F. Scott, *Ferroelectrics* **1990**, *104*, 241.
[21] I. K. Yoo, S. B. Desu, *Phys. Status Solidi A* **1992**, *133*, 565.
[22] A. K. Tagantsev, I. Stolichnov, E. L. Colla, N. Setter, *J. Appl. Phys.* **2001**, *90*, 1387.
[23] W. Wu, K. H. Wong, C. L. Choy, Y. H. Zhang, *Appl. Phys. Lett.* **2000**, *77*, 3441.
[24] W. L. Warren, D. Dimos, R. M. Waser, *MRS Bull.* **1996**, *21*, 40.
[25] C. B. Eom, R. B. Van Dover, J. M. Phillips, D. J. Werder, J. H. Marshall, C. H. Chen, R. J. Cava, R. M. Fleming, D. K. Fork, *Appl. Phys. Lett.* **1993**, *63*, 2570.
[26] G. W. Pabst, L. W. Martin, Y.-H. Chu, R. Ramesh, *Appl. Phys. Lett.* **2007**, *90*, 072902.
[27] B. Nagaraj, S. Aggarwal, R. Ramesh, *J. Appl. Phys.* **2001**, *90*, 375.
[28] W. L. Warren, B. A. Tuttle, D. Dimos, G. E. Pike, H. N. Al-Shareef, R. Ramesh, J. T. Evans Jr., *Jpn. J. Appl. Phys.* **2014**, *35*, 1521.
[29] A. K. Tagantsev, G. Gerra, *J. Appl. Phys.* **2006**, *100*, 051607.
[30] G. Arlt, H. Neumann, *Ferroelectrics* **1988**, *87*, 109.
[31] K. Ishikawa, K. Yoshikawa, N. Okada, *Phys. Rev. B* **1988**, *37*, 5852.
[32] S. Schlag, H.-F. Eicke, *Solid State Commun.* **1994**, *91*, 883.
[33] R. N. Viswanath, S. Ramasamy, K. Shanmugam, R. Ramamoorthy, *J. Mater. Sci. Lett.* **1995**, *14*, 841.
[34] C. A. Randall, N. Kim, J. Kucera, W. Cao, T. R. Shrout, *J. Am. Ceram. Soc.* **1998**, *81*, 677.
[35] W. L. Zhong, Y. G. Wang, P. L. Zhang, B. D. Qu, *Phys. Rev. B* **1994**, *50*, 698.
[36] S. Li, J. A. Eastman, J. M. Vetrone, C. M. Foster, R. E. Newnham, L. E. Cross, *Jpn. J. Appl. Phys.* **1997**, *36*, 5169.
[37] T. Tybell, C. H. Ahn, J.-M. Triscone, *Appl. Phys. Lett.* **1999**, *75*, 856.
[38] Ph. Ghosez, K. M. Rabe, *Appl. Phys. Lett.* **2000**, *76*, 2767.
[39] B. Meyer, D. Vanderbilt, *Phys. Rev. B* **2001**, *63*, 205426.
[40] J. Junquera, P. Ghosez, *Nature* **2003**, *422*, 506.
[41] N. Sai, A. M. Kolpak, A. M. Rappe, *Phys. Rev. B* **2005**, *72*, 020101.
[42] D. D. Fong, G. B. Stephenson, S. K. Streiffer, J. A. Eastman, O. Auciello, P. H. Fuoss, C. Thompson, *Science* **2004**, *304*, 1650.
[43] Y. S. Kim, D. H. Kim, J. D. Kim, Y. J. Chang, T. W. Noh, J. H. Kong, K. Char, Y. D. Park, S. D. Bu, J.-G. Yoon, J.-S. Chung, *Appl. Phys. Lett.* **2005**, *86*, 102907.
[44] D. D. Fong, A. M. Kolpak, J. A. Eastman, S. K. Streiffer, P. H. Fuoss, G. B. Stephenson, C. Thompson, D. M. Kim, K. J. Choi, C. B. Eom, I. Grinberg, A. M. Rappe, *Phys. Rev. Lett.* **2006**, *96*, 127601.
[45] V. Nagarajan, J. Junquera, J. Q. He, C. L. Jia, R. Waser, K. Lee, Y. K. Kim, S. Baik, T. Zhao, R. Ramesh, P. Ghosez, K. M. Rabe, *J. Appl. Phys.* **2006**, *100*, 051609.
[46] C.-L. Jia, V. Nagarajan, J.-Q. He, L. Houben, T. Zhao, R. Ramesh, K. Urban, R. Waser, *Nat. Mater.* **2007**, *6*, 64.
[47] P. W. Forsbergh, *Phys. Rev.* **1953**, *93*, 686.
[48] N. A. Pertsev, A. G. Zembilgotov, A. K. Tagantsev, *Phys. Rev. Lett.* **1998**, *80*, 1988.
[49] N. A. Pertsev, A. G. Zembilgotov, A. K. Tagantsev, *Ferroelectrics* **1999**, *223*, 79.
[50] N. A. Pertsev, V. G. Kukhar, H. Kohlstedt, R. Waser, *Phys. Rev. B* **2003**, *67*, 054107.
[51] N. A. Pertsev, A. K. Tagantsev, N. Setter, *Phys. Rev. B* **2000**, *61*, R825.
[52] R. E. Cohen, H. Krakauer, *Phys. Rev. B* **1990**, *42*, 6416.
[53] R. E. Cohen, *Nature* **1992**, *358*, 136.
[54] R. D. King-Smith, D. Vanderbilt, *Phys. Rev. B* **1994**, *49*, 5828.
[55] C. Bungaro, K. M. Rabe, *Phys. Rev. B* **2004**, *69*, 184101.
[56] O. Diéguez, K. M. Rabe, D. Vanderbilt, *Phys. Rev. B* **2005**, *72*, 144101.
[57] O. Diéguez, S. Tinte, A. Antons, C. Bungaro, J. B. Neaton, K. M. Rabe, D. Vanderbilt, *Phys. Rev. B* **2004**, *69*, 212101.
[58] K. M. Rabe, *Curr. Opin. Solid State Mater. Sci.* **2005**, *9*, 122.
[59] C. Ederer, N. A. Spaldin, *Phys. Rev. Lett.* **2005**, *95*, 257601.
[60] C.-J. Eklund, C. J. Fennie, K. M. Rabe, *Phys. Rev. B* **2009**, *79*, 220101.
[61] C. J. Fennie, K. M. Rabe, *Phys. Rev. Lett.* **2006**, *97*, 267602.
[62] J. M. Rondinelli, A. S. Eidelson, N. A. Spaldin, *Phys. Rev. B* **2009**, *79*, 205119.
[63] S. Bhattacharjee, E. Bousquet, P. Ghosez, *Phys. Rev. Lett.* **2009**, *102*, 117602.
[64] J. H. Haeni, P. Irvin, W. Chang, R. Uecker, P. Reiche, Y. L. Li, S. Choudhury, W. Tian, M. E. Hawley, B. Craigo, A. K. Tagantsev, X. Q. Pan, S. K. Streiffer, L. Q. Chen, S. W. Kirchoefer, J. Levy, D. G. Schlom, *Nature* **2004**, *430*, 758.
[65] K. J. Choi, M. Biegalski, Y. L. Li, A. Sharan, J. Schubert, R. Uecker, P. Reiche, Y. B. Chen, X. Q. Pan, V. Gopalan, L.-Q. Chen, D. G. Schlom, C. B. Eom, *Science* **2004**, *306*, 1005.
[66] R. J. Zeches, M. D. Rossell, J. X. Zhang, A. J. Hatt, Q. He, C.-H. Yang, A. Kumar, C. H. Wang, A. Melville, C. Adamo, G. Sheng, Y.-H. Chu, J. F. Ihlefeld, R. Erni, C. Ederer, V. Gopalan, L. Q. Chen, D. G. Schlom, N. A. Spaldin, L. W. Martin, R. Ramesh, *Science* **2009**, *326*, 977.
[67] A. R. Damodaran, J. C. Agar, S. Pandya, Z. Chen, L. Dedon, R. Xu, B. Apgar, S. Saremi, L. W. Martin, *J. Phys.: Condens. Matter* **2016**, *28*, 263001.
[68] N. A. Pertsev, V. G. Koukhar, *Phys. Rev. Lett.* **2000**, *84*, 3722.
[69] V. G. Koukhar, N. A. Pertsev, R. Waser, *Phys. Rev. B* **2001**, *64*, 214103.
[70] L. Chen, *J. Am. Ceram. Soc.* **2008**, *91*, 1835.
[71] H.-L. Hu, L.-Q. Chen, *Mater. Sci. Eng., A* **1997**, *238*, 182.
[72] S. Nambu, D. A. Sagala, *Phys. Rev. B* **1994**, *50*, 5838.
[73] W. Yang, L. Chen, *J. Am. Ceram. Soc.* **1995**, *78*, 2554.
[74] Y. L. Li, S. Y. Hu, Z. K. Liu, L. Q. Chen, *Appl. Phys. Lett.* **2001**, *78*, 3878.
[75] Y. L. Li, L. Q. Chen, *Appl. Phys. Lett.* **2006**, *88*, 072905.
[76] Y.-H. Shin, V. R. Cooper, I. Grinberg, A. M. Rappe, *Phys. Rev. B* **2005**, *71*, 054104.
[77] Y.-H. Shin, I. Grinberg, I.-W. Chen, A. M. Rappe, *Nature* **2007**, *449*, 881.
[78] L. M. Eng, H.-J. Güntherodt, G. Rosenman, A. Skliar, M. Oron, M. Katz, D. Eger, *J. Appl. Phys.* **1998**, *83*, 5973.

[79] L. M. Eng, H.-J. Güntherodt, *Ferroelectrics* **2000**, *236*, 35.
[80] C. S. Ganpule, V. Nagarajan, B. K. Hill, A. L. Roytburd, E. D. Williams, R. Ramesh, S. P. Alpay, A. Roelofs, R. Waser, L. M. Eng, *J. Appl. Phys.* **2002**, *91*, 1477.
[81] J. Seidel, L. W. Martin, Q. He, Q. Zhan, Y.-H. Chu, A. Rother, M. E. Hawkridge, P. Maksymovych, P. Yu, M. Gajek, N. Balke, S. V. Kalinin, S. Gemming, F. Wang, G. Catalan, J. F. Scott, N. A. Spaldin, J. Orenstein, R. Ramesh, *Nat. Mater.* **2009**, *8*, 229.
[82] L. Feigl, P. Yudin, I. Stolichnov, T. Sluka, K. Shapovalov, M. Mtebwa, C. S. Sandu, X.-K. Wei, A. K. Tagantsev, N. Setter, *Nat. Commun.* **2014**, *5*, 4677.
[83] J. Guyonnet, I. Gaponenko, S. Gariglio, P. Paruch, *Adv. Mater.* **2011**, *23*, 5377.
[84] J. C. Agar, Y. Cao, B. Naul, S. Pandya, S. van der Walt, A. I. Luo, J. T. Maher, N. Balke, S. Jesse, S. V. Kalinin, R. K. Vasudevan, L. W. Martin, *Adv. Mater.* **2018**, *30*, 1800701.
[85] A. R. Damodaran, S. Pandya, J. C. Agar, Y. Cao, R. K. Vasudevan, R. Xu, S. Saremi, Q. Li, J. Kim, M. R. McCarter, L. R. Dedon, T. Angsten, N. Balke, S. Jesse, M. Asta, S. V. Kalinin, L. W. Martin, *Adv. Mater.* **2017**, *29*, 1702069.
[86] S. Jesse, S. V. Kalinin, R. Proksch, A. P. Baddorf, B. J. Rodriguez, *Nanotechnology* **2007**, *18*, 435503.
[87] K. S. Lee, J. H. Choi, J. Y. Lee, S. Baik, *J. Appl. Phys.* **2001**, *90*, 4095.
[88] V. Nagarajan, I. G. Jenkins, S. P. Alpay, H. Li, S. Aggarwal, L. Salamanca-Riba, A. L. Roytburd, R. Ramesh, *J. Appl. Phys.* **1999**, *86*, 595.
[89] S. K. Streiffer, J. A. Eastman, D. D. Fong, C. Thompson, A. Munkholm, M. V. R. Murty, O. Auciello, G. R. Bai, G. B. Stephenson, *Phys. Rev. Lett.* **2002**, *89*, 067601.
[90] L. Feigl, L. J. McGilly, C. S. Sandu, N. Setter, *Appl. Phys. Lett.* **2014**, *104*, 172904.
[91] S. Matzen, O. Nesterov, G. Rispens, J. A. Heuver, M. Biegalski, H. M. Christen, B. Noheda, *Nat. Commun.* **2014**, *5*, 4415.
[92] Y.-H. Chu, M. P. Cruz, C.-H. Yang, L. W. Martin, P.-L. Yang, J.-X. Zhang, K. Lee, P. Yu, L.-Q. Chen, R. Ramesh, *Adv. Mater.* **2007**, *19*, 2662.
[93] Y.-H. Chu, Q. Zhan, L. W. Martin, M. P. Cruz, P.-L. Yang, G. W. Pabst, F. Zavaliche, S.-Y. Yang, J.-X. Zhang, L.-Q. Chen, D. G. Schlom, I.-N. Lin, T.-B. Wu, R. Ramesh, *Adv. Mater.* **2006**, *18*, 2307.
[94] H. W. Jang, D. Ortiz, S. Baek, C. M. Folkman, R. R. Das, P. Shafer, Y. Chen, C. T. Nelson, X. Pan, R. Ramesh, C. Eom, *Adv. Mater.* **2009**, *21*, 817.
[95] J. X. Zhang, B. Xiang, Q. He, J. Seidel, R. J. Zeches, P. Yu, S. Y. Yang, C. H. Wang, Y.-H. Chu, L. W. Martin, A. M. Minor, R. Ramesh, *Nat. Nanotechnol.* **2011**, *6*, 98.
[96] A. R. Damodaran, C. Liang, Q. He, C. Peng, L. Chang, Y. Chu, L. W. Martin, *Adv. Mater.* **2011**, *23*, 3170.
[97] Q. He, Y.-H. Chu, J. T. Heron, S. Y. Yang, W. I. Liang, C. Y. Kuo, H. J. Lin, P. Yu, C. W. Liang, R. J. Zeches, W. C. Kuo, J. Y. Juang, C. T. Chen, E. Arenholz, A. Scholl, R. Ramesh, *Nat. Commun.* **2011**, *2*, 225.
[98] J. Karthik, A. R. Damodaran, L. W. Martin, *Phys. Rev. Lett.* **2012**, *108*, 167601.
[99] J. Karthik, L. W. Martin, *Appl. Phys. Lett.* **2011**, *99*, 032904.
[100] J. Karthik, L. W. Martin, *Phys. Rev. B* **2011**, *84*, 024102.
[101] T. Rojac, A. Bencan, G. Drazic, N. Sakamoto, H. Ursic, B. Jancar, G. Tavcar, M. Makarovic, J. Walker, B. Malic, D. Damjanovic, *Nat. Mater.* **2017**, *16*, 322.
[102] A. Bernal, S. Zhang, N. Bassiri-Gharb, *Appl. Phys. Lett.* **2009**, *95*, 142911.
[103] S. Wada, K. Yako, H. Kakemoto, T. Tsurumi, T. Kiguchi, *J. Appl. Phys.* **2005**, *98*, 014109.
[104] R. Xu, J. Zhang, Z. Chen, L. W. Martin, *Phys. Rev. B* **2015**, *91*, 144106.
[105] J. Li, J. Wang, M. Wuttig, R. Ramesh, N. Wang, B. Ruette, A. P. Pyatakov, A. K. Zvezdin, D. Viehland, *Appl. Phys. Lett.* **2004**, *84*, 5261.
[106] R. Oja, K. Johnston, J. Frantti, R. M. Nieminen, *Phys. Rev. B* **2008**, *78*, 094102.
[107] H. Cao, F. Bai, N. Wang, J. Li, D. Viehland, G. Xu, G. Shirane, *Phys. Rev. B* **2005**, *72*, 064104.
[108] S. C. Ray, H. C. Hsueh, C. H. Wu, C. W. Pao, K. Asokan, M. T. Liu, H. M. Tsai, C. H. Chuang, W. F. Pong, J. W. Chiou, M.-H. Tsai, J. M. Lee, L. Y. Jang, J. M. Chen, J. F. Lee, *Appl. Phys. Lett.* **2011**, *99*, 042909.
[109] O. Nakagawara, T. Shimuta, T. Makino, S. Arai, H. Tabata, T. Kawai, *Appl. Phys. Lett.* **2000**, *77*, 3257.
[110] J. Zhu, L. Zheng, W. B. Luo, Y. R. Li, Y. Zhang, *J. Phys. D: Appl. Phys.* **2006**, *39*, 2438.
[111] R. Xu, J. Karthik, A. R. Damodaran, L. W. Martin, *Nat. Commun.* **2014**, *5*, 3120.
[112] S. Liu, R. E. Cohen, *Phys. Rev. B* **2017**, *95*, 094102.
[113] R. Xu, R. Gao, S. E. Reyes-Lillo, S. Saremi, Y. Dong, H. Lu, Z. Chen, X. Lu, Y. Qi, S.-L. Hsu, A. R. Damodaran, H. Zhou, J. B. Neaton, L. W. Martin, *ACS Nano* **2018**, *12*, 4736.
[114] R. Xu, S. Liu, I. Grinberg, J. Karthik, A. R. Damodaran, A. M. Rappe, L. W. Martin, *Nat. Mater.* **2015**, *14*, 79.
[115] R. Ramesh, D. G. Schlom, *Nat. Rev. Mater.* **2019**, *4*, 257.
[116] J. M. Rondinelli, S. J. May, J. W. Freeland, *MRS Bull.* **2012**, *37*, 261.
[117] A. Bhattacharya, S. J. May, *Annu. Rev. Mater. Res.* **2014**, *44*, 65.
[118] D. G. Schlom, L.-Q. Chen, C.-B. Eom, K. M. Rabe, S. K. Streiffer, J.-M. Triscone, *Annu. Rev. Mater. Res.* **2007**, *37*, 589.
[119] S. Hasegawa, in *Characterization of Materials*, 2nd ed., (Ed: E. N. Kaufmann), John Wiley & Sons **2012**, https://doi.org/10.1002/0471266965.com139.
[120] H. Yamada, M. Kawasaki, Y. Ogawa, Y. Tokura, *Appl. Phys. Lett.* **2002**, *81*, 4793.
[121] H. N. Lee, H. M. Christen, M. F. Chisholm, C. M. Rouleau, D. H. Lowndes, *Nature* **2005**, *433*, 395.
[122] N. Sai, B. Meyer, D. Vanderbilt, *Phys. Rev. Lett.* **2000**, *84*, 5636.
[123] S. M. Nakhmanson, K. M. Rabe, D. Vanderbilt, *Appl. Phys. Lett.* **2005**, *87*, 102906.
[124] Y. Cao, Z. Wang, S. Y. Park, Y. Yuan, X. Liu, S. M. Nikitin, H. Akamatsu, M. Kareev, S. Middey, D. Meyers, P. Thompson, P. J. Ryan, P. Shafer, A. N'Diaye, E. Arenholz, V. Gopalan, Y. Zhu, K. M. Rabe, J. Chakhalian, *Nat. Commun.* **2018**, *9*, 1547.
[125] L. Wang, Q. Feng, Y. Kim, R. Kim, K. H. Lee, S. D. Pollard, Y. J. Shin, H. Zhou, W. Peng, D. Lee, W. Meng, H. Yang, J. H. Han, M. Kim, Q. Lu, T. W. Noh, *Nat. Mater.* **2018**, *17*, 1087.
[126] T. H. Kim, D. Puggioni, Y. Yuan, L. Xie, H. Zhou, N. Campbell, P. J. Ryan, Y. Choi, J.-W. Kim, J. R. Patzner, S. Ryu, J. P. Podkaminer, J. Irwin, Y. Ma, C. J. Fennie, M. S. Rzchowski, X. Q. Pan, V. Gopalan, J. M. Rondinelli, C. B. Eom, *Nature* **2016**, *533*, 68.
[127] N. D. Mermin, *Rev. Mod. Phys.* **1979**, *51*, 591.
[128] Y. Tokura, K. Yasuda, A. Tsukazaki, *Nat. Rev. Phys.* **2019**, *1*, 126.
[129] R. D. Gomez, T. V. Luu, A. O. Pak, K. J. Kirk, J. N. Chapman, *J. Appl. Phys.* **1999**, *85*, 6163.
[130] T. Shinjo, T. Okuno, R. Hassdorf, K. Shigeto, T. Ono, *Science* **2000**, *289*, 930.
[131] S. Mühlbauer, B. Binz, F. Jonietz, C. Pfleiderer, A. Rosch, A. Neubauer, R. Georgii, P. Böni, *Science* **2009**, *323*, 915.
[132] H. Fu, L. Bellaiche, *Phys. Rev. Lett.* **2003**, *91*, 257601.
[133] I. I. Naumov, L. Bellaiche, H. Fu, *Nature* **2004**, *432*, 737.
[134] E. Bousquet, M. Dawber, N. Stucki, C. Lichtensteiger, P. Hermet, S. Gariglio, J.-M. Triscone, P. Ghosez, *Nature* **2008**, *452*, 732.
[135] C.-L. Jia, K. W. Urban, M. Alexe, D. Hesse, I. Vrejoiu, *Science* **2011**, *331*, 1420.

[136] Y. L. Tang, Y. L. Zhu, X. L. Ma, A. Y. Borisevich, A. N. Morozovska, E. A. Eliseev, W. Y. Wang, Y. J. Wang, Y. B. Xu, Z. D. Zhang, S. J. Pennycook, *Science* **2015**, *348*, 547.
[137] A. K. Yadav, C. T. Nelson, S. L. Hsu, Z. Hong, J. D. Clarkson, C. M. Schlepütz, A. R. Damodaran, P. Shafer, E. Arenholz, L. R. Dedon, D. Chen, A. Vishwanath, A. M. Minor, L. Q. Chen, J. F. Scott, L. W. Martin, R. Ramesh, *Nature* **2016**, *530*, 198.
[138] A. R. Damodaran, J. D. Clarkson, Z. Hong, H. Liu, A. K. Yadav, C. T. Nelson, S.-L. Hsu, M. R. McCarter, K.-D. Park, V. Kravtsov, A. Farhan, Y. Dong, Z. Cai, H. Zhou, P. Aguado-Puente, P. García-Fernández, J. Íñiguez, J. Junquera, A. Scholl, M. B. Raschke, L.-Q. Chen, D. D. Fong, R. Ramesh, L. W. Martin, *Nat. Mater.* **2017**, *16*, 1003.
[139] P. Shafer, P. García-Fernández, P. Aguado-Puente, A. R. Damodaran, A. K. Yadav, C. T. Nelson, S.-L. Hsu, J. C. Wojdeł, J. Íñiguez, L. W. Martin, E. Arenholz, J. Junquera, R. Ramesh, *Proc. Natl. Acad. Sci. USA* **2018**, *115*, 915.
[140] V. A. Stoica, N. Laanait, C. Dai, Z. Hong, Y. Yuan, Z. Zhang, S. Lei, M. R. McCarter, A. Yadav, A. R. Damodaran, S. Das, G. A. Stone, J. Karapetrova, D. A. Walko, X. Zhang, L. W. Martin, R. Ramesh, L.-Q. Chen, H. Wen, V. Gopalan, J. W. Freeland, *Nat. Mater.* **2019**, *18*, 377.
[141] Q. Li, V. A. Stoica, M. Paściak, Y. Zhu, Y. Yuan, T. Yang, M. R. McCarter, S. Das, A. K. Yadav, S. Park, C. Dai, H. J. Lee, Y. Ahn, S. D. Marks, S. Yu, C. Kadlec, T. Sato, M. C. Hoffmann, M. Chollet, M. E. Kozina, S. Nelson, D. Zhu, D. A. Walko, A. M. Lindenberg, P. G. Evans, L.-Q. Chen, R. Ramesh, L. W. Martin, V. Gopalan, J. W. Freeland, et al., *Nature* **2021**, *592*, 376.
[142] S. Das, Y. L. Tang, Z. Hong, M. A. P. Gonçalves, M. R. McCarter, C. Klewe, K. X. Nguyen, F. Gómez-Ortiz, P. Shafer, E. Arenholz, V. A. Stoica, S.-L. Hsu, B. Wang, C. Ophus, J. F. Liu, C. T. Nelson, S. Saremi, B. Prasad, A. B. Mei, D. G. Schlom, J. Íñiguez, P. García-Fernández, D. A. Muller, L. Q. Chen, J. Junquera, L. W. Martin, R. Ramesh, *Nature* **2019**, *568*, 368.
[143] S. Das, Z. Hong, V. A. Stoica, M. A. P. Gonçalves, Y. T. Shao, E. Parsonnet, E. J. Marksz, S. Saremi, M. R. McCarter, A. Reynoso, C. J. Long, A. M. Hagerstrom, D. Meyers, V. Ravi, B. Prasad, H. Zhou, Z. Zhang, H. Wen, F. Gómez-Ortiz, P. García-Fernández, J. Bokor, J. Íñiguez, J. W. Freeland, N. D. Orloff, J. Junquera, L. Q. Chen, S. Salahuddin, D. A. Muller, L. W. Martin, R. Ramesh, *Nat. Mater.* **2021**, *20*, 194.
[144] P. Zubko, J. C. Wojdeł, M. Hadjimichael, S. Fernandez-Pena, A. Sené, I. Luk'yanchuk, J.-M. Triscone, J. Íñiguez, *Nature* **2016**, *534*, 524.
[145] J. Wang, S.-Q. Shi, L.-Q. Chen, Y. Li, T.-Y. Zhang, *Acta Mater.* **2004**, *52*, 749.
[146] J.-J. Wang, B. Wang, L.-Q. Chen, *Annu. Rev. Mater. Res.* **2019**, *49*, 127.
[147] Z. Hong, A. R. Damodaran, F. Xue, S.-L. Hsu, J. Britson, A. K. Yadav, C. T. Nelson, J.-J. Wang, J. F. Scott, L. W. Martin, R. Ramesh, L.-Q. Chen, *Nano Lett.* **2017**, *17*, 2246.
[148] P. García-Fernández, J. C. Wojdeł, J. Íñiguez, J. Junquera, *Phys. Rev. B* **2016**, *93*, 195137.
[149] P. Zubko, G. Catalan, A. K. Tagantsev, *Annu. Rev. Mater. Res.* **2013**, *43*, 387.
[150] D. Lee, *APL Mater.* **2020**, *8*, 090901.
[151] H. Lu, C.-W. Bark, E. de los Ojos, J. Alcala, C. B. Eom, G. Catalan, A. Gruverman, *Science* **2012**, *336*, 59.
[152] S. M. Park, B. Wang, S. Das, S. C. Chae, J.-S. Chung, J.-G. Yoon, L.-Q. Chen, S. M. Yang, T. W. Noh, *Nat. Nanotechnol.* **2018**, *13*, 366.
[153] S. Das, B. Wang, Y. Cao, M. R. Cho, Y. J. Shin, S. M. Yang, L. Wang, M. Kim, S. V. Kalinin, L.-Q. Chen, T. W. Noh, *Nat. Commun.* **2017**, *8*, 615.
[154] S. Das, B. Wang, T. R. Paudel, S. M. Park, E. Y. Tsymbal, L.-Q. Chen, D. Lee, T. W. Noh, *Nat. Commun.* **2019**, *10*, 537.
[155] S. M. Park, B. Wang, T. Paudel, S. Y. Park, S. Das, J. R. Kim, E. K. Ko, H. G. Lee, N. Park, L. Tao, D. Suh, E. Y. Tsymbal, L.-Q. Chen, T. W. Noh, D. Lee, *Nat. Commun.* **2020**, *11*, 2586.
[156] P. Zubko, G. Catalan, A. Buckley, P. R. L. Welche, J. F. Scott, *Phys. Rev. Lett.* **2007**, *99*, 167601.
[157] G. Catalan, A. Lubk, A. H. G. Vlooswijk, E. Snoeck, C. Magen, A. Janssens, G. Rispens, G. Rijnders, D. H. A. Blank, B. Noheda, *Nat. Mater.* **2011**, *10*, 963.
[158] K. Chu, B.-K. Jang, J. H. Sung, Y. A. Shin, E.-S. Lee, K. Song, J. H. Lee, C.-S. Woo, S. J. Kim, S.-Y. Choi, T. Y. Koo, Y.-H. Kim, S.-H. Oh, M.-H. Jo, C.-H. Yang, *Nat. Nanotechnol.* **2015**, *10*, 972.
[159] D. Lee, A. Yoon, S. Y. Jang, J.-G. Yoon, J.-S. Chung, M. Kim, J. F. Scott, T. W. Noh, *Phys. Rev. Lett.* **2011**, *107*, 057602.
[160] D. Lee, B. C. Jeon, A. Yoon, Y. J. Shin, M. H. Lee, T. K. Song, S. D. Bu, M. Kim, J. Chung, J. Yoon, T. W. Noh, *Adv. Mater.* **2014**, *26*, 5005.
[161] B. C. Jeon, D. Lee, M. H. Lee, S. M. Yang, S. C. Chae, T. K. Song, S. D. Bu, J. Chung, J. Yoon, T. W. Noh, *Adv. Mater.* **2013**, *25*, 5643.
[162] R. V. K. Mangalam, J. Karthik, A. R. Damodaran, J. C. Agar, L. W. Martin, *Adv. Mater.* **2013**, *25*, 1761.
[163] A. R. Damodaran, S. Pandya, Y. Qi, S.-L. Hsu, S. Liu, C. Nelson, A. Dasgupta, P. Ercius, C. Ophus, L. R. Dedon, J. C. Agar, H. Lu, J. Zhang, A. M. Minor, A. M. Rappe, L. W. Martin, *Nat. Commun.* **2017**, *8*, 14961.
[164] J. C. Agar, A. R. Damodaran, M. B. Okatan, J. Kacher, C. Gammer, R. K. Vasudevan, S. Pandya, L. R. Dedon, R. V. K. Mangalam, G. A. Velarde, S. Jesse, N. Balke, A. M. Minor, S. V. Kalinin, L. W. Martin, *Nat. Mater.* **2016**, *15*, 549.
[165] N. Choudhury, L. Walizer, S. Lisenkov, L. Bellaiche, *Nature* **2011**, *470*, 513.
[166] M. Brazier, M. McElfresh, S. Mansour, *Appl. Phys. Lett.* **1998**, *72*, 1121.
[167] H. Koinuma, *Solid State Ionics* **1998**, *108*, 1.
[168] H. Koinuma, I. Takeuchi, *Nat. Mater.* **2004**, *3*, 429.
[169] M. L. Green, I. Takeuchi, J. R. Hattrick-Simpers, *J. Appl. Phys.* **2013**, *113*, 231101.
[170] X.-D. Xiang, X. Sun, G. Briceño, Y. Lou, K.-A. Wang, H. Chang, W. G. Wallace-Freedman, S.-W. Chen, P. G. Schultz, *Science* **1995**, *268*, 1738.
[171] H. Chang, C. Gao, I. Takeuchi, Y. Yoo, J. Wang, P. G. Schultz, X.-D. Xiang, R. P. Sharma, M. Downes, T. Venkatesan, *Appl. Phys. Lett.* **1998**, *72*, 2185.
[172] D. Kan, C. J. Long, C. Steinmetz, S. E. Lofland, I. Takeuchi, *J. Mater. Res.* **2012**, *27*, 2691.
[173] G. He, T. Iijima, H. Funakubo, *J. Mater. Res.* **2002**, *17*, 2217.
[174] J. Li, F. Duewer, C. Gao, H. Chang, X.-D. Xiang, Y. Lu, *Appl. Phys. Lett.* **2000**, *76*, 769.
[175] I. Takeuchi, H. Chang, C. Gao, P. G. Schultz, X.-D. Xiang, R. P. Sharma, M. J. Downes, T. Venkatesan, *Appl. Phys. Lett.* **1998**, *73*, 894.
[176] H. Chang, I. Takeuchi, X.-D. Xiang, *Appl. Phys. Lett.* **1999**, *74*, 1165.
[177] T. Ohnishi, D. Komiyama, T. Koida, S. Ohashi, C. Stauter, H. Koinuma, A. Ohtomo, M. Lippmaa, N. Nakagawa, M. Kawasaki, T. Kikuchi, K. Omote, *Appl. Phys. Lett.* **2001**, *79*, 536.
[178] L. Hong, A. K. Soh, Q. G. Du, J. Y. Li, *Phys. Rev. B* **2008**, *77*, 094104.
[179] L. He, D. Vanderbilt, *Phys. Rev. B* **2003**, *68*, 134103.
[180] I. Stolichnov, L. Feigl, L. J. McGilly, T. Sluka, X.-K. Wei, E. Colla, A. Crassous, K. Shapovalov, P. Yudin, A. K. Tagantsev, N. Setter, *Nano Lett.* **2015**, *15*, 8049.
[181] D. V. Lang, *J. Appl. Phys.* **1974**, *45*, 3023.
[182] S. Saremi, R. Xu, L. R. Dedon, R. Gao, A. Ghosh, A. Dasgupta, L. W. Martin, *Adv. Mater. Interfaces* **2018**, *5*, 1700991.

[183] A. Dasgupta, S. Saremi, X. Ruijuan, L. R. Dedon, S. Pandya, A. R. Damodaran, L. W. Martin, *J. Mater. Chem. C* **2018**, *6*, 10751.
[184] S. Saremi, R. Xu, L. R. Dedon, J. A. Mundy, S.-L. Hsu, Z. Chen, A. R. Damodaran, S. P. Chapman, J. T. Evans, L. W. Martin, *Adv. Mater.* **2016**, *28*, 10750.
[185] S. Saremi, R. Gao, A. Dasgupta, L. W. Martin, *Bull. Am. Ceram. Soc.* **2018**, *97*, 16.
[186] L. R. Dedon, S. Saremi, Z. Chen, A. R. Damodaran, B. A. Apgar, R. Gao, L. W. Martin, *Chem. Mater.* **2016**, *28*, 5952.
[187] R. Gao, S. E. Reyes-Lillo, R. Xu, A. Dasgupta, Y. Dong, L. R. Dedon, J. Kim, S. Saremi, Z. Chen, C. R. Serrao, H. Zhou, J. B. Neaton, L. W. Martin, *Chem. Mater.* **2017**, *24*, 331.
[188] M. H. Park, Y. H. Lee, H. J. Kim, Y. J. Kim, T. Moon, K. D. Kim, J. Müller, A. Kersch, U. Schroeder, T. Mikolajick, C. S. Hwang, *Adv. Mater.* **2015**, *27*, 1811.
[189] M. H. Park, Y. H. Lee, T. Mikolajick, U. Schroeder, C. S. Hwang, *MRS Commun.* **2018**, *8*, 795.
[190] T. D. Huan, V. Sharma, G. A. Rossetti, R. Ramprasad, *Phys. Rev. B* **2014**, *90*, 064111.
[191] J. Lyu, I. Fina, R. Solanas, J. Fontcuberta, F. Sánchez, *Appl. Phys. Lett.* **2018**, *113*, 082902.
[192] Y.-L. Huang, D. Nikonov, C. Addiego, R. V. Chopdekar, B. Prasad, L. Zhang, J. Chatterjee, H.-J. Liu, A. Farhan, Y.-H. Chu, M. Yang, M. Ramesh, Z. Q. Qiu, B. D. Huey, C.-C. Lin, T. Gosavi, J. Íñiguez, J. Bokor, X. Pan, I. Young, L. W. Martin, R. Ramesh, *Nat. Commun.* **2020**, *11*, 2836.
[193] L. You, F. Zheng, L. Fang, Y. Zhou, L. Z. Tan, Z. Zhang, G. Ma, D. Schmidt, A. Rusydi, L. Wang, L. Chang, A. M. Rappe, J. Wang, *Sci. Adv.* **2018**, *4*, eaat3438.
[194] A. B. Mei, S. Saremi, L. Miao, M. Barone, Y. Tang, C. Zeledon, J. Schubert, D. C. Ralph, L. W. Martin, D. G. Schlom, *APL Mater.* **2019**, *7*, 111101.
[195] S. Saremi, R. Xu, F. I. Allen, J. Maher, J. C. Agar, R. Gao, P. Hosemann, L. W. Martin, *Phys. Rev. Mater.* **2018**, *2*, 084414.
[196] L. Mazet, S. M. Yang, S. V. Kalinin, S. Schamm-Chardon, C. Dubourdieu, *Sci. Technol. Adv. Mater.* **2016**, *16*, 036005.
[197] M. Scigaj, N. Dix, I. Fina, R. Bachelet, B. Warot-Fonrose, J. Fontcuberta, F. Sánchez, *Appl. Phys. Lett.* **2013**, *102*, 112905.
[198] J. W. Reiner, A. M. Kolpak, Y. Segal, K. F. Garrity, S. Ismail-Beigi, C. H. Ahn, F. J. Walker, *Adv. Mater.* **2010**, *22*, 2919.
[199] D. M. Schaadt, E. T. Yu, V. Vaithyanathan, D. G. Schlom, *J. Vac. Sci. Technol., B: Microelectron. Nanometer Struct.–Process., Meas., Phenom.* **2004**, *22*, 2030.
[200] M. Ihara, Y. Arimoto, M. Jifuku, T. Kimura, S. Kodama, H. Yamawaki, T. Yamaoka, *J. Electrochem. Soc.* **1982**, *129*, 2569.
[201] D. K. Fork, D. B. Fenner, G. A. N. Connell, J. M. Phillips, T. H. Geballe, *Appl. Phys. Lett.* **1990**, *57*, 1137.
[202] S. J. Wang, C. K. Ong, L. P. You, S. Y. Xu, *Semicond. Sci. Technol.* **2000**, *15*, 836.
[203] M. P. Warusawithana, C. Cen, C. R. Sleasman, J. C. Woicik, Y. Li, L. F. Kourkoutis, J. A. Klug, H. Li, P. Ryan, L.-P. Wang, M. Bedzyk, D. A. Muller, L.-Q. Chen, J. Levy, D. G. Schlom, *Science* **2009**, *324*, 367.
[204] C. Dubourdieu, J. Bruley, T. M. Arruda, A. Posadas, J. Jordan-Sweet, M. M. Frank, E. Cartier, D. J. Frank, S. V. Kalinin, A. A. Demkov, V. Narayanan, *Nat. Nanotechnol.* **2013**, *8*, 748.
[205] S. Guha, N. A. Bojarczuk, V. Narayanan, *Appl. Phys. Lett.* **2002**, *80*, 766.
[206] C. Merckling, M. El-Kazzi, G. Delhaye, M. Gendry, G. Saint-Girons, G. Hollinger, L. Largeau, G. Patriarche, *Appl. Phys. Lett.* **2006**, *89*, 232907.
[207] H. Li, X. Hu, Y. Wei, Z. Yu, X. Zhang, R. Droopad, A. A. Demkov, J. Edwards, K. Moore, W. Ooms, J. Kulik, P. Fejes, *J. Appl. Phys.* **2003**, *93*, 4521.
[208] R. A. McKee, F. J. Walker, J. R. Conner, E. D. Specht, D. E. Zelmon, *Appl. Phys. Lett.* **1991**, *59*, 782.
[209] C. Rossel, B. Mereu, C. Marchiori, D. Caimi, M. Sousa, A. Guiller, H. Siegwart, R. Germann, J.-P. Locquet, J. Fompeyrine, D. J. Webb, Ch. Dieker, J. W. Seo, *Appl. Phys. Lett.* **2006**, *89*, 053506.
[210] R. A. McKee, F. J. Walker, M. F. Chisholm, *Science* **2001**, *293*, 468.
[211] R. A. McKee, F. J. Walker, M. F. Chisholm, *Phys. Rev. Lett.* **1998**, *81*, 3014.
[212] Z. Yu, Y. Liang, C. Overgaard, X. Hu, J. Curless, H. Li, Y. Wei, B. Craigo, D. Jordan, R. Droopad, J. Finder, K. Eisenbeiser, D. Marshall, K. Moore, J. Kulik, P. Fejes, *Thin Solid Films* **2004**, *462*, 51.
[213] G. Delhaye, C. Merckling, M. El-Kazzi, G. Saint-Girons, M. Gendry, Y. Robach, G. Hollinger, L. Largeau, G. Patriarche, *J. Appl. Phys.* **2006**, *100*, 124109.
[214] W. C. Fan, N. J. Wu, A. Ignatiev, *Phys. Rev. B* **1990**, *42*, 1254.
[215] Y. Wei, X. Hu, Y. Liang, D. C. Jordan, B. Craigo, R. Droopad, Z. Yu, A. Demkov, J. L. Edwards, W. J. Ooms, *J. Vac. Sci. Technol., B: Microelectron. Nanometer Struct.–Process., Meas., Phenom.* **2002**, *20*, 1402.
[216] Y. Liang, S. Gan, Y. Wei, R. Gregory, *Phys. Status Solidi B* **2006**, *243*, 2098.
[217] J. Lettieri, J. H. Haeni, D. G. Schlom, *J. Vac. Sci. Technol., A* **2002**, *20*, 1332.
[218] G. Niu, G. Saint-Girons, B. Vilquin, G. Delhaye, J.-L. Maurice, C. Botella, Y. Robach, G. Hollinger, *Appl. Phys. Lett.* **2009**, *95*, 062902.
[219] L. Mazet, R. Bachelet, L. Louahadj, D. Albertini, B. Gautier, R. Cours, S. Schamm-Chardon, G. Saint-Girons, C. Dubourdieu, *J. Appl. Phys.* **2014**, *116*, 214102.
[220] S. Abel, M. Sousa, C. Rossel, D. Caimi, M. D. Rossell, R. Erni, J. Fompeyrine, C. Marchiori, *Nanotechnology* **2013**, *24*, 285701.
[221] S. H. Baek, J. Park, D. M. Kim, V. A. Aksyuk, R. R. Das, S. D. Bu, D. A. Felker, J. Lettieri, V. Vaithyanathan, S. S. N. Bharadwaja, N. Bassiri-Gharb, Y. B. Chen, H. P. Sun, C. M. Folkman, H. W. Jang, D. J. Kreft, S. K. Streiffer, R. Ramesh, X. Q. Pan, S. Trolier-McKinstry, D. G. Schlom, M. S. Rzchowski, R. H. Blick, C. B. Eom, *Science* **2011**, *334*, 958.
[222] S.-H. Baek, C.-B. Eom, *Acta Mater.* **2013**, *61*, 2734.
[223] J. Lapano, M. Brahlek, L. Zhang, J. Roth, A. Pogrebnyakov, R. Engel-Herbert, *Nat. Commun.* **2019**, *10*, 2464.
[224] Y. Liang, J. Kulik, T. C. Eschrich, R. Droopad, Z. Yu, P. Maniar, *Appl. Phys. Lett.* **2004**, *85*, 1217.
[225] R. Contreras-Guerrero, J. P. Veazey, J. Levy, R. Droopad, *Appl. Phys. Lett.* **2013**, *102*, 012907.
[226] L. Louahadj, D. L. Bourdais, L. Largeau, G. Agnus, L. Mazet, R. Bachelet, P. Regreny, D. Albertini, V. Pillard, C. Dubourdieu, B. Gautier, P. Lecoeur, G. Saint-Girons, *Appl. Phys. Lett.* **2013**, *103*, 212901.
[227] X. Hong, A. Posadas, K. Zou, C. H. Ahn, J. Zhu, *Phys. Rev. Lett.* **2009**, *102*, 136808.
[228] X. Hong, J. Hoffman, A. Posadas, K. Zou, C. H. Ahn, J. Zhu, *Appl. Phys. Lett.* **2010**, *97*, 033114.
[229] C. Baeumer, S. P. Rogers, R. Xu, L. W. Martin, M. Shim, *Nano Lett.* **2013**, *13*, 1693.
[230] Z. Lu, C. Serrao, A. I. Khan, L. You, J. C. Wong, Y. Ye, H. Zhu, X. Zhang, S. Salahuddin, *Appl. Phys. Lett.* **2017**, *111*, 023104.
[231] K. S. Novoselov, D. Jiang, F. Schedin, T. J. Booth, V. V. Khotkevich, S. V. Morozov, A. K. Geim, *Proc. Natl. Acad. Sci. USA* **2005**, *102*, 10451.
[232] A. K. Geim, I. V. Grigorieva, *Nature* **2013**, *499*, 419.
[233] D. M. Paskiewicz, R. Sichel-Tissot, E. Karapetrova, L. Stan, D. D. Fong, *Nano Lett.* **2015**, *16*, 534.
[234] D. Lu, D. J. Baek, S. S. Hong, L. F. Kourkoutis, Y. Hikita, H. Y. Hwang, *Nat. Mater.* **2016**, *15*, 1255.

[235] D. Pesquera, E. Parsonnet, A. Qualls, R. Xu, A. J. Gubser, J. Kim, Y. Jiang, G. Velarde, Y. Huang, H. Y. Hwang, R. Ramesh, L. W. Martin, *Adv. Mater.* **2020**, *32*, 2003780.
[236] W. Kong, H. Li, K. Qiao, Y. Kim, K. Lee, Y. Nie, D. Lee, T. Osadchy, R. J. Molnar, D. K. Gaskill, R. L. Myers-Ward, K. M. Daniels, Y. Zhang, S. Sundram, Y. Yu, S. Bae, S. Rajan, Y. Shao-Horn, K. Cho, A. Ougazzaden, J. C. Grossman, J. Kim, *Nat. Mater.* **2018**, *17*, 999.
[237] Y. Kim, S. S. Cruz, K. Lee, B. O. Alawode, C. Choi, Y. Song, J. M. Johnson, C. Heidelberger, W. Kong, S. Choi, K. Qiao, I. Almansouri, E. A. Fitzgerald, J. Kong, A. M. Kolpak, J. Hwang, J. Kim, *Nature* **2017**, *544*, 340.
[238] B. Zhang, C. Yun, J. L. MacManus-Driscoll, *Nano-Micro Lett.* **2021**, *13*, 39.
[239] F. Pizzocchero, L. Gammelgaard, B. S. Jessen, J. M. Caridad, L. Wang, J. Hone, P. Bøggild, T. J. Booth, *Nat. Commun.* **2016**, *7*, 11894.
[240] D. Ji, S. Cai, T. R. Paudel, H. Sun, C. Zhang, L. Han, Y. Wei, Y. Zang, M. Gu, Y. Zhang, W. Gao, H. Huyan, W. Guo, D. Wu, Z. Gu, E. Y. Tsymbal, P. Wang, Y. Nie, X. Pan, *Nature* **2019**, *570*, 87.
[241] H. Elangovan, M. Barzilay, S. Seremi, N. Cohen, Y. Jiang, L. W. Martin, Y. Ivry, *ACS Nano* **2020**, *14*, 5053.
[242] B. Peng, R.-C. Peng, Y.-Q. Zhang, G. Dong, Z. Zhou, Y. Zhou, T. Li, Z. Liu, Z. Luo, S. Wang, Y. Xia, R. Qiu, X. Cheng, F. Xue, Z. Hu, W. Ren, Z.-G. Ye, L.-Q. Chen, Z. Shan, T. Min, M. Liu, *Sci. Adv.* **2020**, *6*, eaba5847.
[243] V. Harbola, S. Crossley, S. S. Hong, D. Lu, Y. A. Birkhölzer, Y. Hikita, H. Y. Hwang, *Nano Lett.* **2021**, *21*, 2470.
[244] S. S. Hong, M. Gu, M. Verma, V. Harbola, B. Y. Wang, D. Lu, A. Vailionis, Y. Hikita, R. Pentcheva, J. M. Rondinelli, H. Y. Hwang, *Science* **2020**, *368*, 71.
[245] R. Xu, J. Huang, E. S. Barnard, S. S. Hong, P. Singh, E. K. Wong, T. Jansen, V. Harbola, J. Xiao, B. Y. Wang, S. Crossley, D. Lu, S. Liu, H. Y. Hwang, *Nat. Commun.* **2020**, *11*, 3141.
[246] Q. Shi, E. Parsonnet, X. Cheng, N. Fedorova, R.-C. Peng, A. Fernandez, A. Qualls, X. Huang, X. Chang, H. Zhang, D. Pesquera, S. Das, D. Nikonov, I. Young, L.-Q. Chen, L. W. Martin, Y.-L. Huang, J. Íñiguez, R. Ramesh, *Nat. Commun.* **2021**, *13*, 1110.
[247] H. S. Kum, H. Lee, S. Kim, S. Lindemann, W. Kong, K. Qiao, P. Chen, J. Irwin, J. H. Lee, S. Xie, S. Subramanian, J. Shim, S.-H. Bae, C. Choi, L. Ranno, S. Seo, S. Lee, J. Bauer, H. Li, K. Lee, J. A. Robinson, C. A. Ross, D. G. Schlom, M. S. Rzchowski, C.-B. Eom, J. Kim, *Nature* **2020**, *578*, 75.
[248] X. Chen, X. Fan, L. Li, N. Zhang, Z. Niu, T. Guo, S. Xu, H. Xu, D. Wang, H. Zhang, A. S. McLeod, Z. Luo, Q. Lu, A. J. Millis, D. N. Basov, M. Liu, C. Zeng, *Nat. Phys.* **2020**, *16*, 631.
[249] G. A. Smolenskii, A. I. Agranovskaya, *Zh. Tekh. Fiz.* **1958**, *28*, 1380.
[250] D. Lavric, R. A. Rao, Q. Gan, J. J. Krajewski, C.-B. Eom, *Integr. Ferroelectr.* **1998**, *21*, 499.
[251] P. M. Gehring, H. Hiraka, C. Stock, S.-H. Lee, W. Chen, Z.-G. Ye, S. B. Vakhrushev, Z. Chowdhuri, *Phys. Rev. B* **2009**, *79*, 224109.
[252] M. Davis, *J. Electroceram.* **2007**, *19*, 25.
[253] L. E. Cross, *Ferroelectrics* **1987**, *76*, 241.
[254] G. A. Samara, *J. Phys.: Condens. Matter* **2003**, *15*, R367.
[255] J. Hlinka, *J. Adv. Dielectr.* **2012**, *02*, 1241006.
[256] H. Takenaka, I. Grinberg, S. Liu, A. M. Rappe, *Nature* **2017**, *546*, 391.
[257] H. Hiraka, S.-H. Lee, P. M. Gehring, G. Xu, G. Shirane, *Phys. Rev. B* **2004**, *70*, 184105.
[258] D. La-Orauttapong, J. Toulouse, J. L. Robertson, Z.-G. Ye, *Phys. Rev. B* **2001**, *64*, 212101.
[259] G. Xu, G. Shirane, J. R. D. Copley, P. M. Gehring, *Phys. Rev. B* **2004**, *69*, 064112.
[260] M. J. Krogstad, P. M. Gehring, S. Rosenkranz, R. Osborn, F. Ye, Y. Liu, J. P. C. Ruff, W. Chen, J. M. Wozniak, H. Luo, O. Chmaissem, Z.-G. Ye, D. Phelan, *Nat. Mater.* **2018**, *17*, 718.
[261] J. Kim, H. Takenaka, Y. Qi, A. R. Damodaran, A. Fernandez, R. Gao, M. R. McCarter, S. Saremi, L. Chung, A. M. Rappe, L. W. Martin, *Adv. Mater.* **2019**, *31*, 1901060.
[262] A. Fernandez, J. Kim, D. Meyers, S. Saremi, L. W. Martin, *Phys. Rev. B* **2020**, *101*, 094102.
[263] G. Xu, Z. Zhong, Y. Bing, Z.-G. Ye, G. Shirane, *Nat. Mater.* **2006**, *5*, 134.
[264] J. Kim, D. J. Meyers, A. Kumar, A. Fernandez, G. A. P. Velarde, Z. Tian, J.-W. Kim, J. M. LeBeau, P. J. Ryan, L. W. Martin, *Matter* **2021**, *4*, 2367.
[265] F. Li, M. J. Cabral, B. Xu, Z. Cheng, E. C. Dickey, J. M. LeBeau, J. Wang, J. Luo, S. Taylor, W. Hackenberger, L. Bellaiche, Z. Xu, L.-Q. Chen, T. R. Shrout, S. Zhang, *Science* **2019**, *364*, 264.
[266] A. Kumar, J. N. Baker, P. C. Bowes, M. J. Cabral, S. Zhang, E. C. Dickey, D. L. Irving, J. M. LeBeau, *Nat. Mater.* **2020**, *20*, 62.
[267] S. Prosandeev, D. Wang, A. R. Akbarzadeh, L. Bellaiche, *J. Phys.: Condens. Matter* **2015**, *27*, 223202.
[268] S. Prosandeev, D. Wang, L. Bellaiche, *Phys. Rev. Lett.* **2013**, *111*, 247602.
[269] A. R. Akbarzadeh, S. Prosandeev, E. J. Walter, A. Al-Barakaty, L. Bellaiche, *Phys. Rev. Lett.* **2012**, *108*, 257601.
[270] B. Dkhil, P. Gemeiner, A. Al-Barakaty, L. Bellaiche, E. Dul'kin, E. Mojaev, M. Roth, *Phys. Rev. B* **2009**, *80*, 064103.
[271] S. Prosandeev, D. Wang, A. R. Akbarzadeh, B. Dkhil, L. Bellaiche, *Phys. Rev. Lett.* **2012**, *110*, 207601.
[272] H. Takenaka, I. Grinberg, A. M. Rappe, *Phys. Rev. Lett.* **2013**, *110*, 147602.
[273] I. Grinberg, Y.-H. Shin, A. M. Rappe, *Phys. Rev. Lett.* **2009**, *103*, 197601.
[274] D. Phelan, C. Stock, J. A. Rodriguez-Rivera, S. Chi, J. Leão, X. Long, Y. Xie, A. A. Bokov, Z.-G. Ye, P. Ganesh, P. M. Gehring, *Proc. Natl. Acad. Sci. USA* **2014**, *111*, 1754.
[275] S. Shetty, A. Damodaran, K. Wang, Y. Yuan, V. Gopalan, L. Martin, S. Trolier-McKinstry, *Adv. Funct. Mater.* **2019**, *29*, 1804258.
[276] H. Pan, F. Li, Y. Liu, Q. Zhang, M. Wang, S. Lan, Y. Zheng, J. Ma, L. Gu, Y. Shen, P. Yu, S. Zhang, L.-Q. Chen, Y.-H. Lin, C.-W. Nan, *Science* **2019**, *365*, 578.
[277] H. Pan, J. Ma, J. Ma, Q. Zhang, X. Liu, B. Guan, L. Gu, X. Zhang, Y.-J. Zhang, L. Li, Y. Shen, Y.-H. Lin, C.-W. Nan, *Nat. Commun.* **2018**, *9*, 1813.
[278] S. Saremi, J. Kim, A. Ghosh, D. Meyers, L. W. Martin, *Phys. Rev. Lett.* **2019**, *123*, 207602.
[279] S. Kojima, R. Imaizumi, S. Hamazaki, M. Takashige, *Jpn. J. Appl. Phys.* **2014**, *33*, 5559.
[280] T. S. Kalkur, J. Kulkarni, Y. C. Lu, M. Rowe, W. Han, L. Kammerdiner, *Ferroelectrics* **1991**, *116*, 135.
[281] R. Ramesh, K. Luther, B. Wilkens, D. L. Hart, E. Wang, J. A. Inam, X. D. Wu, T. Venkatesan, *Appl. Phys. Lett.* **1990**, *57*, 1505.
[282] P. C. Joshi, S. B. Krupanidhi, A. Mansingh, *J. Appl. Phys.* **1992**, *72*, 5517.
[283] N. Tohge, Y. Fukuda, T. Minami, *Jpn. J. Appl. Phys.* **1992**, *31*, 4016.
[284] S. E. Cummins, L. E. Cross, *J. Appl. Phys.* **1968**, *39*, 2268.
[285] Z. Tang, J. Chen, B. Yang, S. Zhao, *Appl. Phys. Lett.* **2019**, *114*, 163901.
[286] M. M. Seyfouri, Q. Liu, J. Yang, Y. Sun, X. Dai, J. Shi, X. Tan, S. Li, T. Wu, D. Wang, *J. Mater. Chem. C* **2021**, *9*, 3161.
[287] Z. Tang, B. Yang, J. Chen, Q. Lu, S. Zhao, *J. Alloys Compd.* **2019**, *772*, 298.
[288] Y. Wu, T. Yao, Y. Lu, B. Zou, X. Mao, F. Huang, H. Sun, X. Chen, *J. Mater. Sci.* **2017**, *52*, 7360.
[289] R. Ramesh, D. G. Schlom, *Science* **2002**, *296*, 1975.

[290] P. B. Jamieson, S. C. Abrahams, J. L. Bernstein, *J. Chem. Phys.* **1968**, *48*, 5048.
[291] K. L. Ngai, T. L. Reinecke, *Phys. Rev. Lett.* **1977**, *38*, 74.
[292] R. Bodeux, D. Michau, M. Josse, M. Maglione, *Solid State Sci.* **2014**, *38*, 112.
[293] A. J. Miller, A. Rotaru, D. C. Arnold, F. D. Morrison, *Dalton Trans.* **2015**, *44*, 10738.
[294] I. Levin, M. C. Stennett, G. C. Miles, D. I. Woodward, A. R. West, I. M. Reaney, *Appl. Phys. Lett.* **2006**, *89*, 122908.
[295] X. Zhu, M. Fu, M. C. Stennett, P. M. Vilarinho, I. Levin, C. A. Randall, J. Gardner, F. D. Morrison, I. M. Reaney, *Chem. Mater.* **2015**, *27*, 3250.
[296] X. L. Zhu, X. M. Chen, X. Q. Liu, X. G. Li, *J. Mater. Res.* **2008**, *23*, 3112.
[297] T. Hajlaoui, C. Harnagea, D. Michau, M. Josse, A. Pignolet, *J. Alloys Compd.* **2017**, *711*, 480.
[298] T. Hajlaoui, C. Chabanier, C. Harnagea, A. Pignolet, *Scr. Mater.* **2017**, *136*, 1.
[299] F. Roulland, M. Josse, E. Castel, M. Maglione, *Solid State Sci.* **2009**, *11*, 1709.
[300] T. Hajlaoui, M. Josse, C. Harnagea, A. Pignolet, *Mater. Res. Bull.* **2017**, *86*, 30.
[301] M. J. Harris, S. T. Bramwell, D. F. McMorrow, T. Zeiske, K. W. Godfrey, *Phys. Rev. Lett.* **1997**, *79*, 2554.
[302] C. Castelnovo, R. Moessner, S. L. Sondhi, *Nature* **2008**, *451*, 42.
[303] L. Balents, *Nature* **2010**, *464*, 199.
[304] Y. Zhou, K. Kanoda, T.-K. Ng, *Rev. Mod. Phys.* **2017**, *89*, 025003.
[305] Z.-C. Xu, M.-F. Liu, L. Lin, H. Liu, Z.-B. Yan, J.-M. Liu, *Front. Phys.* **2014**, *9*, 82.
[306] J. S. Gardner, M. J. P. Gingras, J. E. Greedan, *Rev. Mod. Phys.* **2010**, *82*, 53.
[307] R. Seshadri, *Solid State Sci.* **2006**, *8*, 259.
[308] T. Malcherek, U. Bismayer, C. Paulmann, *J. Phys.: Condens. Matter* **2010**, *22*, 205401.
[309] I. Hase, T. Yanagisawa, K. Kawashima, *Nanoscale Res. Lett.* **2018**, *13*, 63.
[310] S. Katayama, Y. Ogawa, H. Hayashi, F. Oba, I. Tanaka, *J. Cryst. Growth* **2015**, *416*, 126.
[311] H. L. Yakel, W. C. Koehler, E. F. Bertaut, E. F. Forrat, *Acta Crystallogr.* **1963**, *16*, 957.
[312] M. Lilienblum, T. Lottermoser, S. Manz, S. M. Selbach, A. Cano, M. Fiebig, *Nat. Phys.* **2015**, *11*, 1070.
[313] Y. Kumagai, N. A. Spaldin, *Nat. Commun.* **2013**, *4*, 1540.
[314] P. Barrozo, D. R. Småbråten, Y. Tang, B. Prasad, S. Saremi, R. Ozgur, V. Thakare, R. A. Steinhardt, M. E. Holtz, V. A. Stoica, L. W. Martin, D. G. Schlom, S. M. Selbach, R. Ramesh, *Adv. Mater.* **2020**, *32*, 2000508.
[315] M. Han, Y. Zhu, L. Wu, T. Aoki, V. Volkov, X. Wang, S. C. Chae, Y. S. Oh, S. Cheong, *Adv. Mater.* **2013**, *25*, 2415.
[316] J. A. Mundy, J. Schaab, Y. Kumagai, A. Cano, M. Stengel, I. P. Krug, D. M. Gottlob, H. Doğanay, M. E. Holtz, R. Held, Z. Yan, E. Bourret, C. M. Schneider, D. G. Schlom, D. A. Muller, R. Ramesh, N. A. Spaldin, D. Meier, *Nat. Mater.* **2017**, *16*, 622.
[317] Y. Geng, H. Das, A. L. Wysocki, X. Wang, S.-W. Cheong, M. Mostovoy, C. J. Fennie, W. Wu, *Nat. Mater.* **2014**, *13*, 163.
[318] H. Das, A. L. Wysocki, Y. Geng, W. Wu, C. J. Fennie, *Nat. Commun.* **2014**, *5*, 2998.
[319] C. Lin, J. Liu, Y. Li, X. Li, R. Li, *Solid State Commun.* **2013**, *173*, 51.
[320] T. Tohei, H. Moriwake, H. Murata, A. Kuwabara, R. Hashimoto, T. Yamamoto, I. Tanaka, *Phys. Rev. B* **2009**, *79*, 144125.
[321] S. V. Barabash, S. Fichtner, M. H. Park, T. Schenk, *Phys. Status Solidi RRL* **2021**, *15*, 2100201.
[322] T. S. Böscke, J. Müller, D. Bräuhaus, U. Schröder, U. Böttger, *Appl. Phys. Lett.* **2011**, *99*, 102903.
[323] P. Polakowski, J. Müller, *Appl. Phys. Lett.* **2015**, *106*, 232905.
[324] A. Pal, V. K. Narasimhan, S. Weeks, K. Littau, D. Pramanik, T. Chiang, *Appl. Phys. Lett.* **2017**, *110*, 022903.
[325] T. Shimizu, K. Katayama, T. Kiguchi, A. Akama, T. J. Konno, O. Sakata, H. Funakubo, *Sci. Rep.* **2016**, *6*, 32931.
[326] Z. Zhang, S. Hsu, V. A. Stoica, H. Paik, E. Parsonnet, A. Qualls, J. Wang, L. Xie, M. Kumari, S. Das, Z. Leng, M. McBriarty, R. Proksch, A. Gruverman, D. G. Schlom, L. Chen, S. Salahuddin, L. W. Martin, R. Ramesh, *Adv. Mater.* **2021**, *33*, 2006089.
[327] P. Nukala, J. Antoja-Lleonart, Y. Wei, L. Yedra, B. Dkhil, B. Noheda, *ACS Appl. Electron. Mater.* **2019**, *1*, 2585.
[328] J. Cao, S. Shi, Y. Zhu, J. Chen, *Phys. Status Solidi RRL* **2021**, *15*, 2100025.
[329] S. Starschich, T. Schenk, U. Schroeder, U. Boettger, *Appl. Phys. Lett.* **2017**, *110*, 182905.
[330] J. Müller, T. S. Böscke, U. Schröder, S. Mueller, D. Bräuhaus, U. Böttger, L. Frey, T. Mikolajick, *Nano Lett.* **2012**, *12*, 4318.
[331] K. D. Kim, M. H. Park, H. J. Kim, Y. J. Kim, T. Moon, Y. H. Lee, S. D. Hyun, T. Gwon, C. S. Hwang, *J. Mater. Chem. C* **2016**, *4*, 6864.
[332] H.-J. Lee, M. Lee, K. Lee, J. Jo, H. Yang, Y. Kim, S. C. Chae, U. Waghmare, J. H. Lee, *Science* **2020**, *369*, 1343.
[333] D.-H. Choe, S. Kim, T. Moon, S. Jo, H. Bae, S.-G. Nam, Y. S. Lee, J. Heo, *Mater. Today* **2021**, *50*, 8.
[334] A. Kashir, M. G. Farahani, J. Lančok, H. Hwang, S. Kamba, *Nanotechnology* **2022**, *33*, 155703.
[335] C. E. Dreyer, A. Janotti, C. G. V. de Walle, D. Vanderbilt, *Phys. Rev. X* **2016**, *6*, 021038.
[336] H. Moriwake, A. Konishi, T. Ogawa, K. Fujimura, C. A. J. Fisher, A. Kuwabara, T. Shimizu, S. Yasui, M. Itoh, *Appl. Phys. Lett.* **2014**, *104*, 242909.
[337] S. Fichtner, N. Wolff, F. Lofink, L. Kienle, B. Wagner, *J. Appl. Phys.* **2019**, *125*, 114103.
[338] D. Wang, J. Zheng, P. Musavigharavi, W. Zhu, A. C. Foucher, S. E. Trolier-McKinstry, E. A. Stach, R. H. Olsson, *IEEE Electron Device Lett.* **2020**, *41*, 1774.
[339] S. Yasuoka, T. Shimizu, A. Tateyama, M. Uehara, H. Yamada, M. Akiyama, Y. Hiranaga, Y. Cho, H. Funakubo, *J. Appl. Phys.* **2020**, *128*, 114103.
[340] W. Zhu, J. Hayden, F. He, J.-I. Yang, P. Tipsawat, M. D. Hossain, J.-P. Maria, S. Trolier-McKinstry, *Appl. Phys. Lett.* **2021**, *119*, 062901.
[341] K. Ferri, S. Bachu, W. Zhu, M. Imperatore, J. Hayden, N. Alem, N. Giebink, S. Trolier-McKinstry, J.-P. Maria, *J. Appl. Phys.* **2021**, *130*, 044101.
[342] J. Huang, Y. Hu, S. Liu, arXiv:2201.02938, **2022**.
[343] K. Alberi, M. B. Nardelli, A. Zakutayev, L. Mitas, S. Curtarolo, A. Jain, M. Fornari, N. Marzari, I. Takeuchi, M. L. Green, M. Kanatzidis, M. F. Toney, S. Butenko, B. Meredig, S. Lany, U. Kattner, A. Davydov, E. S. Toberer, V. Stevanovic, A. Walsh, N.-G. Park, A. Aspuru-Guzik, D. P. Tabor, J. Nelson, J. Murphy, A. Setlur, J. Gregoire, H. Li, R. Xiao, A. Ludwig, et al., *J. Phys. D: Appl. Phys.* **2018**, *52*, 013001.
[344] R. D. King-Smith, D. Vanderbilt, *Phys. Rev. B* **1992**, *47*, 1651.
[345] W. Sun, S. T. Dacek, S. P. Ong, G. Hautier, A. Jain, W. D. Richards, A. C. Gamst, K. A. Persson, G. Ceder, *Sci. Adv.* **2016**, *2*, e1600225.
[346] M. Aykol, S. S. Dwaraknath, W. Sun, K. A. Persson, *Sci. Adv.* **2018**, *4*, eaaq0148.
[347] T. E. Smidt, S. A. Mack, S. E. Reyes-Lillo, A. Jain, J. B. Neaton, *Sci. Data* **2020**, *7*, 72.
[348] M. de Jong, W. Chen, H. Geerlings, M. Asta, K. A. Persson, *Sci. Data* **2015**, *2*, 150053.
[349] H. Ling, S. S. Dwaraknath, K. A. Persson, *Chem. Mater.* **2020**, *32*, 2836.
[350] K. F. Garrity, *Phys. Rev. B* **2018**, *97*, 024115.
[351] E. Kroumova, M. I. Aroyo, J. M. Perez-Mato, *Acta Crystallogr., Sect. B: Struct. Sci., Cryst. Eng. Mater.* **2002**, *58*, 921.

[352] S. C. Abrahams, *Acta Crystallogr., Sect. B: Struct. Sci., Cryst. Eng. Mater.* **1996**, *52*, 790.
[353] S. C. Abrahams, *Acta Crystallogr., Sect. B: Struct. Sci., Cryst. Eng. Mater.* **1989**, *45*, 228.
[354] K. M. Rabe in *Functional Metal Oxides: New Science and Novel Applications* (Eds: S. B. Ogale, T. V. Venkatesan, M. G. Blamire), Wiley-VCH, Weinheim, Germany **2013**, Ch. 7.
[355] M. Acharya, S. Mack, A. Fernandez, J. Kim, H. Wang, K. Eriguchi, D. Meyers, V. Gopalan, J. Neaton, L. W. Martin, *Chem. Mater.* **2020**, *32*, 7274.
[356] D. J. Singh, *Phys. Rev. B* **2006**, *73*, 094102.
[357] A. A. Belik, M. Azuma, T. Saito, Y. Shimakawa, M. Takano, *Chem. Mater.* **2005**, *17*, 269.
[358] L. W. Martin, Q. Zhan, Y. Suzuki, R. Ramesh, M. Chi, N. Browning, T. Mizoguchi, J. Kreisel, *Appl. Phys. Lett.* **2007**, *90*, 062903.
[359] A. Kumar, L. W. Martin, S. Denev, J. B. Kortright, Y. Suzuki, R. Ramesh, V. Gopalan, *Phys. Rev. B* **2007**, *75*, 060101.
[360] T. Angsten, L. W. Martin, M. Asta, *Chem. Mater.* **2018**, *30*, 5870.
[361] J. H. Lee, L. Fang, E. Vlahos, X. Ke, Y. W. Jung, L. F. Kourkoutis, J.-W. Kim, P. J. Ryan, T. Heeg, M. Roeckerath, V. Goian, M. Bernhagen, R. Uecker, P. C. Hammel, K. M. Rabe, S. Kamba, J. Schubert, J. W. Freeland, D. A. Muller, C. J. Fennie, P. Schiffer, V. Gopalan, E. Johnston-Halperin, D. G. Schlom, *Nature* **2010**, *466*, 954.
[362] N. A. Benedek, A. T. Mulder, C. J. Fennie, *J. Solid State Chem.* **2012**, *195*, 11.
[363] A. T. Mulder, N. A. Benedek, J. M. Rondinelli, C. J. Fennie, *Adv. Funct. Mater.* **2013**, *23*, 4810.
[364] S. Yoshida, K. Fujita, H. Akamatsu, O. Hernandez, A. S. Gupta, F. G. Brown, H. Padmanabhan, A. S. Gibbs, T. Kuge, R. Tsuji, S. Murai, J. M. Rondinelli, V. Gopalan, K. Tanaka, *Adv. Funct. Mater.* **2018**, *28*, 1801856.
[365] A. Zunger, *Nature* **2019**, *566*, 447.
[366] R. Uecker, R. Bertram, M. Brützam, Z. Galazka, T. M. Gesing, C. Guguschev, D. Klimm, M. Klupsch, A. Kwasniewski, D. G. Schlom, *J. Cryst. Growth* **2017**, *457*, 137.
[367] H. Ritter, J. Ihringer, J. K. Maichle, W. Prandl, A. Hoser, A. W. Hewat, *Z. Phys. B: Condens. Matter* **1989**, *75*, 297.
[368] Y.-R. Luo, J.-M. Wu, *Appl. Phys. Lett.* **2001**, *79*, 3669.
[369] N. Yamada, I. Yasui, Y. Shigesato, H. Li, Y. Ujihara, K. Nomura, *Jpn. J. Appl. Phys.* **2014**, *38*, 2856.
[370] H. Ohta, M. Orita, M. Hirano, H. Tanji, H. Kawazoe, H. Hosono, *Appl. Phys. Lett.* **2000**, *76*, 2740.
[371] M. Yan, M. Lane, C. R. Kannewurf, R. P. H. Chang, *Appl. Phys. Lett.* **2001**, *78*, 2342.
[372] B. Li, L. Zeng, F. Zhang, *Phys. Status Solidi* **2004**, *201*, 960.
[373] M. Liberati, R. V. Chopdekar, V. Mehta, E. Arenholz, Y. Suzuki, *J. Magn. Magn. Mater.* **2009**, *321*, 2852.
[374] M. Mirjolet, F. Sánchez, J. Fontcuberta, *Adv. Funct. Mater.* **2019**, *29*, 1808432.
[375] H. Falcón, J. A. Alonso, M. T. Casais, M. J. MartÍnez-Lope, J. Sánchez-BenÍtez, *J. Solid State Chem.* **2004**, *177*, 3099.
[376] J.-S. Zhou, C.-Q. Jin, Y.-W. Long, L.-X. Yang, J. B. Goodenough, *Phys. Rev. Lett.* **2006**, *96*, 046408.
[377] J. F. Weiher, B. L. Chamberland, J. L. Gillson, *J. Solid State Chem.* **1971**, *3*, 529.
[378] B. Chamberland, *Solid State Commun.* **1967**, *5*, 663.
[379] H. H. Wang, D. F. Cui, Y. L. Zhou, Z. H. Chen, F. Chen, T. Zhao, H. B. Lu, G. Z. Yang, M. C. Xu, Y. C. Lan, X. L. Chen, H. J. Qian, F. Q. Liu, *J. Cryst. Growth* **2001**, *226*, 261.
[380] O. Auciello, J. F. Scott, R. Ramesh, *Phys. Today* **1998**, *51*, 22.
[381] X. J. Lou, *Appl. Phys. Lett.* **2009**, *94*, 072901.
[382] M. Pešić, M. Hoffmann, C. Richter, T. Mikolajick, U. Schroeder, *Adv. Funct. Mater.* **2016**, *26*, 7486.
[383] M. Pesic, S. Knebel, M. Hoffmann, C. Richter, T. Mikolajick, U. Schroeder, *2016 IEEE Int. Electron Devices Meeting (IEDM)*, IEEE, Piscataway, NJ, USA **2016**, https://doi.org/10.1109/IEDM.2016.7838398.
[384] L. Xie, L. Li, C. A. Heikes, Y. Zhang, Z. Hong, P. Gao, C. T. Nelson, F. Xue, E. Kioupakis, L. Chen, D. G. Schlom, P. Wang, X. Pan, *Adv. Mater.* **2017**, *29*, 1701475.
[385] H. Lu, X. Liu, J. D. Burton, C.-W. Bark, Y. Wang, Y. Zhang, D. J. Kim, A. Stamm, P. Lukashev, D. A. Felker, C. M. Folkman, P. Gao, M. S. Rzchowski, X. Q. Pan, C.-B. Eom, E. Y. Tsymbal, A. Gruverman, *Adv. Mater.* **2012**, *24*, 1209.
[386] T. Mikolajick, U. Schroeder, S. Slesazeck, *IEEE Trans. Electron Devices* **2020**, *67*, 1434.
[387] T. Mikolajick, S. Slesazeck, M. H. Park, U. Schroeder, *MRS Bull.* **2018**, *43*, 340.
[388] B. Max, M. Hoffmann, S. Slesazeck, T. Mikolajick, in *2018 48th Eur. Solid-State Device Research Conf. (ESSDERC)*, IEEE, Piscataway, NJ, USA **2018**, pp. 142–145.
[389] G. E. Moore, *Electronics* **1965**, *38*, 114.
[390] R. H. Dennard, F. H. Gaensslen, H.-N. Yu, V. L. Rideout, E. Bassous, A. R. LeBlanc, *IEEE J. Solid-State Circuits* **1974**, *9*, 256.
[391] J. D. Meindl, Q. Chen, J. A. Davis, *Science* **2001**, *293*, 2044.
[392] I. Ferain, C. A. Colinge, J.-P. Colinge, *Nature* **2011**, *479*, 310.
[393] S. Manipatruni, D. E. Nikonov, I. A. Young, *Nat. Phys.* **2018**, *14*, 338.
[394] D. E. Nikonov, I. A. Young, *IEEE J. Explor. Solid-State Comput. Devices Circuits* **2015**, *1*, 3.
[395] A. I. Khan, A. Keshavarzi, S. Datta, *Nat. Electron.* **2020**, *3*, 588.
[396] Y. Long, D. Kim, E. Lee, P. Saha, B. A. Mudassar, X. She, A. I. Khan, S. Mukhopadhyay, *IEEE J. Explor. Solid-State Comput. Devices Circuits* **2019**, *5*, 113.
[397] J. C. Wong, S. Salahuddin, *Proc. IEEE* **2019**, *107*, 49.
[398] S. Salahuddin, S. Datta, *Nano Lett.* **2008**, *8*, 405.
[399] Y. Fang, Z. Wang, J. Gomez, S. Datta, A. I. Khan, A. Raychowdhury, *Front. Neurosci.* **2019**, *13*, 855.
[400] M. Seo, M.-H. Kang, S.-B. Jeon, H. Bae, J. Hur, B. C. Jang, S. Yun, S. Cho, W.-K. Kim, M.-S. Kim, K.-M. Hwang, S. Hong, S.-Y. Choi, Y.-K. Choi, *IEEE Electron Device Lett.* **2018**, *39*, 1445.
[401] E. J. Fuller, S. T. Keene, A. Melianas, Z. Wang, S. Agarwal, Y. Li, Y. Tuchman, C. D. James, M. J. Marinella, J. J. Yang, A. Salleo, A. A. Talin, *Science* **2019**, *364*, eaaw5581.
[402] S. Oh, H. Hwang, I. K. Yoo, *APL Mater.* **2019**, *7*, 091109.
[403] J. Seidel, P. Maksymovych, Y. Batra, A. Katan, S.-Y. Yang, Q. He, A. P. Baddorf, S. V. Kalinin, C.-H. Yang, J.-C. Yang, Y.-H. Chu, E. K. H. Salje, H. Wormeester, M. Salmeron, R. Ramesh, *Phys. Rev. Lett.* **2010**, *105*, 197603.
[404] M. Schröder, A. Haußmann, A. Thiessen, E. Soergel, T. Woike, L. M. Eng, *Adv. Funct. Mater.* **2012**, *22*, 3936.
[405] P. Sharma, T. S. Moise, L. Colombo, J. Seidel, *Adv. Funct. Mater.* **2021**, *32*, 2110263.
[406] P. Sharma, Q. Zhang, D. Sando, C. H. Lei, Y. Liu, J. Li, V. Nagarajan, J. Seidel, *Sci. Adv.* **2017**, *3*, e1700512.
[407] A. Q. Jiang, Y. Zhang, *NPG Asia Mater.* **2019**, *11*, 2.
[408] J. Seidel, R. Ramesh, in *Domain Walls: From Fundamental Properties to Nanotechnology Concepts*, (Eds: D. Meier, J. Seidel, M. Gregg, R. Ramesh), Oxford University Press, Oxford, UK **2020**, Ch. 15, https://doi.org/10.1093/oso/9780198862499.003.0015.
[409] S. Manipatruni, D. E. Nikonov, C.-C. Lin, T. A. Gosavi, H. Liu, B. Prasad, Y.-L. Huang, E. Bonturim, R. Ramesh, I. A. Young, *Nature* **2018**, *565*, 35.
[410] A. Vorobiev, P. Rundqvist, K. Khamchane, S. Gevorgian, *Appl. Phys. Lett.* **2003**, *83*, 3144.
[411] X. Liang, Z. Meng, W. Wu, *J. Am. Ceram. Soc.* **2004**, *87*, 2218.
[412] Z. Gu, S. Pandya, A. Samanta, S. Liu, G. Xiao, C. J. G. Meyers, A. R. Damodaran, H. Barak, A. Dasgupta, S. Saremi, A. Polemi,

L. Wu, A. A. Podpirka, A. Will-Cole, C. J. Hawley, P. K. Davies, R. A. York, I. Grinberg, L. W. Martin, J. E. Spanier, *Nature* **2018**, *560*, 622.
[413] C.-H. Lee, N. D. Orloff, T. Birol, Y. Zhu, V. Goian, E. Rocas, R. Haislmaier, E. Vlahos, J. A. Mundy, L. F. Kourkoutis, Y. Nie, M. D. Biegalski, J. Zhang, M. Bernhagen, N. A. Benedek, Y. Kim, J. D. Brock, R. Uecker, X. X. Xi, V. Gopalan, D. Nuzhnyy, S. Kamba, D. A. Muller, I. Takeuchi, J. C. Booth, C. J. Fennie, D. G. Schlom, *Nature* **2013**, *502*, 532.
[414] A. P. Levanyuk, D. G. Sannikov, *Sov. Phys. - Usp.* **1974**, *17*, 199.
[415] M. Acharya, E. Banyas, M. Ramesh, Y. Jiang, A. Fernandez, A. Dasgupta, H. Ling, B. Hanrahan, K. Persson, J. B. Neaton, L. W. Martin, *Adv. Mater.* **2021**, *34*, 2105967.
[416] J. Kim, S. Saremi, M. Acharya, G. Velarde, E. Parsonnet, P. Donahue, A. Qualls, D. Garcia, L. W. Martin, *Science* **2020**, *369*, 81.
[417] X. Wei, C. Jia, H. Du, K. Roleder, J. Mayer, R. E. Dunin-Borkowski, *Adv. Mater.* **2020**, *32*, 1907208.
[418] M.-F. Tsai, Y.-Z. Zheng, S.-C. Lu, J.-D. Zheng, H. Pan, C.-G. Duan, P. Yu, R. Huang, Y.-H. Chu, *Adv. Funct. Mater.* **2021**, *31*, 2105060.
[419] B. Ma, Z. Hu, R. E. Koritala, T. H. Lee, S. E. Dorris, U. Balachandran, *J. Mater. Sci.: Mater. Electron.* **2015**, *26*, 9279.
[420] M. H. Park, H. J. Kim, Y. J. Kim, T. Moon, K. D. Kim, C. S. Hwang, *Adv. Energy Mater.* **2014**, *4*, 1400610.
[421] H. Palneedi, M. Peddigari, G. Hwang, D. Jeong, J. Ryu, *Adv. Funct. Mater.* **2018**, *28*, 1803665.
[422] Z. Liu, T. Lu, J. Ye, G. Wang, X. Dong, R. Withers, Y. Liu, *Adv. Mater. Technol.* **2018**, *3*, 1800111.
[423] H. Cheng, J. Ouyang, Y.-X. Zhang, D. Ascienzo, Y. Li, Y.-Y. Zhao, Y. Ren, *Nat. Commun.* **2017**, *8*, 1999.
[424] B. Peng, Q. Zhang, X. Li, T. Sun, H. Fan, S. Ke, M. Ye, Y. Wang, W. Lu, H. Niu, X. Zeng, H. Huang, *ACS Appl. Mater. Interfaces* **2015**, *7*, 13512.
[425] H. J. Jung, Y. Song, S. K. Hong, C. H. Yang, S. J. Hwang, S. Y. Jeong, T. H. Sung, *Sens. Actuators, A* **2015**, *222*, 314.
[426] J. Sirohi, R. Mahadik, *J. Intell. Mater. Syst. Struct.* **2011**, *22*, 2215.
[427] M. Wischke, M. Masur, M. Kröner, P. Woias, *Smart Mater. Struct.* **2011**, *20*, 085014.
[428] Y. Kuang, T. Ruan, Z. J. Chew, M. Zhu, *Sens. Actuators, A* **2017**, *254*, 69.
[429] C.-B. Eom, S. Trolier-McKinstry, *MRS Bull.* **2012**, *37*, 1007.
[430] D. Isarakorn, A. Sambri, P. Janphuang, D. Briand, S. Gariglio, J.-M. Triscone, F. Guy, J. W. Reiner, C. H. Ahn, N. F. de Rooij, *J. Micromech. Microeng.* **2010**, *20*, 055008.
[431] H. Liu, H. Wu, K. P. Ong, T. Yang, P. Yang, P. K. Das, X. Chi, Y. Zhang, C. Diao, W. K. A. Wong, E. P. Chew, Y. F. Chen, C. K. I. Tan, A. Rusydi, M. B. H. Breese, D. J. Singh, L.-Q. Chen, S. J. Pennycook, K. Yao, *Science* **2020**, *369*, 292.
[432] S. Shetty, J. I. Yang, J. Stitt, S. Trolier-McKinstry, *J. Appl. Phys.* **2015**, *118*, 174104.
[433] B. Ren, S. W. Or, Y. Zhang, Q. Zhang, X. Li, J. Jiao, W. Wang, D. Liu, X. Zhao, H. Luo, *Appl. Phys. Lett.* **2010**, *96*, 083502.
[434] V. Nagarajan, A. Roytburd, A. Stanishevsky, S. Prasertchoung, T. Zhao, L. Chen, J. Melngailis, O. Auciello, R. Ramesh, *Nat. Mater.* **2003**, *2*, 43.
[435] R. Keech, S. Shetty, M. A. Kuroda, X. H. Liu, G. J. Martyna, D. M. Newns, S. Trolier-McKinstry, *J. Appl. Phys.* **2014**, *115*, 234106.
[436] C. K. Jeong, K.-I. Park, J. H. Son, G.-T. Hwang, S. H. Lee, D. Y. Park, H. E. Lee, H. K. Lee, M. Byun, K. J. Lee, *Energy Environ. Sci.* **2014**, *7*, 4035.
[437] S. Xu, Y. Qin, C. Xu, Y. Wei, R. Yang, Z. L. Wang, *Nat. Nanotechnol.* **2010**, *5*, 366.
[438] M. Zhang, T. Gao, J. Wang, J. Liao, Y. Qiu, Q. Yang, H. Xue, Z. Shi, Y. Zhao, Z. Xiong, L. Chen, *Nano Energy* **2015**, *13*, 298.
[439] N. Sezer, M. Koç, *Nano Energy* **2021**, *80*, 105567.
[440] H. Liu, J. Zhong, C. Lee, S.-W. Lee, L. Lin, *Appl. Phys. Rev.* **2018**, *5*, 041306.
[441] Z. Yang, S. Zhou, J. Zu, D. Inman, *Joule* **2018**, *2*, 642.
[442] Y. Q. Fu, J. K. Luo, N. T. Nguyen, A. J. Walton, A. J. Flewitt, X. T. Zu, Y. Li, G. McHale, A. Matthews, E. Iborra, H. Du, W. I. Milne, *Prog. Mater. Sci.* **2017**, *89*, 31.
[443] G. Sebald, S. Pruvost, D. Guyomar, *Smart Mater. Struct.* **2008**, *17*, 015012.
[444] S. Pandya, G. Velarde, L. Zhang, J. D. Wilbur, A. Smith, B. Hanrahan, C. Dames, L. W. Martin, *NPG Asia Mater.* **2019**, *11*, 26.
[445] G. Velarde, S. Pandya, J. Karthik, D. Pesquera, L. W. Martin, *APL Mater.* **2021**, *9*, 010702.
[446] S. Pandya, J. D. Wilbur, B. Bhatia, A. R. Damodaran, C. Monachon, A. Dasgupta, W. P. King, C. Dames, L. W. Martin, *Phys. Rev. Appl.* **2017**, *7*, 034025.
[447] J. Karthik, J. C. Agar, A. R. Damodaran, L. W. Martin, *Phys. Rev. Lett.* **2012**, *109*, 257602.
[448] S. Pandya, G. A. Velarde, R. Gao, A. S. Everhardt, J. D. Wilbur, R. Xu, J. T. Maher, J. C. Agar, C. Dames, L. W. Martin, *Adv. Mater.* **2019**, *31*, 1803312.
[449] G. Velarde, S. Pandya, L. Zhang, D. Garcia, E. Lupi, R. Gao, J. D. Wilbur, C. Dames, L. W. Martin, *ACS Appl. Mater. Interfaces* **2019**, *11*, 35146.
[450] R. V. K. Mangalam, J. C. Agar, A. R. Damodaran, J. Karthik, L. W. Martin, *ACS Appl. Mater. Interfaces* **2013**, *5*, 13235.
[451] S. Pandya, J. Wilbur, J. Kim, R. Gao, A. Dasgupta, C. Dames, L. W. Martin, *Nat. Mater.* **2018**, *17*, 432.
[452] S. Pandya, G. Velarde, L. Zhang, L. W. Martin, *Phys. Rev. Mater.* **2018**, *2*, 124405.
[453] S. Liu, Y. Kim, L. Z. Tan, A. M. Rappe, *Nano Lett.* **2016**, *16*, 1663.
[454] S. Das, A. Ghosh, M. R. McCarter, S.-L. Hsu, Y.-L. Tang, A. R. Damodaran, R. Ramesh, L. W. Martin, *APL Mater.* **2018**, *6*, 100901.
[455] S. Das, Z. Hong, M. McCarter, P. Shafer, Y.-T. Shao, D. A. Muller, L. W. Martin, R. Ramesh, *APL Mater.* **2020**, *8*, 120902.
[456] N. S. Kiselev, A. N. Bogdanov, R. Schäfer, U. K. Rößler, *J. Phys. D: Appl. Phys.* **2011**, *44*, 392001.
[457] A. Fert, V. Cros, J. Sampaio, *Nat. Nanotechnol.* **2013**, *8*, 152.
[458] J. D. Koralek, C. P. Weber, J. Orenstein, B. A. Bernevig, S.-C. Zhang, S. Mack, D. D. Awschalom, *Nature* **2009**, *458*, 610.
[459] L. L. Tao, E. Y. Tsymbal, *J. Phys. D: Appl. Phys.* **2021**, *54*, 113001.
[460] L. L. Tao, E. Y. Tsymbal, *Nat. Commun.* **2018**, *9*, 2763.
[461] X.-Z. Lu, J. M. Rondinelli, *Matter* **2020**, *3*, 1211.

Abel Fernandez is currently pursuing his Ph.D. in the Department of Materials Science and Engineering at the University of California, Berkeley (UC Berkeley). He is a UC Berkeley Chancellor's Fellow and a National Science Foundation Graduate Research Fellow. He received his B.S. in chemistry from the University of California, Santa Barbara in 2016. While his research has covered a range of topics, he is currently focused on the synthesis, fabrication, and study of freestanding membranes of relaxor ferroelectrics.

Megha Acharya is currently pursuing her Ph.D. in the Department of Materials Science and Engineering at the University of California, Berkeley. Prior to this, she received her M.S. degree in materials science and engineering from the Indian Institute of Technology, Kanpur in 2018. She received her Bachelor's degree in ceramic engineering from the National Institute of Technology, Rourkela (India) in 2016. Among a wide variety of areas, her current research interests are focused on the discovery, design, and realization of novel complex-perovskite-based oxides for ferroelectric applications.

Lane W. Martin received his B.S. (2003, Carnegie Mellon University), M.S., and Ph.D. (2006 and 2008, respectively, University of California, Berkeley) all in materials science and engineering. He was a Postdoctoral Researcher at the Lawrence Berkeley National Laboratory from 2008 to 2009 before joining the University of Illinois, Urbana–Champaign as an Assistant Professor in Materials Science and Engineering from 2009 to 2014. Since 2014, he has been in the Department of Materials Science and Engineering at the University of California, Berkeley as an Associate Professor (2014–2018), Professor and Vice Chair (2018–2021), and Chancellor's Professor and Chair (2021–now).